

**SEISMIC IMAGING WITH OCEAN-BOTTOM NODES (OBN):
NEW ACQUISITION DESIGNS AND THE ATLANTIS 4C OBN SURVEY**

A Thesis

Presented to

the Department of Earth and Atmospheric Sciences

University of Houston

In Partial Fulfillment

of the Requirements for the Degree

Master of Science

by

Emin Emrah Pacal

May, 2012

**SEISMIC IMAGING WITH OCEAN-BOTTOM NODES (OBN):
NEW ACQUISITION DESIGNS AND THE ATLANTIS 4C OBN SURVEY**

Emin Emrah Pacal

APPROVED:

Dr. Robert Stewart (Chairman)

Dr. Christopher Liner (Member)

Mr. Bjorn Olofsson (Member)

Dean, College of Natural Sciences and Mathematics

Acknowledgements

I am very thankful to people who served, challenged, encouraged, and supported me throughout my academic program in the University of Houston. My sincere appreciation especially goes to my advisor, Dr. Robert Stewart for his guidance in my work and giving me the opportunity to participate in the remarkable research projects at the Allied Geophysical Laboratories (AGL). Appreciation is also extended to Dr. Chris Liner and Dr. Bob Wiley for their support and comments.

I am also very grateful to Dr. Edip Baysal, Dr. Orhan Yilmaz, and Irfan Tanritanir who had contributed great efforts to my thesis at Paradigm. I am highly indebted to Mr. Bjorn Olofsson of SeaBird for his time and sharing of his knowledge.

This work was made possible by the generous donation of the seismic data by SeaBird Exploration. I also acknowledge companies, GEDCO and Paradigm for software support. I would also like to take this opportunity to thank the Turkish Petroleum Corporation (TPAO) for their financial support.

My friends in Allied Geophysical Laboratories (AGL) and in the Department of Geosciences of University of Houston are thanked for their friendship and support.

The last but not the least, I wish to express my great gratitude to my parents, Lutfu and Hatice Pacal, my sister and brother, Gulsah and Emre Pacal for their understanding, support, and courage.

**SEISMIC IMAGING WITH OCEAN-BOTTOM NODES (OBN):
NEW ACQUISITION DESIGNS AND THE ATLANTIS 4C OBN SURVEY**

A Thesis
Presented to
the Department of Earth and Atmospheric Sciences
University of Houston

In Partial Fulfillment
of the Requirements for the Degree
Master of Science

by
Emin Emrah Pacal
May, 2012

Abstract

The limitations in conventional marine seismic surveys such as imaging of complicated geology in the deep water motivate a quest for new and alternative technologies such as OBNs (ocean-bottom nodes). In this study, survey designs for OBN to provide better fold, offset, and azimuth distributions are created. Augmented VSP geometries are also studied and compared with conventional orthogonal geometries. Then I created joint survey design with both VSP and OBN by combining these two surveys. The results show that joint survey design of VSP and OBN has improved azimuth and offset distribution then VSP itself. In this case, limitations with VSP survey such as poor azimuth and offset coverage can be enhanced by combining VSP survey with ocean-bottom nodes.

A main challenge with the ocean-bottom nodes is now processing and imaging of the data. The mirror migration technique is an effective solution for this challenge by separation of the seabed hydrophone and geophone data into up-going and down-going waves. In this study, I explained that mirror imaging (imaging from the down-going ghost reflections) can produce better image quality than conventional up-going imaging. To understand the mirror imaging technique, we first generated synthetic dataset to apply this technique. I then apply mirror imaging technique to Seabird's Seatrial OBN dataset acquired near the Atlantis field in the Gulf of Mexico. To obtain images from down-going and up-going waves, we used Kirchhoff pre-stack time migration (KPSTM),

Kirchhoff pre-stack depth migration (KPSDM) and reverse time migration (RTM) algorithms. The results show that mirror imaging of down-going waves provide better illuminated image from shallow subsurface than conventional migration of up-going waves.

Table of Contents

| | | |
|------------------------------|---|-----------|
| Acknowledgements | | iii |
| Abstract | | v |
| List of Figures | | x |
| List of Tables | | xix |
| List of Abbreviations | | xx |
| | | |
| Chapter 1. | INTRODUCTION | 1 |
| 1.1. | Motivation to Deployed Ocean-bottom Nodes | 4 |
| Chapter 2. | OBN, VSP and JOINT OBN-VSP SURVEY DESIGNS | 10 |
| 2.1. | Ocean-bottom Acquisition Techniques | 10 |
| 2.2. | VSP Survey Design | 15 |
| 2.3. | OBN Survey Design | 21 |
| 2.4. | Joint OBN-VSP Survey Design | 29 |
| Chapter 3. | ATLANTIS SEABIRD SEATRIAL 3D-4C OBN SURVEY | 35 |
| 3.1. | Atlantis Field and Deepwater Imaging Challenges | 35 |
| 3.2. | Atlantis Seatrial 3D-4C OBN Survey | 38 |

| | | |
|-------------------|--|----|
| 3.3. | Atlantis Field Synthetic Data | 41 |
| Chapter 4. | OCEAN-BOTTOM NODE DATA PROCESSING AND IMAGING | 47 |
| 4.1. | Motivation..... | 47 |
| 4.2. | Wavefield Separation..... | 48 |
| 4.2.1. | Application to Atlantis Seatrial OBN data..... | 53 |
| 4.2.1. A. | Wavelet shaping..... | 53 |
| 4.2.1. B. | Deghosting and PZ summation | 61 |
| 4.3. | Background Velocity Estimation | 66 |
| 4.4. | Imaging from Multiples (Mirror Imaging) | 71 |
| 4.4.1. | Mirror Imaging with Kirchhoff Pre-stack Time Migration (KPSTM) | 75 |
| 4.4.2. | Mirror Imaging with Kirchhoff Pre-stack Depth Migration (KPSDM)..... | 82 |
| 4.4.3. | Mirror Imaging with Kirchhoff Pre-stack Time Migration (KPSTM) | 87 |
| 4.4.3. A. | Synthetic data example..... | 88 |
| 4.4.3. B. | Field data example | 92 |
| Chapter 5. | CONCLUSION | 96 |
| References | | 98 |

| | | |
|-------------------|--|-----|
| Appendix | | 104 |
| Appendix A | Fundamentals of Survey Design..... | 104 |
| A.1. | Fold | 104 |
| A.2. | Bin Size | 108 |
| A.3. | Minimum Offset | 110 |
| Appendix B | Deghosting and PZ summation..... | 111 |
| Appendix C | Imaging condition for RTM of multiples | 115 |

LIST OF FIGURES:

Figure 1.1: Ocean-bottom cable (OBC) (right) and ocean-bottom node (OBN) (left) acquisition. OBC is deployed on the seafloor and connected by electrical wires. OBN is also deployed on the seafloor; however, they are autonomous recording system. 2

Figure 1.2: Comparison of narrow azimuth towed streamer (A), and receiver migrated OBS node (B). The node images benefit from the improved salt model (Beaudoin, 2010). 5

Figure 1.3: Comparison of extra-salt images at the Miocene level at Atlantis. Higher resolution and improved fault definition are apparent in the OBS wide-azimuth node image on the bottom compared to the narrow-azimuth towed streamer image above (Howie et al. 2008)..... 6

Figure 1.4: Wavefield separation. From left to right, a common receiver gather (CRG) for a) pressure, b) vertical component of particle velocity, c) up-going wavefield, d) down-going wavefield, and (e) the up-down deconvolution result. Events M1 and M2 are the first and second order water-layer multiples (Wang, 2010). 7

Figure 1.5: PP and PS imaging. The PS image (right) reveals details of the reservoir which are hidden on the PP image (left) by effects from the shallow gas (Ronholt et al., 2008). 8

Figure 2.1: Ocean-bottom Seismograph (OBS) consist of 3 component geophones and a hydrophone (Modified from GeoPro ocean-bottom seismograph)..... 10

Figure 2.2: Schematic illustration of OBC receivers lay on the sea bottom. 4C receivers record the velocity and pressure..... 12

Figure 2.3: Examples of 4-C receivers in an ocean-bottom cable (modified from Caldwell et al., 1999). From left to right, the hydrophone (pressure sensitive), radial (inline), transverse (crossline) and vertical components. 12

Figure 2.4: Ocean-bottom node system consists of 3C geophone module, hydrophone, and battery and recorder module. Top figure shows node with cover, bottom show node without cover Modified from Fairfield ocean-bottom node..... 13

Figure 2.5: Imaging comparison at Atlantis of 3D conventional marine seismic (left) and receiver migrated 3D OBN seismic (right). The node images benefit from an improved salt model (Howie et al., 2008) Courtesy BP. 14

Figure 2.6: Map of shots geometry in a circular pattern for 3D VSP (Burch, 2010)..... 16

Figure 2.7: Depth Fold map of VSP survey designs with different parameters. The left top is Survey 1, right top is Survey 2, the left bottom is Survey 3, and the right bottom is Survey 4. 17

Figure 2.8: VSP source and receiver positions on 3D view. Red symbols represent shot locations (10 concentric circles) and blue symbols represent receiver locations..... 18

Figure 2.9: Fold map of 3D VSP survey with circular shooting geometry (10 concentric circles). The top shows a plane view of fold distribution and bottom shows 3D view. The red color indicates maximum fold, blue indicates minimum fold..... 19

Figure 2.10: Azimuth and fold distribution for selected bin grid. Top left shows azimuth, right shows fold, and bottom shows selected partial bin grid. 20

Figure 2.11: Example of dense shot carpet geometry from Atlantis Seatrial survey. Blue points show nodes locations and black dots show shot locations. 21

Figure 2.12: Hexagonal receiver location (blue dots) under platform with 58m interval, circular shooting geometry (black dots) with 10m shot interval and 10, interval between circles (Apache Co., 2009)..... 22

Figure 2.13: Receiver locations (blue dot) and dense shot (red dots) carpet geometry for orthogonal OBN survey. 23

Figure 2.14: Circular shooting geometry with ocean-bottom nodes. Red dots represent source locations and blue dots represent receiver locations. 24

Figure 2.15: Fold distributions for OBN surveys. The top figure shows circular shooting fold distribution and the bottom shows orthogonal shooting fold distribution. 25

Figure 2.16: Comparison of azimuth (bottom) and offset (top) coverage for both surveys. The left charts are offset and azimuth distribution for circular shooting and the right charts are offset and azimuth distribution for orthogonal shooting. 26

Figure 2.17: Comparison of circular shooting geometry (top) and orthogonal shooting geometry (bottom) in rose diagram. 27

Figure 2.18: Azimuth and offset distribution in selected bin grid for circular and orthogonal shooting geometry. Top left shows azimuth distribution and top right shows offset distribution for circular shooting. Bottom left represents azimuth distribution and bottom right offset distribution for orthogonal shooting. 28

Figure 2.19: 3D view of source and receiver locations for joint OBN-VSP survey. Red circles shows shots, and blue point shows VSP receiver and ocean-bottom node locations. 30

Figure 2.20: Fold coverage for VSP survey itself in plane view on top and 3D view on bottom. .. 31

Figure 2.21: Fold coverage for joint OBN-VSP survey in plane view on top and 3D view on bottom..... 32

| | |
|--|-----------|
| <i>Figure 2.22: Comparison of azimuthal coverage for both surveys in selected area. Top shows azimuth distribution for VSP survey itself, bottom shows azimuth distribution for joint survey.</i> | <i>33</i> |
| <i>Figure 2.23: Comparison of offset coverage for both surveys in selected area. Top shows offset distribution for VSP survey itself; bottom shows offset distribution for joint survey.</i> | <i>34</i> |
| <i>Figure 3.1: Location map of Atlantis field, Gulf of Mexico (Howie et al., 2008).</i> | <i>35</i> |
| <i>Figure 3.2: Geological cross section over the Atlantis field. (Howie et al., 2008).....</i> | <i>36</i> |
| <i>Figure 3.3: 3D view of Sigsbee Escarpment. Sigsbee bathymetry was displayed on OMNI 3D. The black circle indicates the area of Atlantis field.....</i> | <i>37</i> |
| <i>Figure 3.4: Atlantis Seatrial survey. Shot (black dots) and node positions (blue dot).....</i> | <i>38</i> |
| <i>Figure 3.5: Illumination of Seatrial OBN survey on the sea floor. The black dots inticates node locations, red dots indicate source locations. The grey surface indicates ocean-bottom with elevation range from -2300m to -1400m.....</i> | <i>39</i> |
| <i>Figure 3.6: Azimuth and Offset distribution of Seatrial OBN servey. (a) Offset distribution-trace count. (b) offset distribution – stick diagram. (c) Azimuth distribution-trace count. (d) azimuth distrubition – spider diagram.</i> | <i>40</i> |
| <i>Figure 3.7: Raw receiver gathers from Seatrial OBN dataset. From left to right: X , Y, Z (vertical) and P (pressure) components.</i> | <i>41</i> |
| <i>Figure 3.8: 2D section of synthetic velocity model.....</i> | <i>42</i> |
| <i>Figure 3.9: Atlantis field synthetic receiver gathers.....</i> | <i>43</i> |
| <i>Figure 3.10: Synthetic up-going wavefield data and real Z component data from the Seatrial OBN survey.</i> | <i>44</i> |

| | |
|--|-----------|
| <i>Figure 3.11: Synthetic down-going wavefield data and real down-going wavefield data from Seatrial OBN survey. In down-going synthetic data, direct arrivals and receiver-side ghost can be clearly seen.</i> | <i>45</i> |
| <i>Figure 4.1: Schematic diagram of the hydrophone and geophone at the ocean-bottom as they record up and down-going wavefield.....</i> | <i>49</i> |
| <i>Figure 4.2: (a) Schematic demonstration of source-side and (b) receiver-side multiples on a 2D model (Modified from Xia, 2006).</i> | <i>51</i> |
| <i>Figure 4.3: Demonstration of source-side and receiver-side multiples on a 2D synthetic example (Xia, 2006).</i> | <i>51</i> |
| <i>Figure 4.4: The raw vertical component (Z) common-receiver gathers of Seatrial OBN data from selected shot line.</i> | <i>55</i> |
| <i>Figure 4.5: The raw pressure component (P) common-receiver gathers of Seatrial OBN data from selected shot line.</i> | <i>56</i> |
| <i>Figure 4.6: Butterworth wavelet and Butterworth scaling function. This figure was created in MATLAB.</i> | <i>57</i> |
| <i>Figure 4.7: Desired and generated Butterworth wavelet. Low-cut frequency is 10 Hz, high-cut frequency is 80 Hz. Slope in the low-cut side is 18, and in the high-cut side is 36.</i> | <i>58</i> |
| <i>Figure 4.8: Results of wavelet shaping. The figure on the top shows the raw P component and after wavelet shaping, bottom shows raw Z component and after wavelet shaping.</i> | <i>59</i> |
| <i>Figure 4.9: P and Z components and after wavelet shaping. Left side shows hydrophone data, right side shows geophone data. Red circles indicate the direct arrivals. Blue circles</i> | |

| | |
|--|----|
| <p>indicate primaries. Down-going wavefield (direct arrivals) has different polarity on hydrophone and geophone data.</p> | 60 |
| <p>Figure 4.10: Raw pressure (P) and vertical velocity (Z) components before PZ summation. The blue circles indicate the first water bottom multiples. The red circles indicate multiples.</p> | 63 |
| <p>Figure 4.11: Up-going and down-going wavefields after PZ summation. The left side shows down-going data, the right side shows up-going data. The blue circles indicate the first water bottom multiples. The red circles indicate multiples.</p> | 64 |
| <p>Figure 4.12: a) P component after wavelet shaping. b) scaled Z component after wavelet shaping. c) down-going wavefield after PZ summation. d) Up-going wavefield after PZ summation.....</p> | 65 |
| <p>Figure 4.13: Comparison of common-shot gathers for sparsely sampled acquisition (top), the spacing between receivers is 400 m, and common-shot gathers for densely sampled acquisition (bottom), the spacing between receivers is 25 m. Synthetic shot gathers were generated in VISTA by GEDCO.</p> | 67 |
| <p>Figure 4.14: Comparison of common-image gathers for sparsely sampled acquisition (top), the spacing between receivers is 400 m, and common-image gathers for densely sampled acquisition (bottom), the spacing between receivers is 25 m.....</p> | 68 |
| <p>Figure 4.15: Hyperbolic move-out velocity analysis of P component. The right side shows semblance. Purple corresponds to high and blue to low semblance. The left side shows traces in one CDP gather. The red plot on the traces indicates offsets of traces.</p> | 70 |

Figure 4.16: Illumination with sparse node geometry. The gaps in shallow reflectors coverage are noticeable. Shots are shown as red dots, live nodes are shown as yellow triangle, and dead node is shown as red triangle. (After Grion et al., 2007)..... 71

Figure 4.17: Conventional imaging of up-going wave (U) just below the sea floor..... 72

Figure 4.18: Ray paths of down-going (a) wave and mirror imaged down-going (b) wave. Down-going wave can be imaged as primaries recorded on a sea surface twice as high. The sea surface acts like a mirror for primary reflections. The down-going multiple is an up-going primary reflected downward at the sea surface. (After Grion et al., 2007) 73

Figure 4.19: Illumination of the up-going (a) wave and down-going (b) wave. It is clear that up-going wave has narrow illumination than down-going wave. Red circles are shows illuminated area. 74

Figure 4.20: KPSTM mirror imaging result with different constant velocities for Seatrial OBN data. The yellow circles indicates the events that are picked to create the velocity model..... 76

Figure 4.21: RMS velocity model for Seatrial OBN data from picked velocities..... 77

Figure 4.22: Mirror image with RMS velocity model. 78

Figure 4.23: Stacking velocity analysis window to update the velocity model from CIGs. The left side shows common image gathers, middle of the figure represents semblance window, and right side represents the stacked section. 79

Figure 4.24: Final updated RMS velocity model..... 79

Figure 4.25: Inline time migrated sections of the Seatrial OBN data. Conventional imaging of up-going waves (top) and mirror imaging of down-going waves (bottom). 80

Figure 4.26: Stacked image of PSTM up-going image and down-going image. 81

| | |
|---|-----|
| Figure 4.27: P-wave velocity volume in depth for Atlantis field (Gherasim et al., 2010). The black square area indicates our approximate area of coverage. | 83 |
| Figure 4.28: The final interval velocity model. The black circle indicates the salt body..... | 83 |
| Figure 4.29: The final interval velocity volume in 3D view. Chair display (top) and inline-crossline display (bottom). | 84 |
| Figure 4.30: Inline depth migrated sections of the Seatrial OBN data. Conventional imaging of up-going waves (top) and mirror imaging of down-going waves (bottom)..... | 85 |
| Figure 4.31: Stacked image of PSDM up-going image and down-going image..... | 86 |
| Figure 4.32: Synthetic RMS velocity model for a single inline..... | 88 |
| Figure 4.33: Synthetic interval velocity model for a single inline..... | 89 |
| Figure 4.34: Synthetic Up-going and down-going data for the same shot and same node. | 90 |
| Figure 4.35: Inline RTM sections of the synthetic up-going and down-going data. Conventional RTM of up-going waves (top) and mirror imaging RTM of down-going waves (bottom). | 91 |
| Figure 4.36: Inline RTM sections of the real Seabird OBN up-going and down-going data. Conventional RTM of up-going waves (top) and mirror imaging RTM of down-going waves (bottom). | 94 |
| Figure 4.37: Stacked image result of RTM up-going image and RTM down-going image. | 95 |
| Figure A.1: Offset and azimuth distribution in a CMP bin. Offset distribution is shown at the bottom for 6 specific bin grid. (Ashton, 1994)..... | 106 |
| Figure A.2: Fold distribution map for a 3D survey..... | 107 |
| Figure A.3: Fold versus signal-to-noise ratio (S/N), after Cordsen (2000)..... | 108 |
| Figure A.4: Signal-to-noise ratio (S/N) versus bin size, after Cordsen (2000)..... | 109 |
| Figure A.5: Fold versus bin size after Cordsen (2000)..... | 110 |

Figure A.6: *Xmin* definition with coincident source and receiver stations at corners of box, after Cordsen (2000).....111

Figure B.1. Reverberations between water surface and ocean-bottom (Modified from Hoffe et al. (2000))..... 112

Figure B.2. Up-going wavefield reflectivity, δ , and continuing receiver-side multiples. Modified from Hoffe et al. (2000).....114

Figure D.1: Construction stage of Vinton Dome model. Top left shows bottom layer of model and bottom figure shows finale shape of model (taken by Robert Wiley).121

Figure D.2: Dimensions of Vinton Dome model..... 122

Figure D.3: Schematic illustration of experimental setup on Vinton model. Receiver is located on the surface of the model. Source is located 200 m above the surface..... 123

Figure D.4: Schematic diagram of acquisition geometry. Drawing is not to scale. Red circles show shot locations, yellow triangles show receiver locations and brown plus symbols show hydrophone locations..... 124

Figure D.5: Location of source lines (red) and position of 6 ocean-bottom nodes in VISTA..... 125

Figure D.6. Common-receiver gathers from physical modeling data. The source spacing is 25 m. The red circle indicates the first water bottom multiples.....126

Figure D.7. A common-receiver gather from physical modeling data. The source spacing is 25 m127

LIST of Tables

| | |
|---|------------|
| <i>Table 1. Compare of VSP survey design parameter.....</i> | <i>17</i> |
| <i>Table A.1 Survey design decision table (after Cordsen, 2000.....</i> | <i>106</i> |
| <i>Table D.1: Physical properties of Black and Blue resin.....</i> | <i>120</i> |

LIST of ABBREVIATIONS

| | |
|--------------|-------------------------------------|
| AGL | Allied Geophysical Laboratories |
| CMP | Common-mid Point |
| CIG | Common-image Gather |
| CSG | Common-shot Gather |
| CRG | Common-receiver Gather |
| KPSDM | Kirchhoff Pre-Stack Depth Migration |
| KPSTM | Kirchhoff Pre-Stack Time Migration |
| NAZ | Narrow Azimuth |
| OBC | Ocean-bottom Cable |
| OBS | Ocean-bottom Seismometer |
| OBN | Ocean-bottom Node |
| RTM | Reverse Time Migration |
| VSP | Vertical Seismic Profile |
| WAZ | Wide Azimuth |

Chapter 1

INTRODUCTION

Subsurface imaging for clastic sediments by using 3D seismic surveys has been proven particularly successful; however, imaging geologies under complex overburdens such as salt body like the Atlantis Sigsbee basin in the deep water of the Gulf of Mexico is a still challenge in deep water (Orange, 2003).

Conventional narrow-azimuth (NAZ) streamer data can have large non-illuminated zones beneath complex geology. In this case, recording wide-azimuth (WAZ) seismic data can be helpful in reducing non-illuminated zones. Vertical seismic profiling (VSP) and ocean-bottom seismometer (OBS, OBC, or OBN) techniques can provide WAZ data; however, these techniques also have challenges of their own in deep water (Moldoveanu, 2006).

The conventional towed streamer method often provides high quality seismic data, but streamers have some limitations due to obstacles such as production platforms. These limitations motivate a quest for new and alternative technologies such as ocean-bottom nodes (OBN) and ocean-bottom cables (OBC) (Figure 1) which are the two main acquisition methods to acquire data on the seafloor. The OBN and OBC concepts are a development from ocean-bottom seismometers (OBS). The motivation for acquiring data on the sea floor is not only the obstacles. The other important

motivation for OBS is that OBS provides wide azimuth geometries. This is important key for imaging structures under complex overburdens such as subsalt (Grion, 2007).

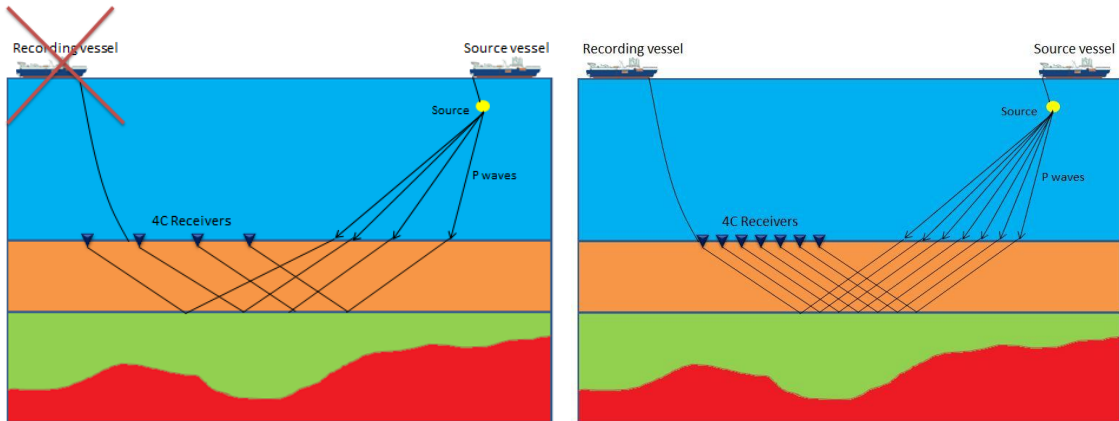


Figure 1.1: Ocean-bottom cable (OBC) (right) and ocean-bottom node (OBN) (left) acquisition. OBC is deployed on the seafloor and connected by electrical wires. OBN is also deployed on the seafloor; however, they are autonomous recording system.

The other advantage of ocean-bottom acquisition technologies is flexibility. Ocean-bottom nodes can be deployed almost anywhere. This flexibility gives us opportunity to combine the ocean-bottom nodes with other surveys such as VSP survey. There are various of VSP survey geometry such as 3D VSP with grids, walk away geometry, far and near offset VSP, and circular geometry (coil shooting, ring shooting, spiral and spokes shooting).

3D VSP with circular shooting has been used for 3D imaging near the borehole. VSP itself, however, still has some limitations such as poor offset and angular coverage per bin and limited total bin fold. This limitation in the VSP can be enhanced by combining ocean-bottom nodes on the sea floor with VSP survey.

In this work, many survey designs created in OMNI 3D Survey Design software by GEDCO (Geophysical Exploration and Development Co.). Joint OBN and VSP survey design created to achieve better offset and azimuth distribution than VSP survey itself.

The compressional-wave images of the subsurface can be obtained by OBN seismic data. Water-layer reverberations are well known problem with conventional streamer seismic data. The compressional-wave images for OBN recordings have fewer water layer reverberations than image obtained from streamer seismic data. The up-going P-wave and down-going P-wave recorded on the sea floor by multi-component ocean-bottom nodes can be separated by combining the vertical component (Z component) and pressure component (hydrophone). This process is called PZ summation. Details on the PZ summation process are mentioned by Soubaras (1996).

The ocean-bottom node seismic data, which are used in this study, were provided by Seabird Exploration. The Atlantis Seatrial 3D-4C OBN survey was acquired by SeaBird Exploration in 2009 over the Atlantis field at Gulf of Mexico. A total of 41 nodes were used at 17 locations on receiver lines to record the data from the sea bottom.

The Seatrial OBN data set were used to process and image the data from ocean-bottom. Since the OBN acquisition has high cost, a sparse receiver interval is usually used to acquire the data. This type of acquisition has several problems, such as

illumination. The illumination, specifically of the shallow surface, is poor because of sparse receiver locations (Alerini et al., 2009).

The large receiver spacing causes the poor continuity of event in common-shot gathers, common-mid point (CMP) and common-image gathers (CIGs). Because of this poor continuity, velocity model estimation will fail or be difficult. These difficulties motivated me to image the data in receiver domain from down-going waves. Both up-going and down-going waves were imaged to understand the improvement in the illumination of shallow area.

It is impossible to mention all aspects related with ocean-bottom acquisition in single dissertation. In this work, I focused on PZ summation and imaging up-going and down-going wavefields (Mirror Imaging). Imaging via Kirchhoff Pre-stack Time Migration (PSTM) and Reverse Time Migration (RTM) were performed for synthetic data and real data from Seatrial Atlantis Field for OBN type data acquisition. Software packages Vista by GEDCO, Echos and GeoDepth by Paradigm were used in this study to process and image the data. For imaging the data sets, Allied Geophysical Laboratories (AGL) and Paradigm's powerful computers were used.

1.1. Motivation to Deploy Ocean-bottom Node Technology

Some of the advantages of seismic acquisition using OBN technology can be listed as:

1) The wide-offset and wide-azimuth geometry can be designed to illuminate structures under complex overburdens such as subsalt. The Figure 1.2 clearly shows that the illumination under salt model for receiver migrated node acquisition is much better than conventional narrow azimuth towed streamer.

2) Shots within each receiver bin can provide full-azimuth coverage with suitable fold and offset coverage.

3) Dense source array with sparse OBS receiver array can provide uniform wave field sampling.

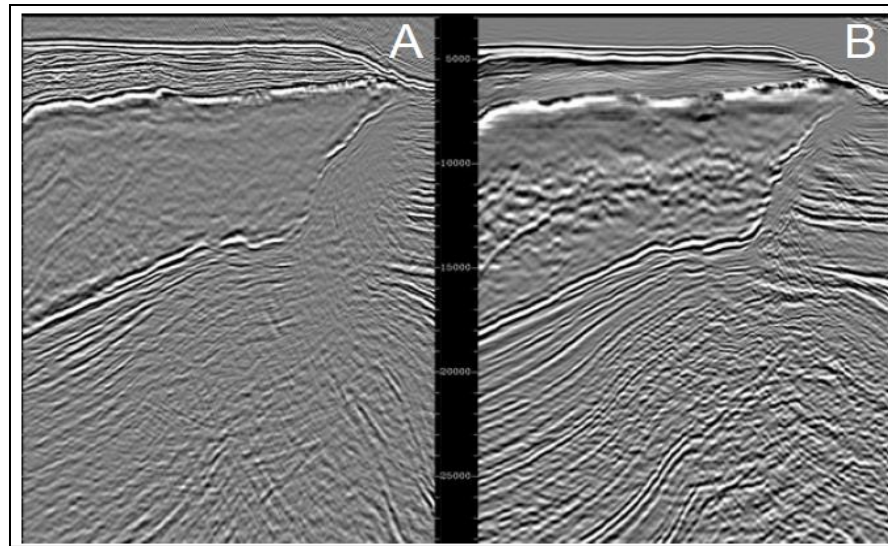


Figure 1.2: Comparison of narrow azimuth towed streamer (A), and receiver migrated OBS node (B). The node images benefit from the improved salt model (Beaudoin, 2010).

4) Node seismic has higher resolution both vertically and laterally than narrow azimuth towed streamer (NATS) seismic because of high fidelity sensors recording in low noise environment. (Figure 1.3)

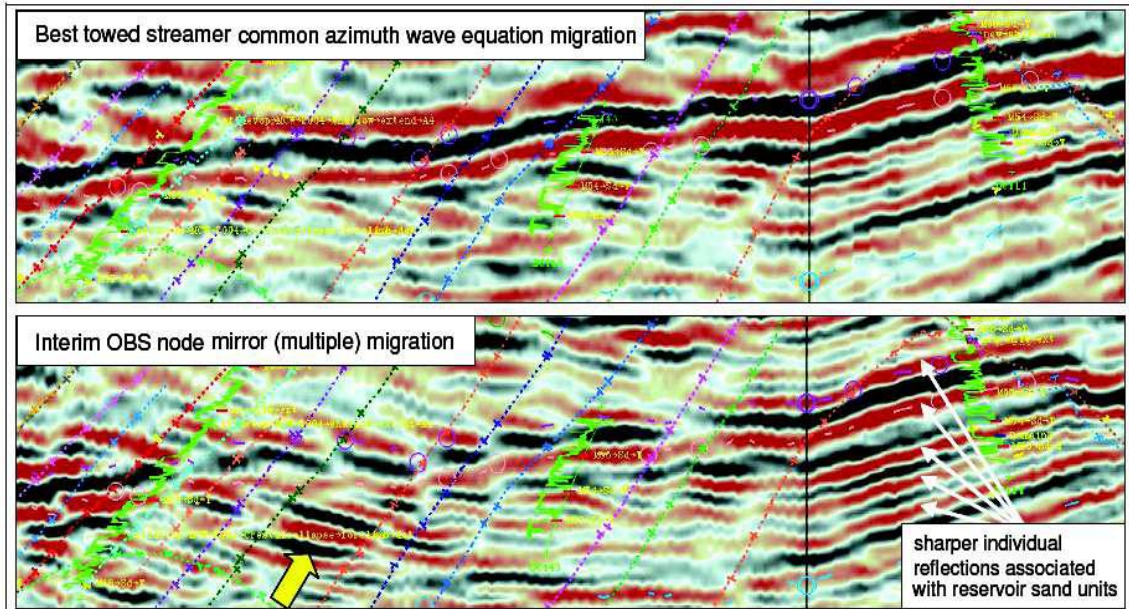


Figure 1.3: Comparison of extra-salt images at the Miocene level at Atlantis. Higher resolution and improved fault definition are apparent in the OBS wide-azimuth node image on the bottom compared to the narrow-azimuth towed streamer image above (Howie et al. 2008).

5) Up-going and down-going waves can be separated at the seafloor for multiples attenuation or imaging using the multiples (Maxwell, 2007) (Figure 1.4).

6) Seismic acquisition is less affected by surface weather conditions.

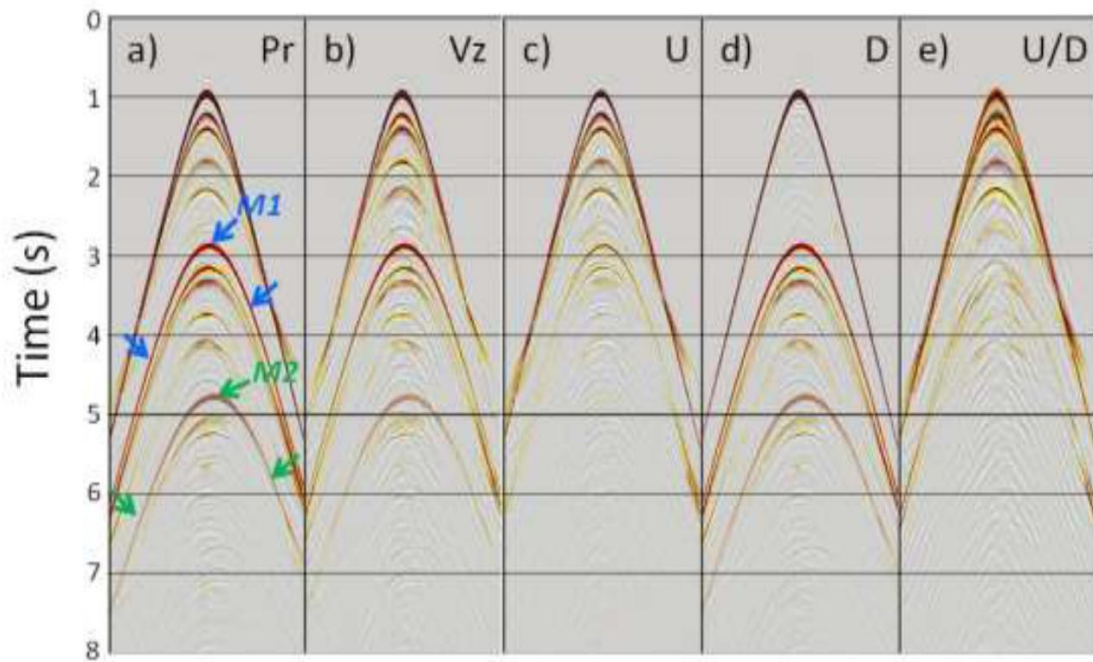


Figure 1.4: Wavefield separation. From left to right, a common receiver gather (CRG) for a) pressure, b) vertical component of particle velocity, c) up-going wavefield, d) down-going wavefield, and (e) the up-down deconvolution result. Events M1 and M2 are the first and second order water-layer multiples (Wang, 2010).

7) Both P-waves and S-waves can be recorded.

Analysis of the shear waves is one of the advantages of the OBN data. The PS section of the OBN data can be useful in several areas such as identification of hydrocarbons and gas presence. Due to shear waves are not affected by presence of gas, they can help to identify the subsurface image.

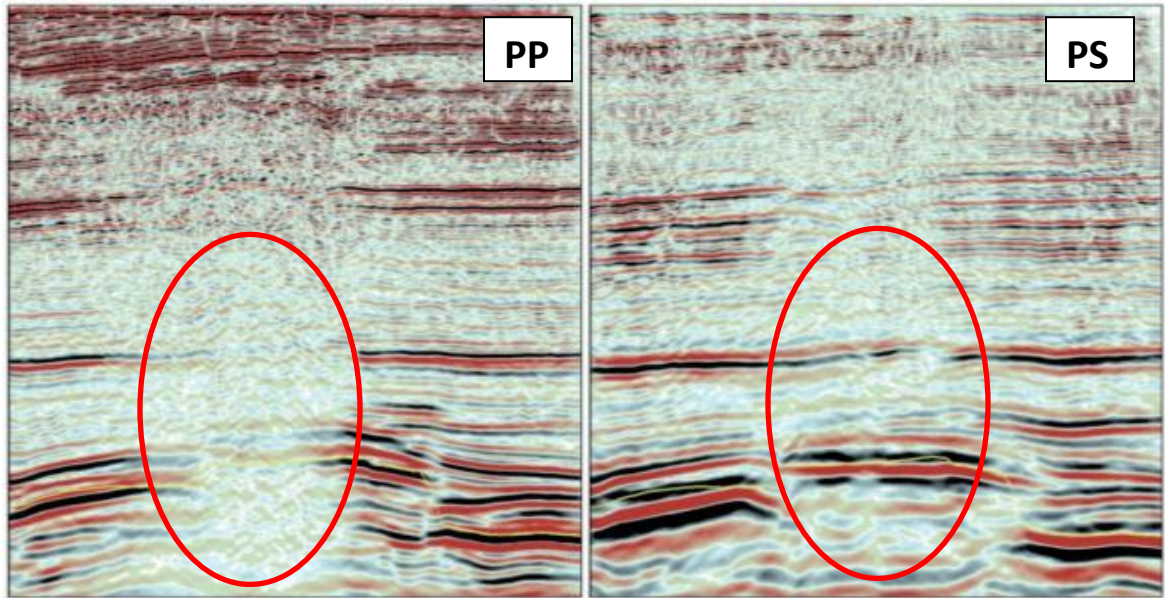


Figure 1.5: PP and PS imaging. The PS image (right) reveals details of the reservoir which are hidden on the PP image (left) by effects from the shallow gas (Ronholt et al., 2008)

Multicomponent acquisition and processing can provide better and improved imaging compared to conventional data. The amplitude of P-waves passing through the gas is attenuated. This causes structural distortion because of the low velocities in the vicinity of the gas. This affects events beneath the gas giving rise to false structure. Unlike P-waves, S-wave amplitudes are undiminished and so provide clear images under the gas.

Figure 1.5 shows the example of PP and PS imaging. It is clear that the converted wave (PS) images provide a better continuity of the seismic events beneath the shallow gas (annotated with red circles) compared to the compressional PP images.

The other advantages of OBN data are time-lapse (4D) repeatability, vector fidelity of the seismic wavefield, vector decomposition, coupling of geophones with the ocean-bottom, and PZ summation.

Chapter 2

OBN, VSP and JOINT OBN-VSP SURVEY DESIGNS

2.1. Ocean-bottom Acquisition Techniques

To provide large-scale information for crustal studies and lithospheric investigations, ocean-bottom seismometers (OBS) (Figure 2.1) have been used for many years by universities and oceanographic research groups (Maxwell, 2007).

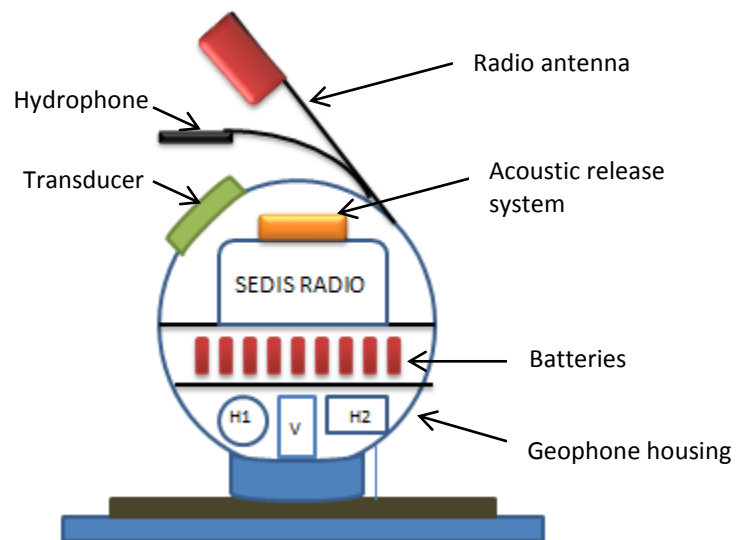


Figure 2.1: Ocean-bottom Seismograph (OBS) consist of 3 component geophones and a hydrophone (Modified from GeoPro ocean-bottom seismograph).

The advantages of OBS technique were mentioned earlier by Zachariadis et al. (1983). They indicated that advantages of OBS technique: deployment and recovery of

OBSs are generally straight forward, low signal to noise may be obtained and geophones may be used with hydrophones. This technique also has been overviewed by Loncarevic et al. (1983). According to them, this technique was first used in the mid-1930s; however, the expectations were not fulfilled because the noise at marine sites was not much lower than land surveys. The other problems were instruments cost, complexity, and unreliability. According to Zachariadis et al. (1983), Mobil Oil Co. evaluated the use of academic OBS designs for refraction work in 1975.

Ocean-bottom Cable (OBC) surveying is modified from conventional streamers to lie on the sea bottom (Gallant et al. 1996). Figure 2.2 shows the schematic illustration of OBC receiver array on the sea floor. Usually, at least two vessels are used to acquire the data from ocean-bottom in the OBC technique. One of these vessels records the information from the ocean-bottom. Another vessel carries the source. The OBC technique can be used as a dual-sensor cable laid on the ocean floor, which records both the velocity and pressure signals (Figure 2.3). The dual-sensor systems have been used to attenuate the receiver side ghost from the recorded seismic data (Gallant et al. 1996).

One of the first acquisitions with OBC technique is reported by Zachariadis and Bowden (1986). According to the authors, this technique was used in areas where there are navigational obstacles such as production or exploration platforms or buoys. The authors also mentioned other advantages of OBC technique such as better positioning and uniform acquisition pattern.

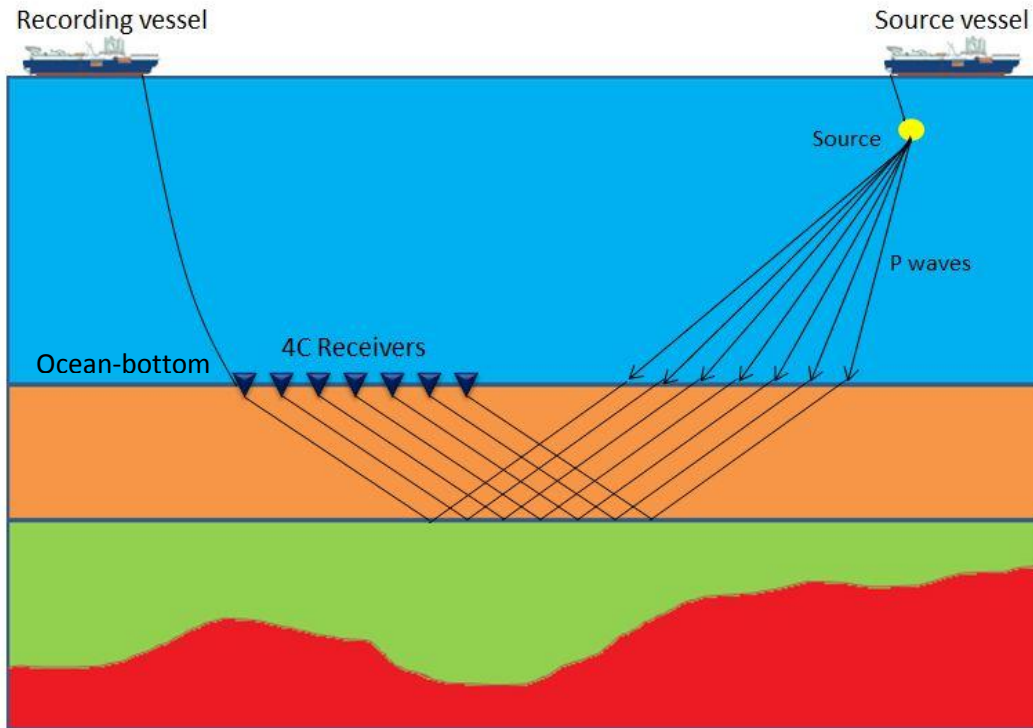


Figure 2.2: Schematic illustration of OBC receivers lay on the sea bottom. 4C receivers record the velocity and pressure.

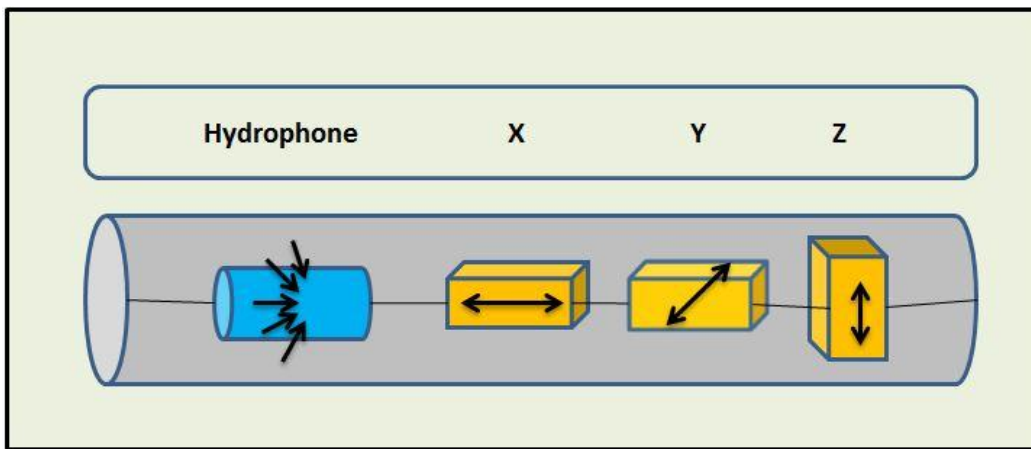


Figure 2.3: Examples of 4-C receivers in an ocean-bottom cable (*modified from Caldwell et al., 1999*). From left to right, the hydrophone (pressure sensitive), radial (inline), transverse (crossline) and vertical components.

The Ocean-bottom seismometer technique (OBS) which has been used for several decades was the pioneer in the development of ocean-bottom node concept.

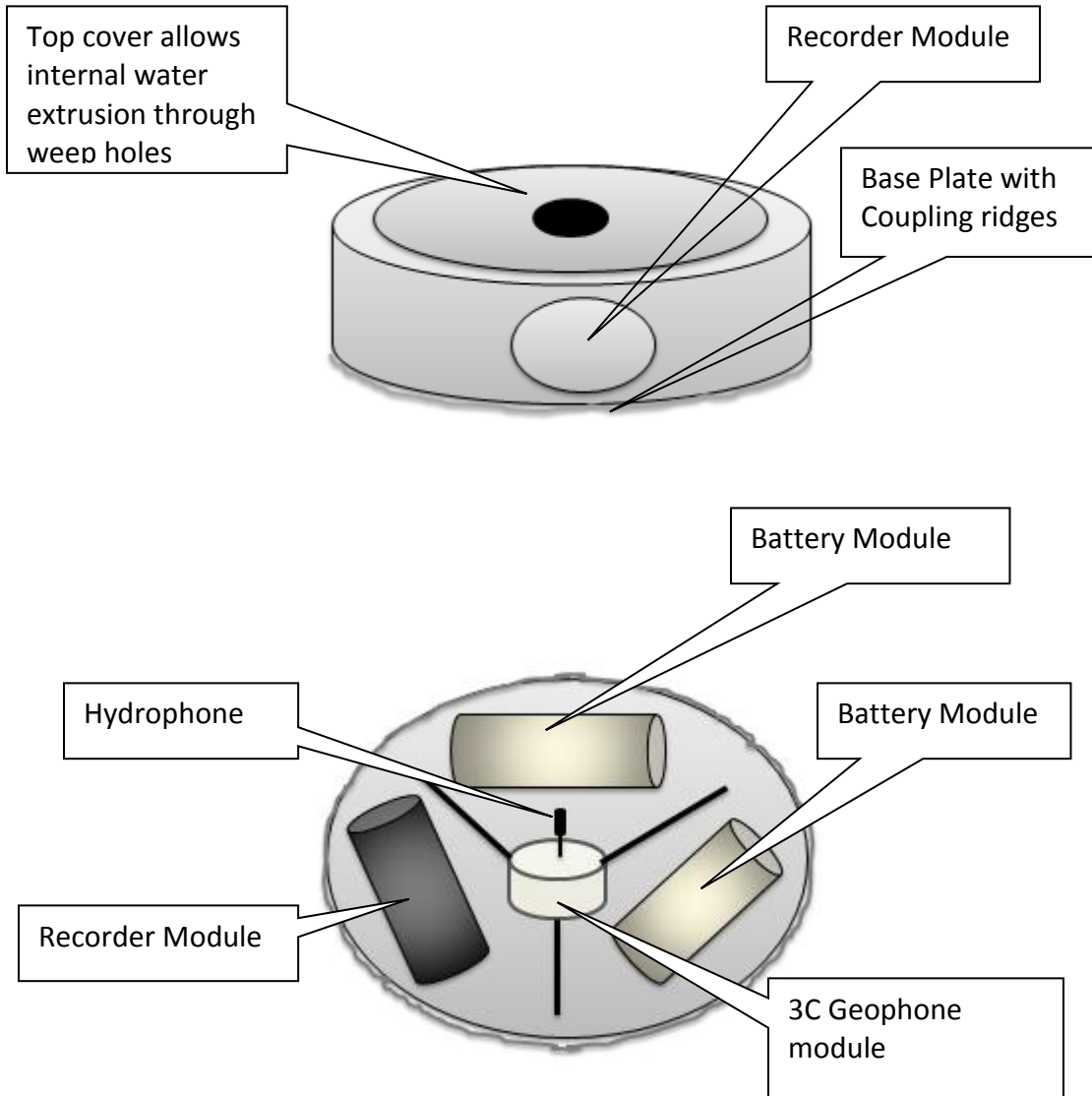


Figure 2.4: Ocean-bottom node system consists of 3C geophone module, hydrophone, and battery and recorder module. Top figure shows node with cover, bottom show node without cover Modified from Fairfield ocean-bottom node.

The ocean-bottom nodes (Figure 2.4) are autonomous seismic recording units operating on the seafloor while a source vessel shoots lines above. The ocean-bottom nodes record 4C (four components) data; three components geophone to record seabed motions and a hydrophone to record water-borne pressure.

Between 2000 and 2005, OBNs were used for the BP's Atlantis OBS project in the Gulf of Mexico. According to Howie et al. (2008), this project was the world's first 3D deepwater and wide-azimuth ocean-bottom seismic acquisition. The results (Figure 2.5) show that 3D OBN data has higher resolution, excellent reflector continuity, and improved structural definition in Atlantis field, compare with the existing streamer data (Howie et al. 2008).

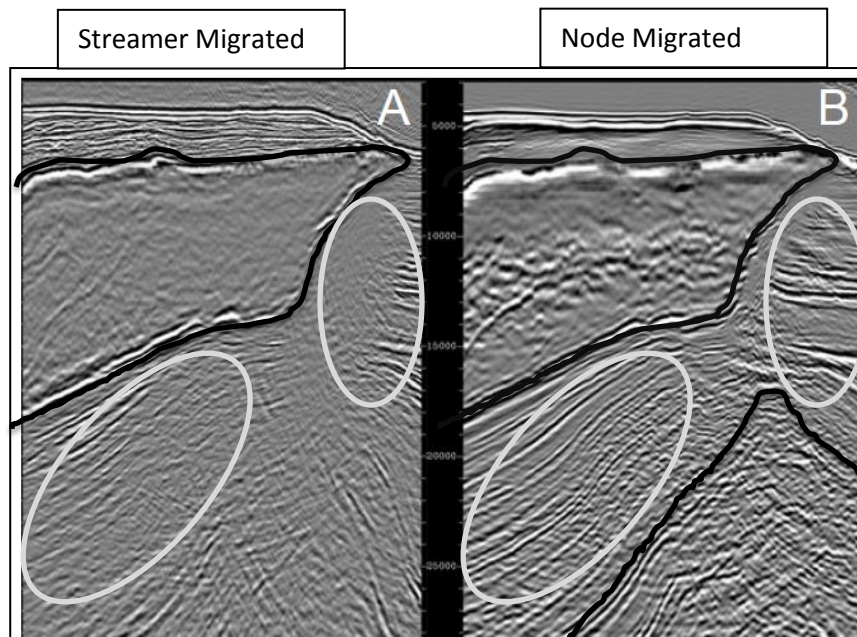


Figure 2.5: Imaging comparison at Atlantis of 3D conventional marine seismic (left) and receiver migrated 3D OBN seismic (right). The node images benefit from an improved salt model (Howie et al., 2008) Courtesy BP.

2.2. VSP Survey Design

Borehole seismic surveys have a long history of providing rock properties such as interval velocity, impedance, and attenuation near the borehole (Stewart and Gulati, 1997). To image and estimate rock properties near or between wells, in situ measurements such as VSP, reverse VSP and cross surveys have proven useful (Zhang, 2005).

3D offshore vertical seismic profile (VSP) has been successfully proven to improve seismic imaging of complex structural and stratigraphic features (Ray et al., 2003; Hornby et al., 2006) and recently has been used for imaging “blind spots” in surface seismic coverage (Hornby et al., 2005; Hornby et al., 2007).

There are various of VSP survey geometry such as 3D VSP with grids, walk away geometry, far and near offset VSP, and circular geometry (coil shooting, ring shooting, spiral and spokes shooting). In this study, I use circular shooting geometry to create survey designs.

Burch et al. (2010) reported 3D VSP survey in the deepwater Gulf of Mexico with circular geometry. According to author, circular sail pattern was chosen as the most effective shot geometry for this survey. Totally 17,000 shots were acquired with offset up to 6000 m (Burch et al, 2010). Figure 2.6 shows the circular shot geometry of this survey.

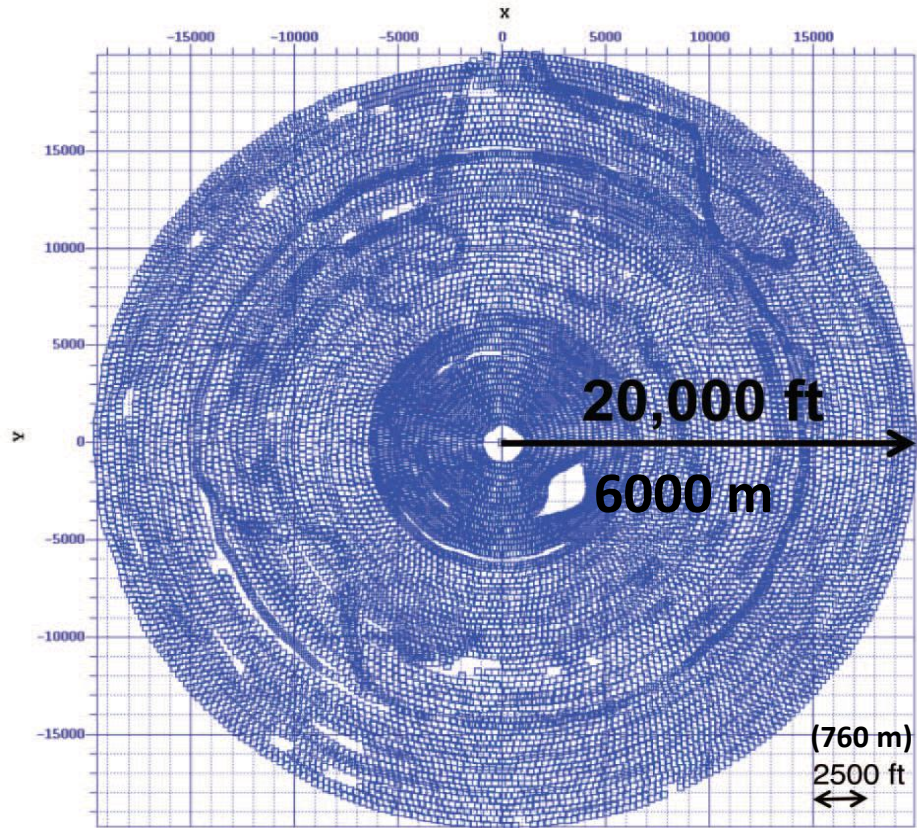


Figure 2.6: Map of shots geometry in a circular pattern for 3D VSP (Burch, 2010)

In this study, OMNI 3D survey design software is used to create VSP surveys. OMNI 3D from Geophysical Exploration and Development Co. (GEDCO), Calgary is an industry-standard software package for seismic survey design and modeling.

First a 3D VSP marine survey with circular shooting geometry was created to assess azimuth and offset distribution. We created 4 different surveys with different shot and receiver numbers in order to compare surveys. The survey parameters for these VSP surveys can be seen in Table 1.

| | # of Shots | # of Receivers | Max Depth fold |
|--------------|------------|----------------|----------------|
| VSP Survey 1 | 686 | 50 | 48 |
| VSP Survey 2 | 2760 | 50 | 149 |
| VSP Survey 3 | 1378 | 25 | 41 |
| VSP Survey 4 | 1378 | 100 | 185 |

Table 1. Compare of VSP survey design parameters

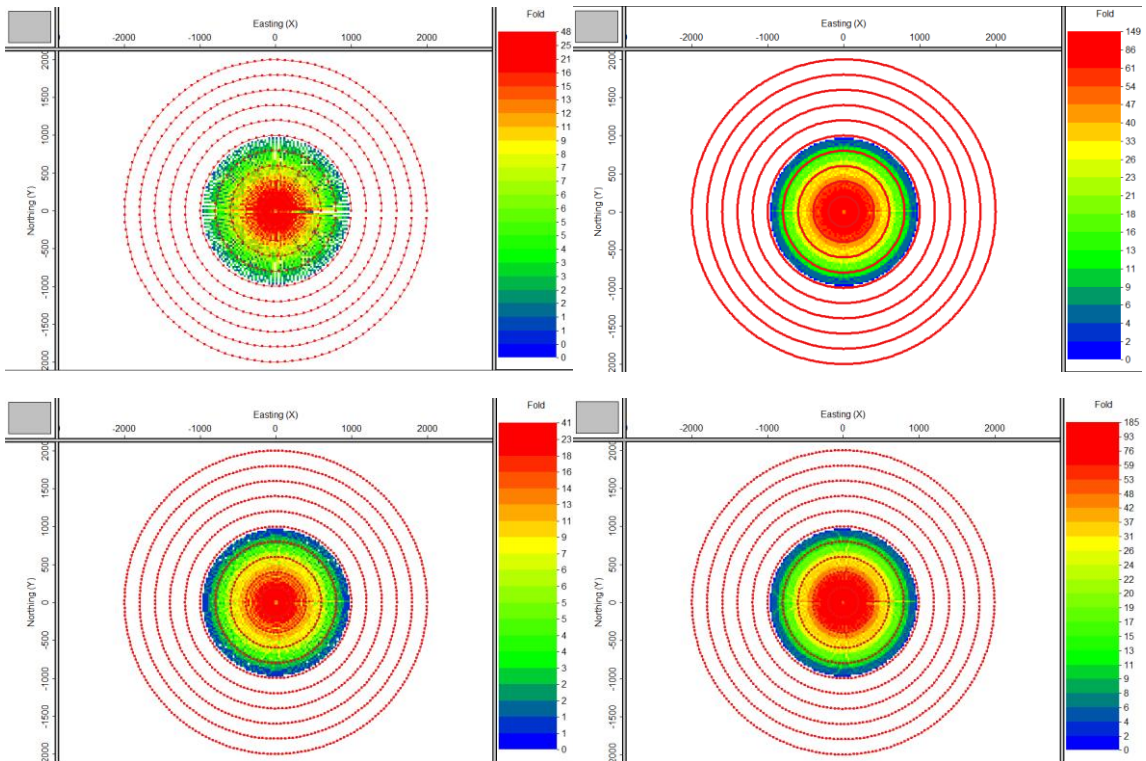


Figure 2.7: Depth Fold map of VSP survey designs with different parameters. The left top is Survey 1, right top is Survey 2, the left bottom is Survey 3, and the right bottom is Survey 4.

It is clear that increasing the number of shots increases the maximum depth fold. Since increasing the number of shots effect the cost of survey, the ideal sea surface source distribution for this VSP survey ends up with 10 concentric circles, separated by 200 m, radiating out from the well containing the borehole geophone array because of the economical and practical reasons. The shooting interval for each circle is 50 m. There are total 50 borehole receivers with 50 m interval (Figure 2.8).

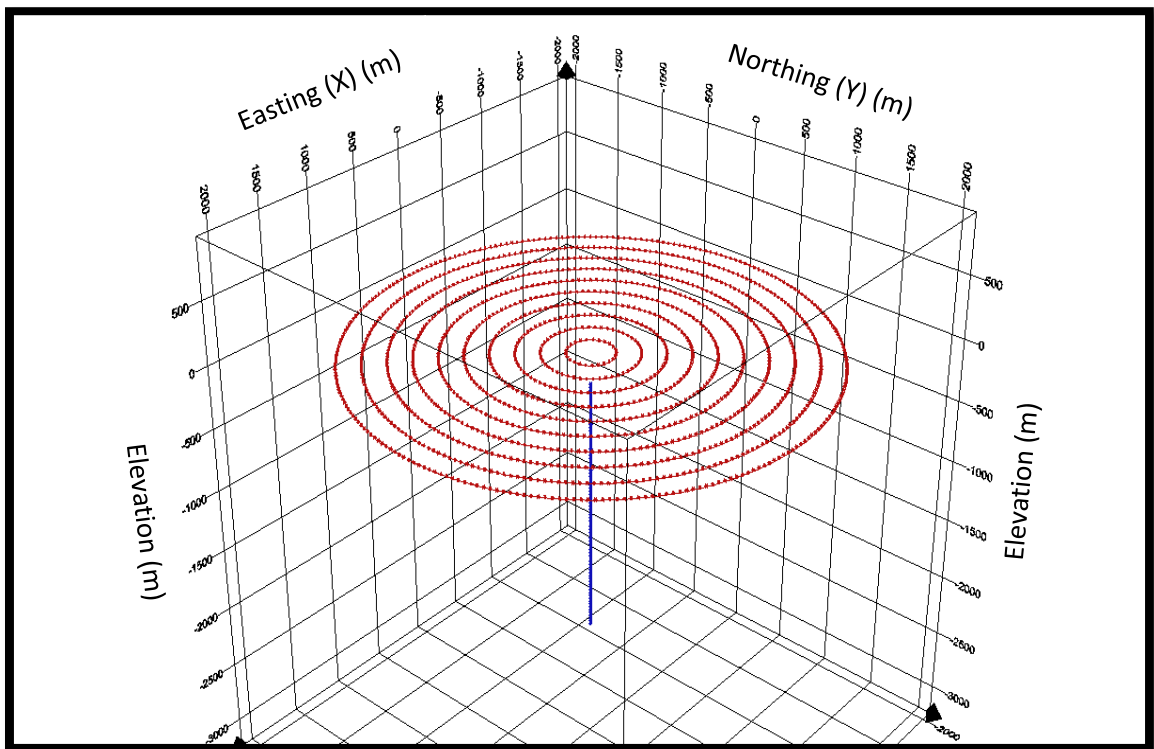


Figure 2.8: VSP source and receiver positions on 3D view. Red symbols represent shot locations (10 concentric circles) and blue symbols represent receiver locations.

It can be clearly seen in Figure 2.9 that area close to center of circles (near offsets) has higher and better fold distribution. For this survey, maximum fold around center is 88 CMP fold.

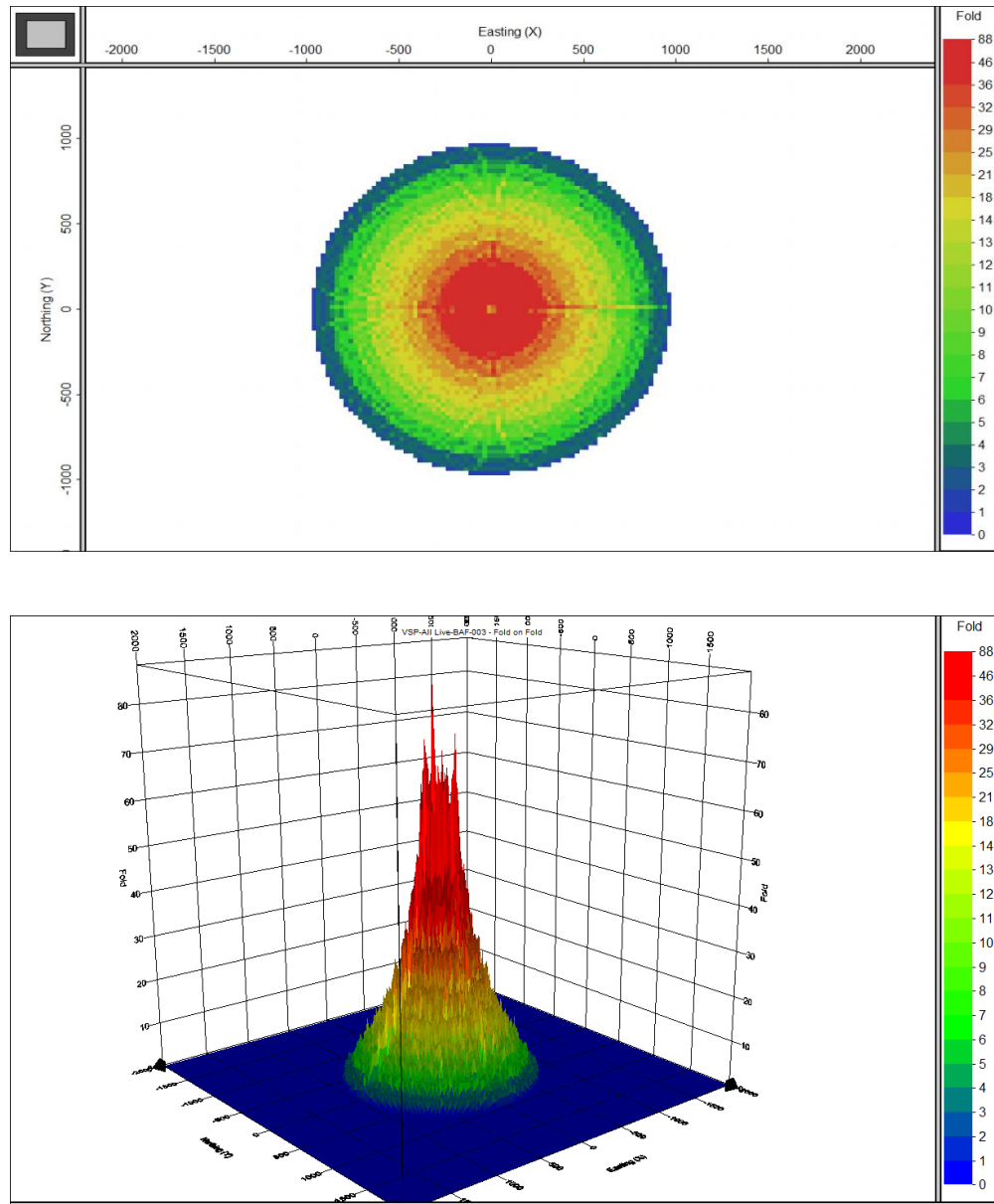


Figure 2.9: Fold map of 3D VSP survey with circular shooting geometry (10 concentric circles). The top shows a plane view of fold distribution and bottom shows 3D view. The red color indicates maximum fold, blue indicates minimum fold.

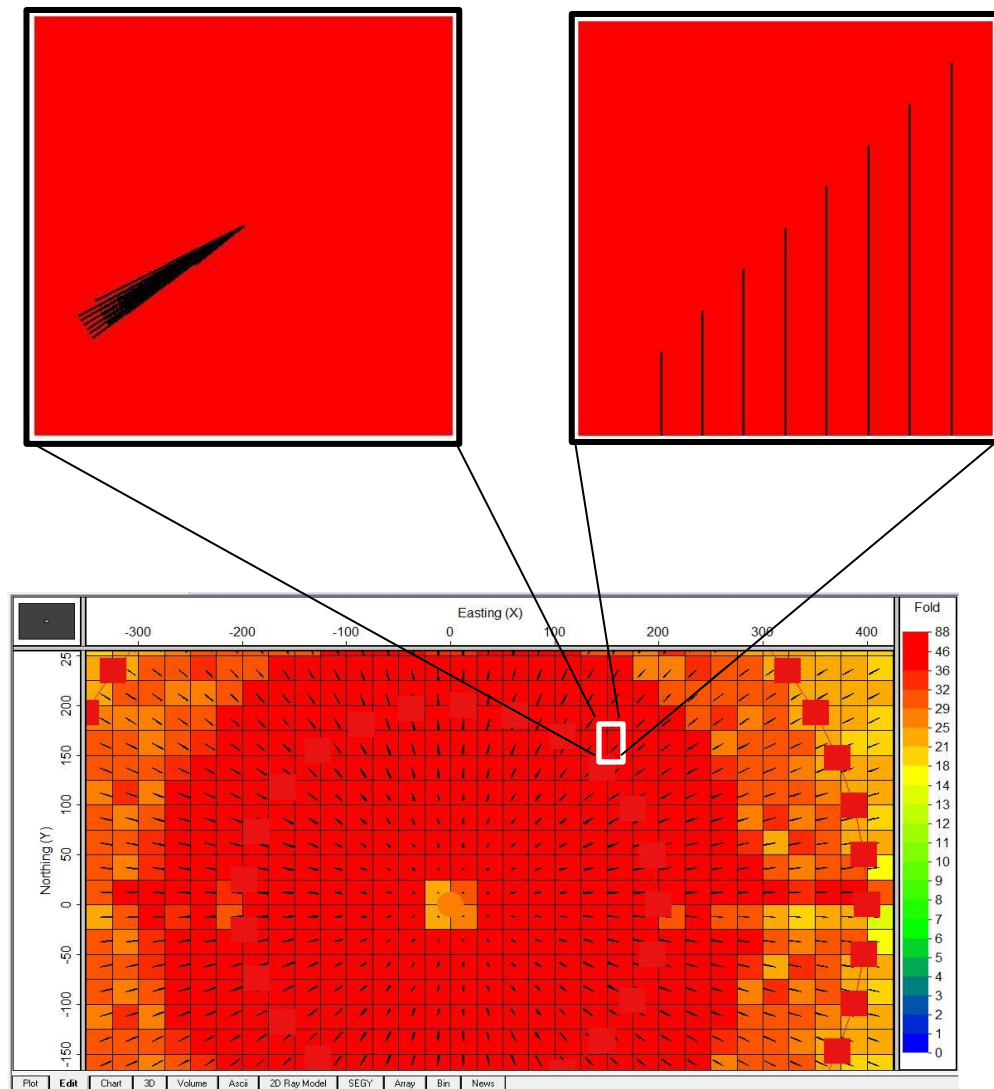


Figure 2.10: Azimuth and fold distribution for selected bin grid. Top left shows azimuth, right shows fold, and bottom shows selected partial bin grid.

From Figure 2.10, it can be noticed that VSP has still limitations such as suffering from restricted angular coverage per bin, poor offset coverage, and limited total bin fold. Solution for VSP limitations will be discussed in following sections.

2.3. Ocean-bottom Node (OBN) Survey Design

Ocean-bottom node surveys are usually shot with a dense shot carpet. Figure 2.11 shows an example with 16.85m x 46.5m shot interval/source line interval. The most common geometries in 3D OBN seismic acquisition are orthogonal and parallel geometry with dense shot carpet. Based on this standard geometry, receiver locations on the sea floor and source locations on the sea surface can be regularized.

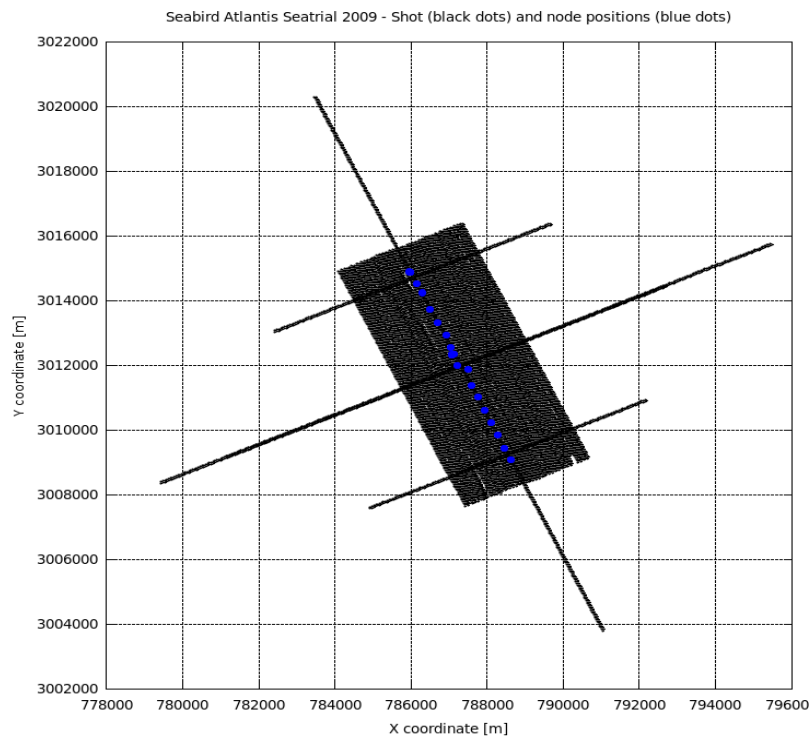


Figure 2.11: Example of dense shot carpet geometry from Atlantis Seatrial survey. Blue points show nodes locations and black dots show shot locations.

In this work, I created survey design for 3D OBN seismic with circular shooting. This circular shooting geometry with OBN survey compared in azimuth and offset distribution with regular OBN surveys.

In 2009, Apache Co. decided to acquire 3D seismic data to image shallow gas accumulations at Fortis field, North Sea. However, towed streamers were not able to acquire data near or under existing platforms. Because of this limitation Apache decided to use ocean-bottom nodes to image directly under platform (Koster, et al., 2011). A total of 154 nodes deployed on the sea floor by hexagonal receiver geometry with 58 m receiver intervals. 10 m shot interval was used to acquire the data (Figure 2.12).

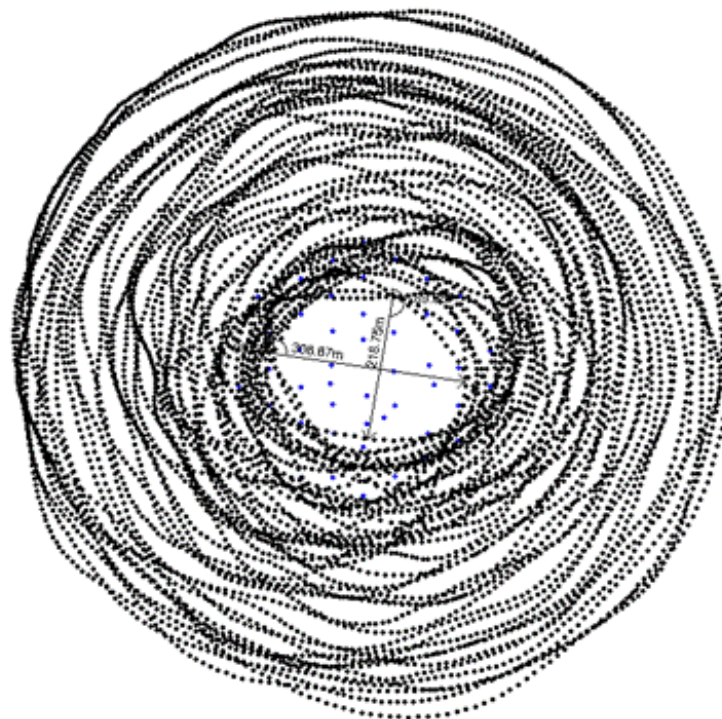


Figure 2.12: Hexagonal receiver location (blue dots) under platform with 58 m interval, circular shooting geometry (black dots) with 10m shot interval and 10, interval between circles (Apache Co., 2009).

To test circular shooting geometry with ocean-bottom survey, first I created regular OBN survey with orthogonal source and receiver geometry. A total of 100 nodes are located on the sea floor (500 m water depth) with 400 m intervals. There is 200 m indent between receiver lines. Dense shot carpet geometry, which has orthogonal shot lines, was used to generate source geometry on the nodes. The distance between shots is 25 m shot interval with 50 m shot line interval. This survey has total 41276 shots. Different shot and shot line intervals were used to create a survey with the same number of shots in the circular shooting geometry (Figure 2.13). The survey parameters were calculated based on Cordsen's criteria. The Cordsen's criteria for 3D survey can be found in Appendix A (fundamental of survey design).

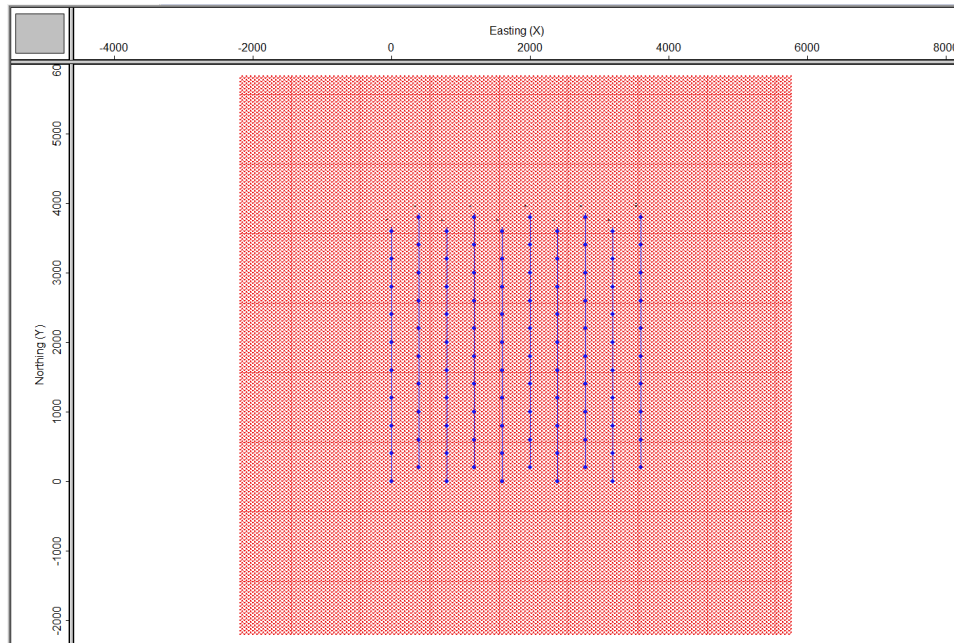


Figure 2.13: Receiver locations (blue dot) and dense shot (red dots) carpet geometry for orthogonal OBN survey.

Orthogonal shot lines on the marine surveys require turning the vessel 180 degrees to start shooting new line. Turning vessel causes additional cost and waste of time. These disadvantages of orthogonal line shooting motivate me to create survey with circular shooting geometry.

Figure 2.14 shows source and receiver locations for circular shooting geometry with OBN survey. The survey consists of 41188 shots. 25 m source interval with 25 m circle interval was used to optimize the area of coverage. The same receiver geometry and water depth with previous design was used to located nodes on the sea floor.

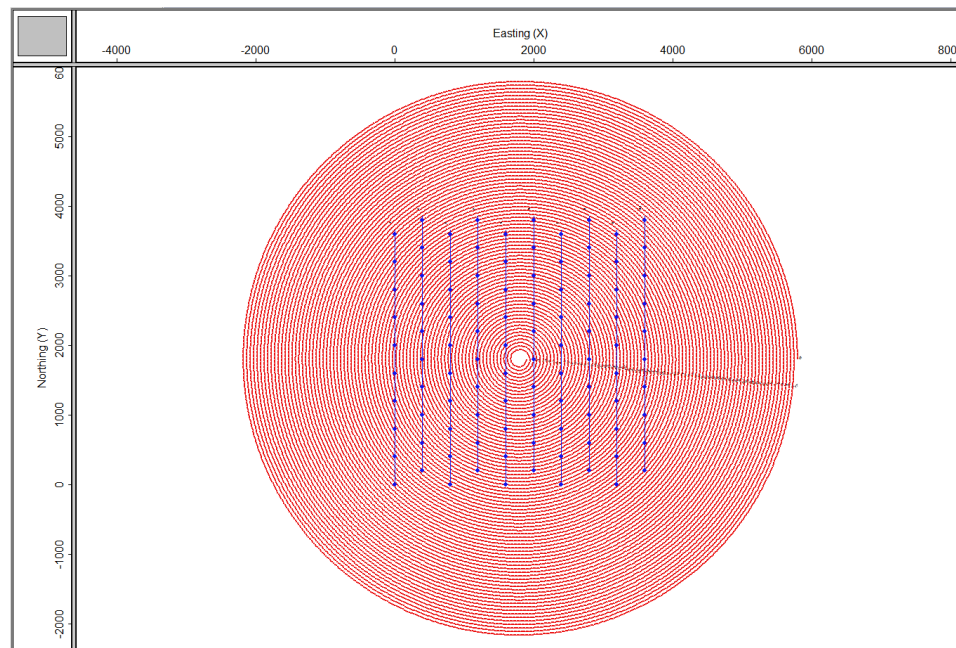


Figure 2.14: Circular shooting geometry with ocean-bottom nodes. Red dots represent source locations and blue dots represent receiver locations.

Fold distribution for both orthogonal lines and circular shooting geometry can be seen in Figure 2.15. The top of Figure 2.15 shows the fold distribution for OBN survey with circular shooting, and the bottom part shows the fold distribution for OBN survey with orthogonal lines shooting geometry. The figure clearly shows that circular shooting has more even fold distribution than orthogonal shooting: however orthogonal shooting has better fold coverage.

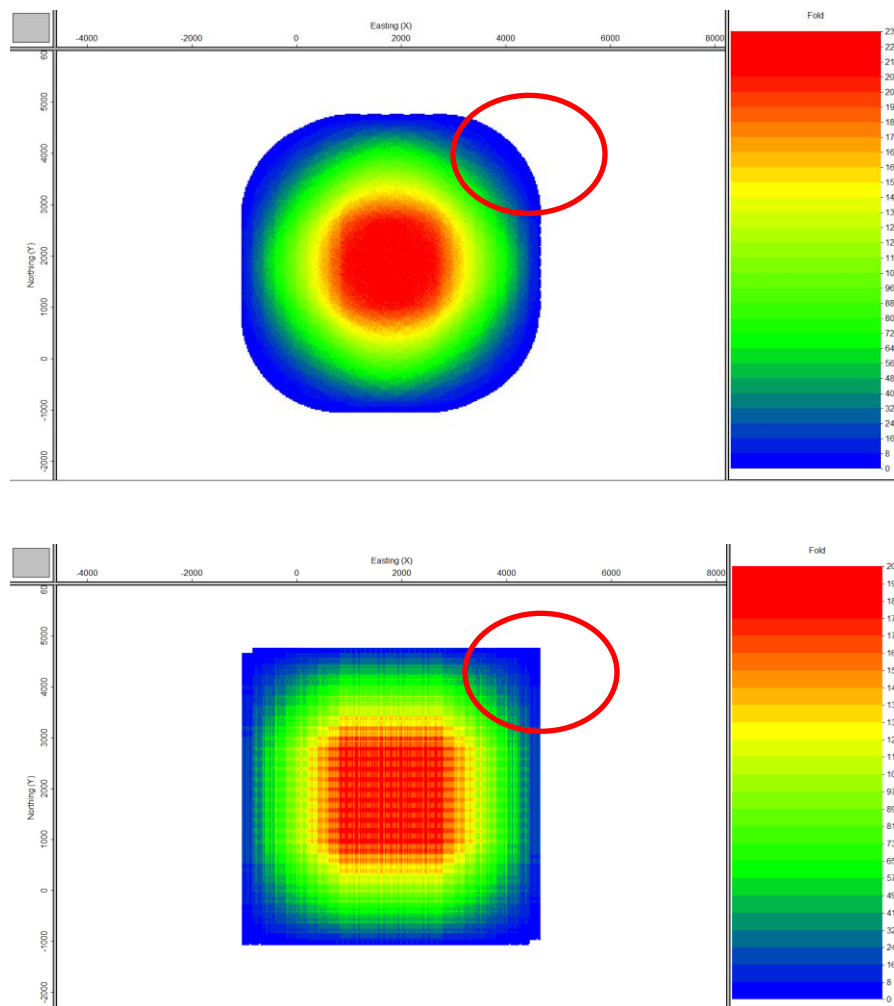


Figure 2.15: Fold distributions for OBN surveys. The top figure shows circular shooting fold distribution and the bottom shows orthogonal shooting fold distribution.

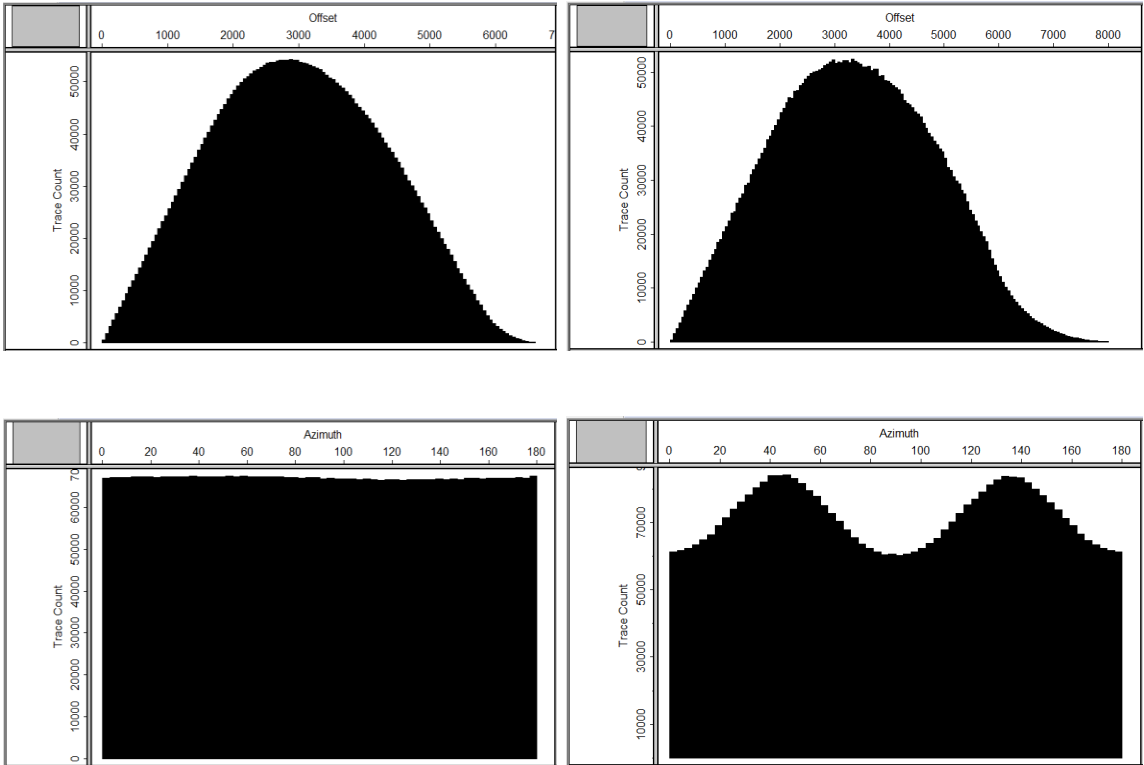


Figure 2.16: Comparison of azimuth (bottom) and offset (top) coverage for both surveys. The left charts are offset and azimuth distribution for circular shooting and the right charts are offset and azimuth distribution for orthogonal shooting.

Azimuth and offset coverage for both surveys are compared in Figure 2.16. The top charts show the number of traces that fall in each range of offset values. The bottom charts represent the number of traces that fall in each range of azimuth values. From Figure 2.16, it can be seen that circular shooting geometry has better offset and azimuth distribution than orthogonal survey.

Figure 2.17 shows the comparison of circular shooting geometry and orthogonal shooting geometry in rose diagram. This diagram colored by the number of traces that

fall in each sector, defined by offset steps (50 m) and azimuth steps (10°). Figure 2.17 also shows that azimuth distribution is better in circular shooting geometry than orthogonal shooting geometry.

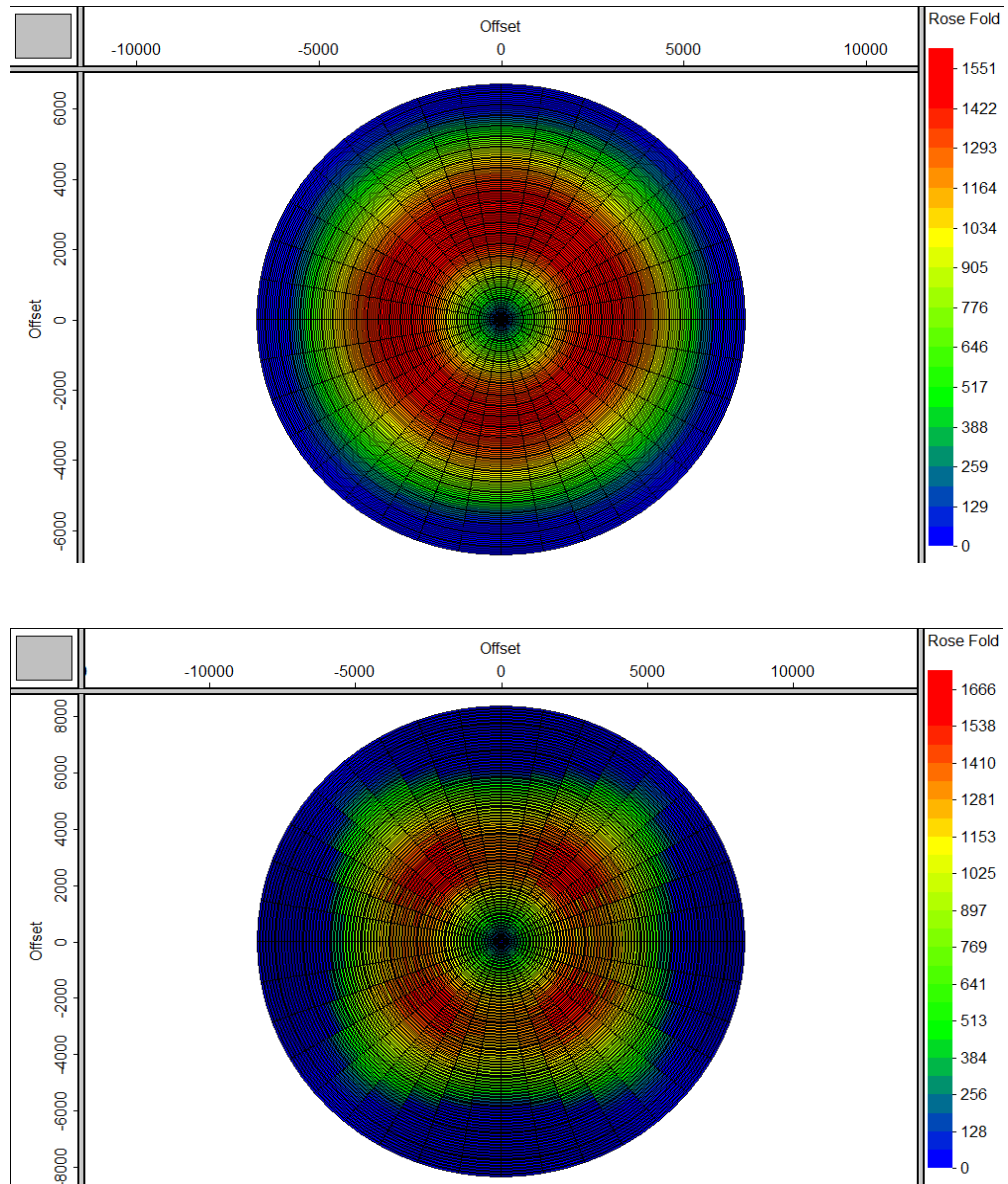


Figure 2.17: Comparison of circular shooting geometry (top) and orthogonal shooting geometry (bottom) in rose diagram.

Figure 2.18 shows also azimuth and offset distribution azimuth and offset distribution in selected bin grid for circular and orthogonal shooting geometry. Circular shooting azimuth and offset distribution are shown in top part of the figure. Left top shows spider diagram of circular shooting, and right top shows offset distribution.

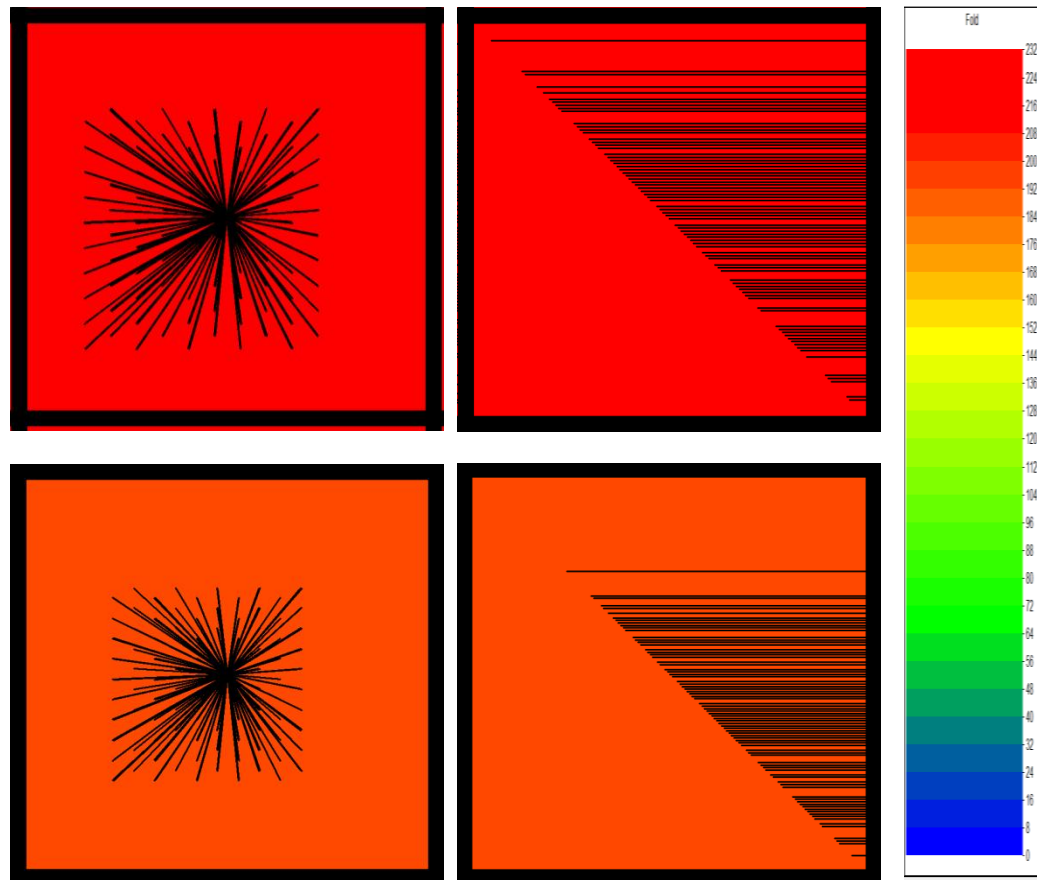


Figure 2.18: Azimuth and offset distribution in selected bin grid for circular and orthogonal shooting geometry. Top left shows azimuth distribution and top right shows offset distribution for circular shooting. Bottom left represents azimuth distribution and bottom right offset distribution for orthogonal shooting.

It can be clearly said that ocean-bottom node survey with circular shooting has better fold and offset distribution than orthogonal shooting. Another advantage of circular shooting is that circular shooting needs less time and cost than orthogonal shooting to complete the same survey.

Wide-azimuth data can be acquired by 3-4 seismic vessels to improve the quality of complex overburden imaging. However, in comparison with parallel WAZ acquisition geometry, a single vessel with circular shooting geometry can deliver some advantages such as a better range of azimuth, fold, and offset distribution (Moldoveanu, 2008).

2.4. Joint OBN-VSP Survey Design

As mentioned earlier in the chapter, 3D VSP with circular shooting has been used for 3D imaging; however, it still has some limitations such as poor offset and angular coverage per bin and limited total bin fold with 3D VSP survey.

In this study, I created a survey design by combining ocean-bottom nodes with VSP survey. The idea was that these limitations in the VSP can be overcome by combining ocean-bottom nodes on the sea floor with VSP.

VSP survey design was reviewed in section 2.2. To see improvement in azimuth and offset coverage, I combined ocean-bottom nodes with this VSP survey and created a new survey design. For this new survey, the same concentric circles with VSP survey were used to generate source geometry, 10 concentric circles, separated by 200 m, radiating out from the well containing the borehole geophone array. The shooting interval for each circle is 50 m.

There are total 50 borehole receivers with 50 m interval. Ocean-bottom nodes geometry on the sea floor is based on 200 m sparse receiver grid (200x200 m). A total of 100 nodes are combined with the VSP survey (Figure 2.18).

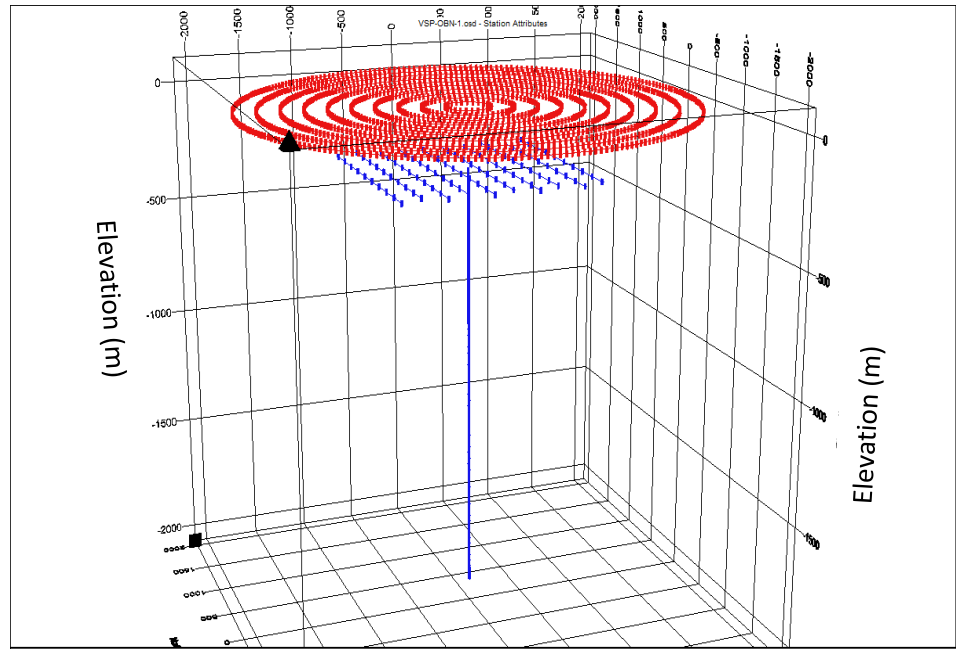


Figure 2.19: 3D view of source and receiver locations for joint OBN-VSP survey. Red circles shows shots, and blue point shows VSP receiver and ocean-bottom node locations.

Figure 2.19 shows fold distribution in plain and 3D view for VSP survey itself, and Figure 2.20 shows fold distribution for joint OBN-VSP survey. Improvement in fold coverage for joint survey can be easily noticed from 3D view. Maximum number of fold in joint survey increases from 88 to 125 fold.

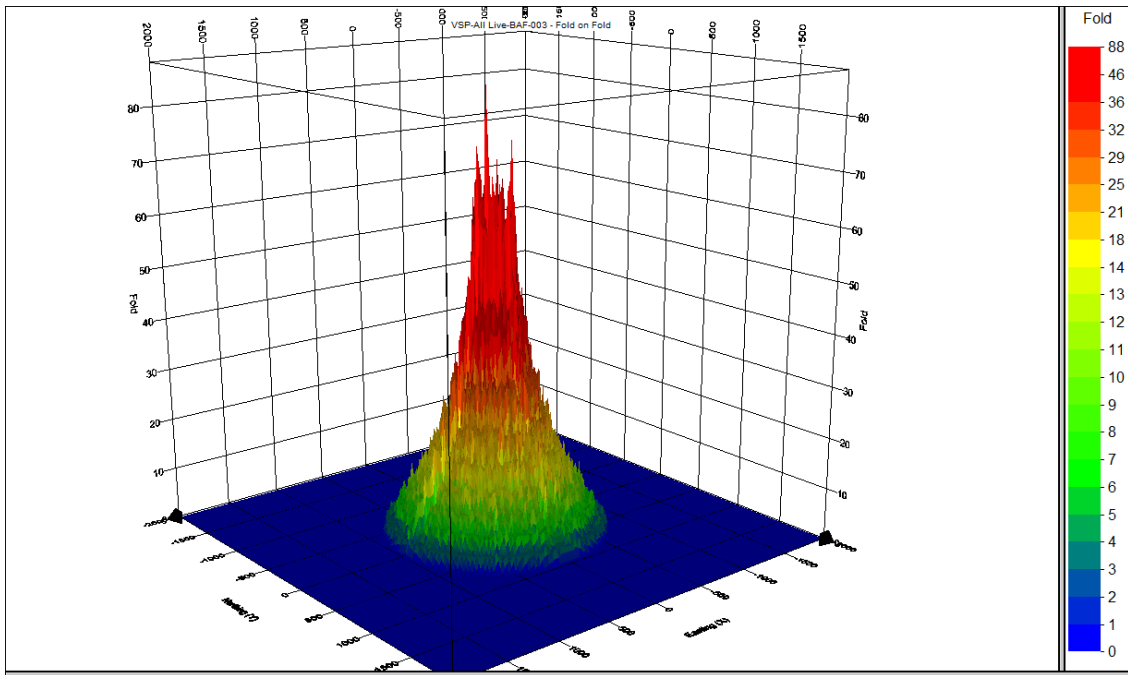
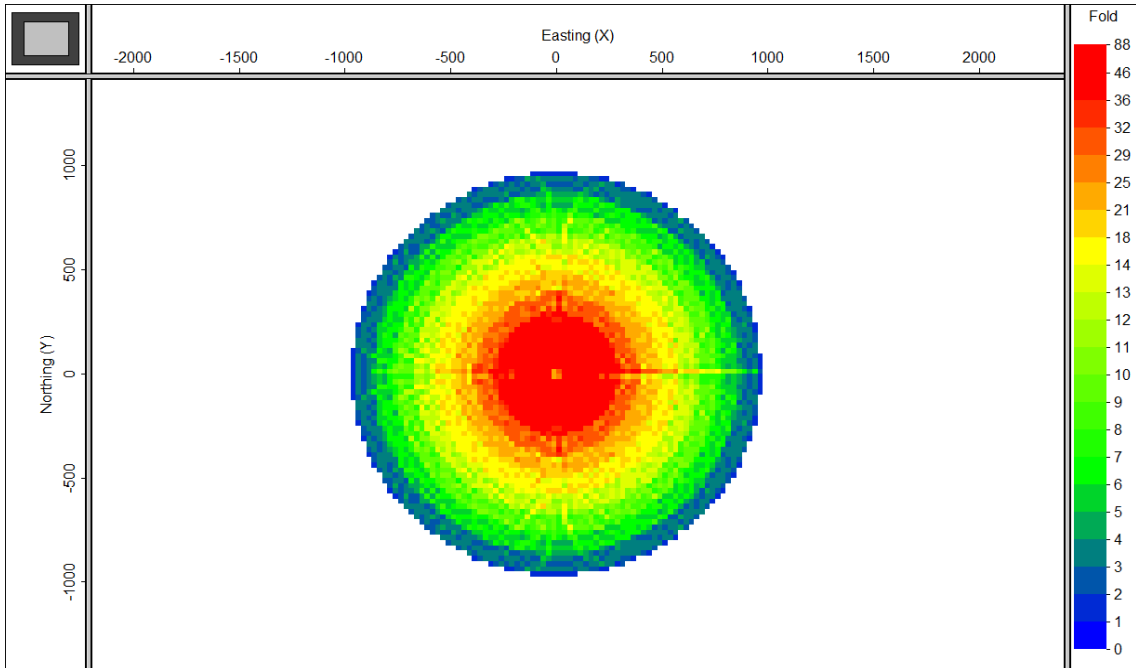


Figure 2.20: Fold coverage for VSP survey itself in plane view on top and 3D view on bottom.

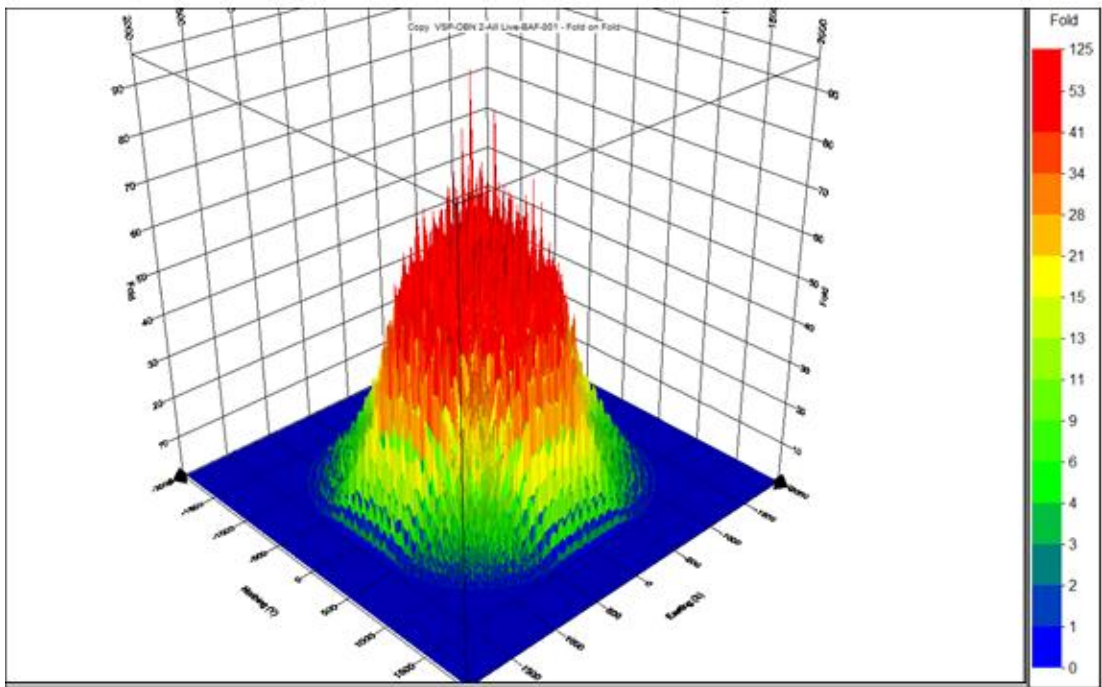
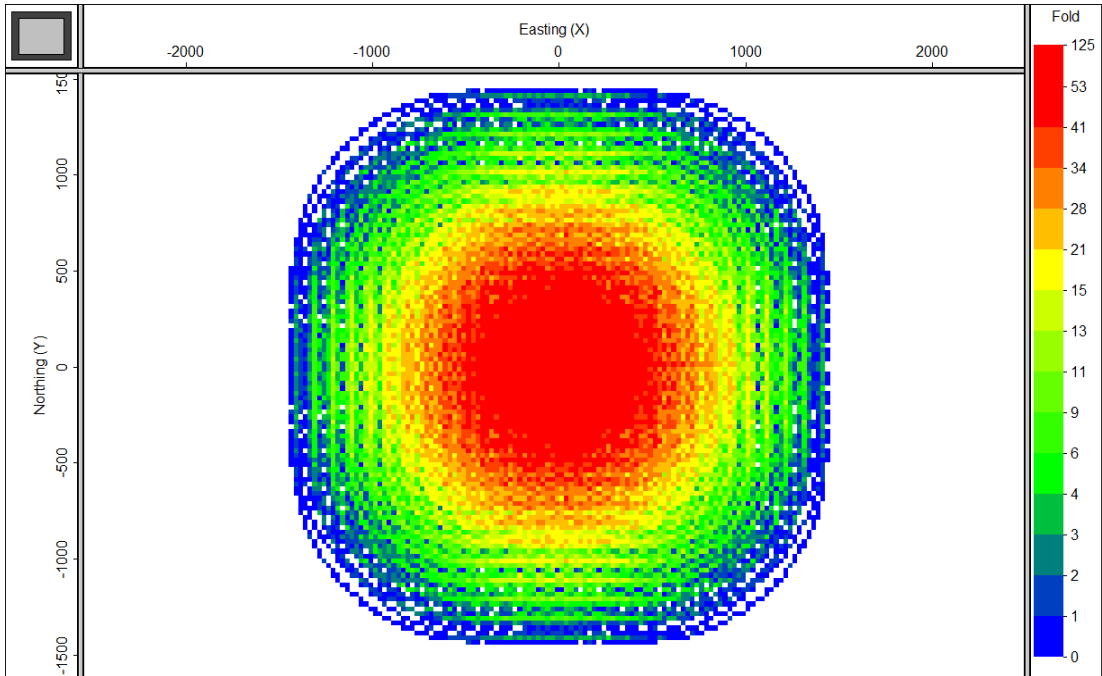


Figure 2.21: Fold coverage for joint OBN-VSP survey in plane view on top and 3D view on bottom.

Joint OBN-VSP survey has improvement in azimuth and offset distribution also.

Figure 2.21 shows the comparison of azimuthal coverage in spider diagram for both VSP itself and joint OBN-VSP survey. It is clear that joint survey design has better azimuthal coverage than VSP survey itself. VSP survey has limited azimuthal coverage in the direction of borehole; however, VSP survey with ocean-bottom nodes has full azimuth coverage.

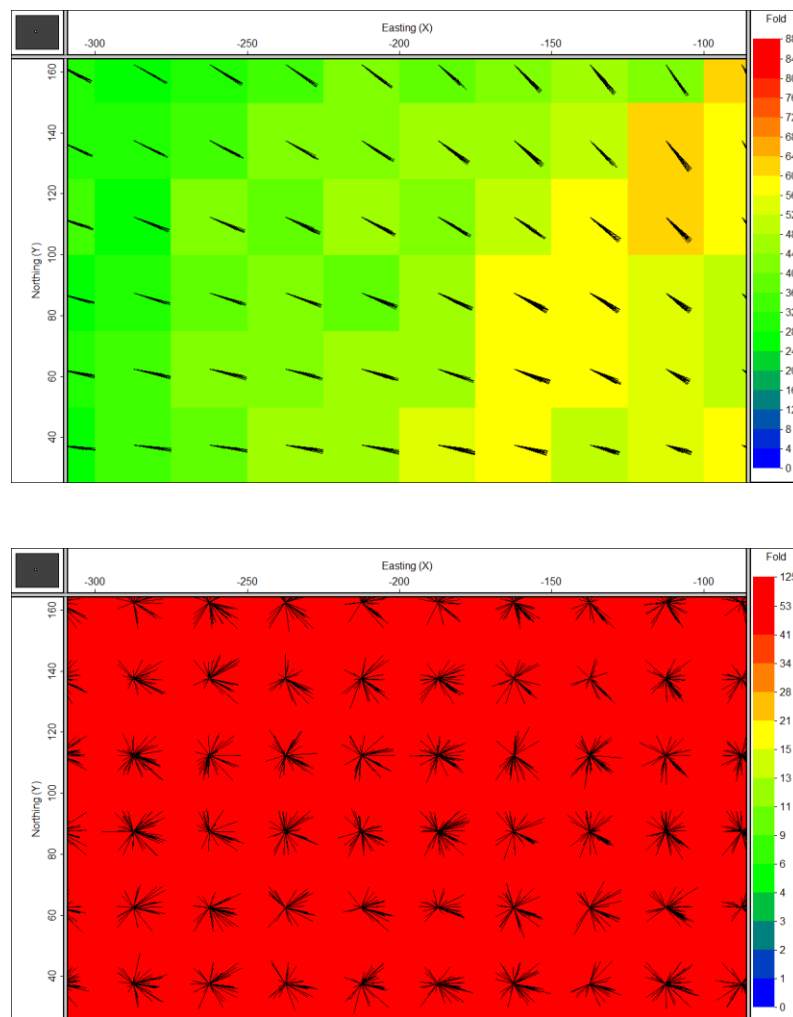


Figure 2.22: Comparison of azimuthal coverage for both surveys in selected area. Top shows azimuth distribution for VSP survey itself, bottom shows azimuth distribution for joint survey.

Offset distribution for both surveys can be seen in Figure 2.22. It is noticeable that joint survey design has better offset coverage than VSP survey itself. The limitations with VSP seismic such as poor azimuth and offset coverage were overcome by combining ocean-bottom nodes with VSP survey. Deploying nodes on the seafloor might be time and cost consuming; however, it can provide better data to image complex structures and some advantages such as a better azimuthal, fold, and offset coverage.

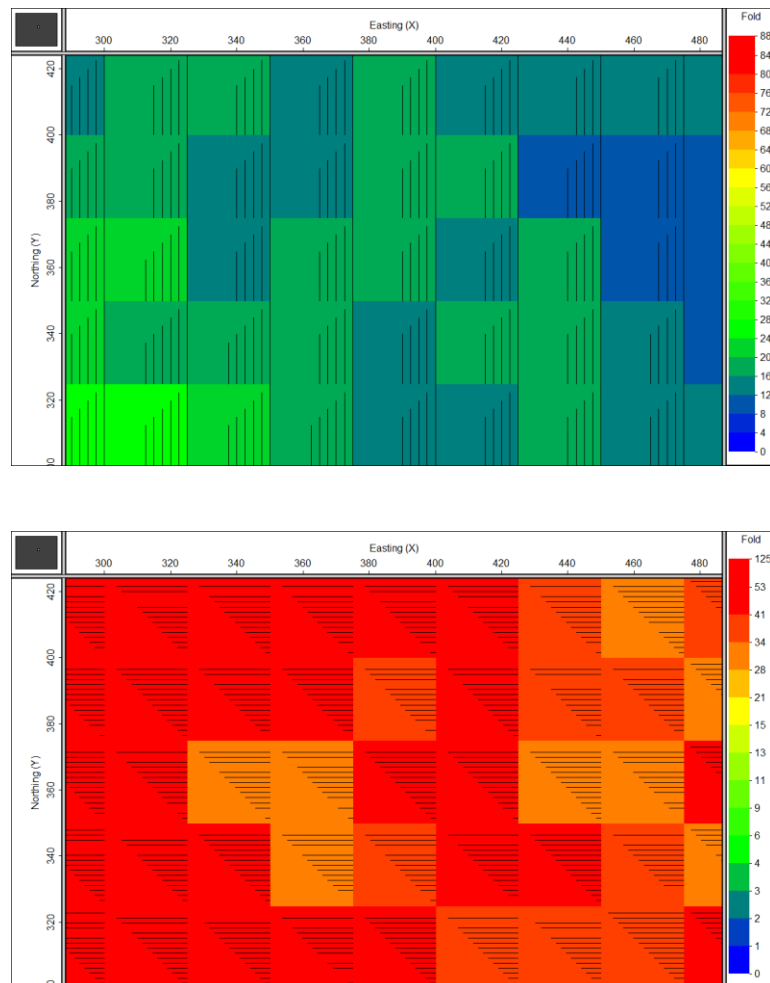


Figure 2.23: Comparison of offset coverage for both surveys in selected area. Top shows offset distribution for VSP survey itself; bottom shows offset distribution for joint survey.

Chapter 3

ATLANTIS SEABIRD SEATRIAL 3D-4C OBN SURVEY

3.1. Atlantis Field and Deepwater Imaging Challenges

The Atlantis field, discovered in 1998, is located approximately 190 miles south of New Orleans in the Gulf of Mexico in the southern Green Canyon protraction area (Howie, 2008) (Figure 3.1).

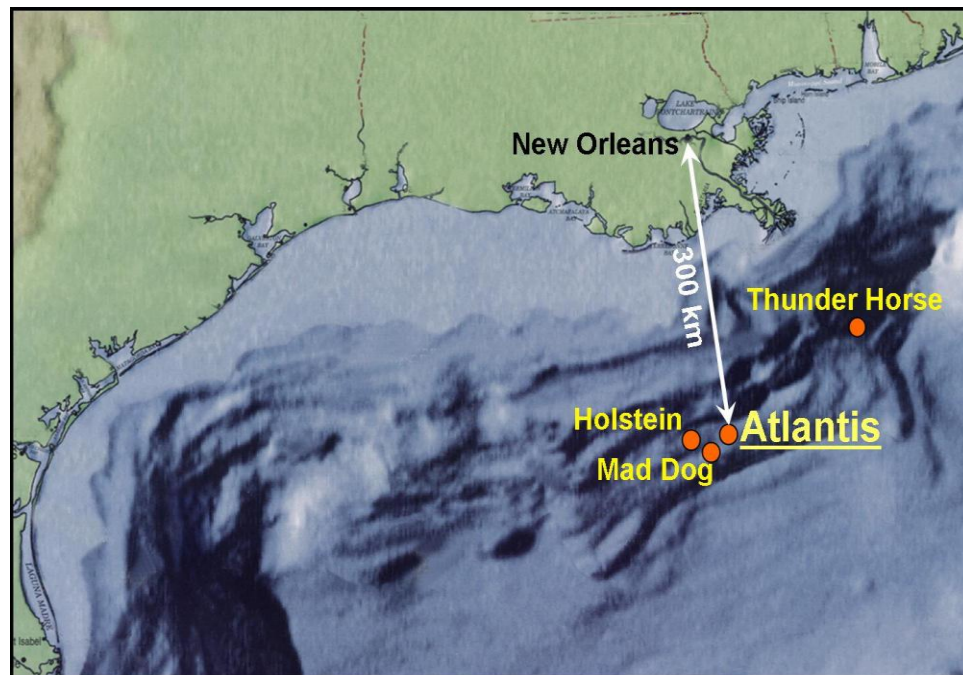


Figure 3.1: Location map of Atlantis field, Gulf of Mexico (Howie et al., 2008).

According to Howie et al. (2008), Atlantis is giant oil field. The field is expected to produce about 200,000 barrels per day of oil and 180 million cubic feet per day of gas.

The Atlantis field has several fundamental challenges to image the subsalt portions of the field. One of the main challenges is that northern portions of the structure locate under a complex allochthonous (meaning “out of place”, as opposed to “autochthonous” = “in place”) salt body. Another challenge is that the part of complex salt body, called autochthonous salt, approaches the sea floor (Figure 3.2). Another challenge is that the part of complex salt body approaches the sea floor. This causes a major bathymetric feature on the sea floor which is known as Sigsbee Escarpment. Depth of Sigsbee Escarpment changes from 1300 m to 2400 m with slopes up to 30 degrees (Figure 3.3).

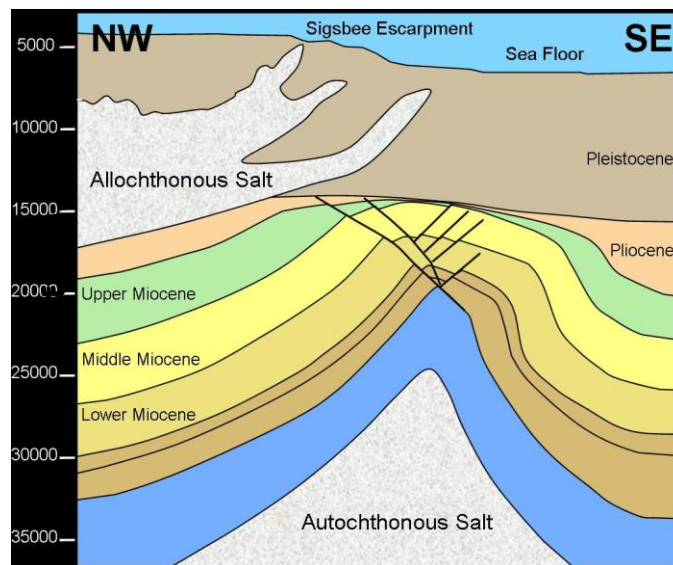


Figure 3.2: Geological cross section over the Atlantis field. (Howie et al., 2008)

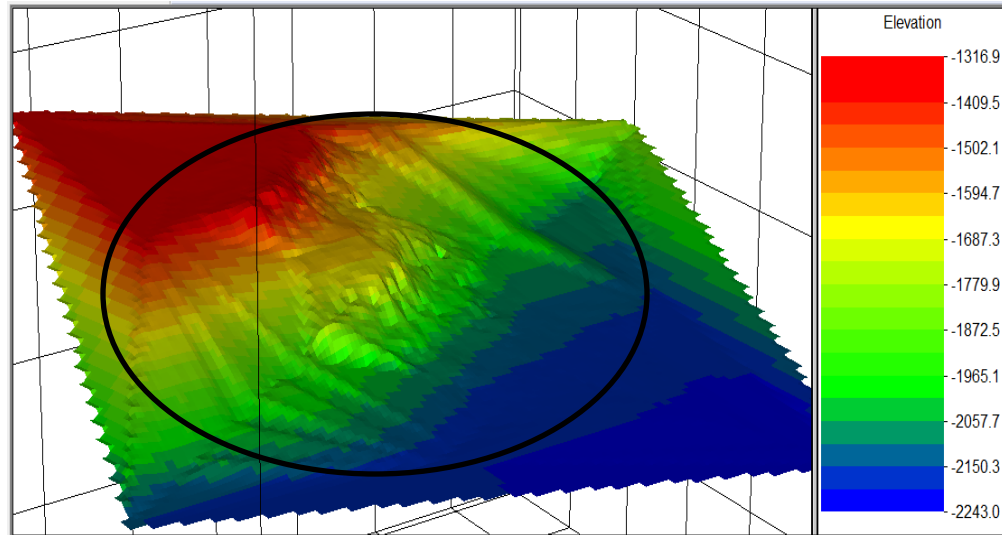


Figure 3.3: 3D view of Sigsbee Escarpment. Sigsbee bathymetry was displayed on OMNI 3D. The black circle indicates the area of Atlantis field.

Conventional narrow azimuth streamer acquisition is inadequate in imaging over Atlantis structures because of the complex sea floor and complex overburden. An OBN survey seems well suited for Atlantis field due to complex seafloor, subsalt imaging challenges and water too deep for cables. These imaging challenges at Atlantis field motivated BP for using ocean-bottom nodes at this location. BP deployed over 900 autonomous nodes on the sea floor in water depth ranging from 1300 to 2400 m at Atlantis field in late 2005 to early 2006 (Beaudoin, 2006).

3.2. Atlantis Seatrial 3D-4C OBN Survey

Another ocean-bottom survey, Atlantis Seatrial 4C ocean-bottom node (OBN) survey, was acquired by SeaBird Exploration in 2009 over the Atlantis field at Gulf of Mexico. It was a trial OBN survey with 41 nodes at 17 locations on receiver line to record the data from sea bottom. There are 14058 shot points in total, 4 crosslines (three short and one long), one long inline and dense shot carpets (26.85m x 46.5m). Figure 3.4 shows the receiver and shot locations of Seatrial survey.

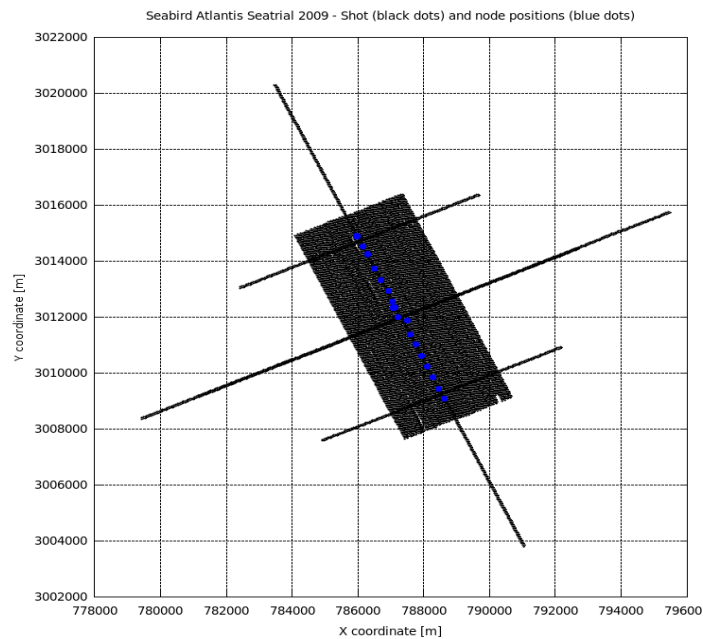


Figure 3.4: Atlantis Seatrial survey. Shot (black dots) and node positions (blue dot)

I used the same receiver and shot locations with the Seatrial OBN survey to create a new survey in OMNI 3D to see illumination, fold, azimuth, and offset

distributions. The same water depths, ranging from 1300 to 2400 meters, were used to specify the target depth and receiver attributes. Figure 3.5 shows the illumination on the sea floor. The black dots indicated the receiver location on the sea floor and the red dots indicates source location on the sea surface.

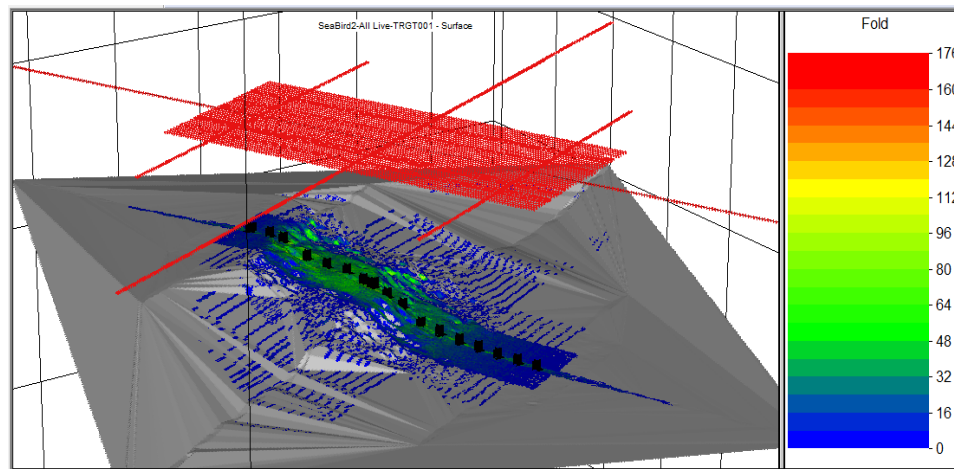
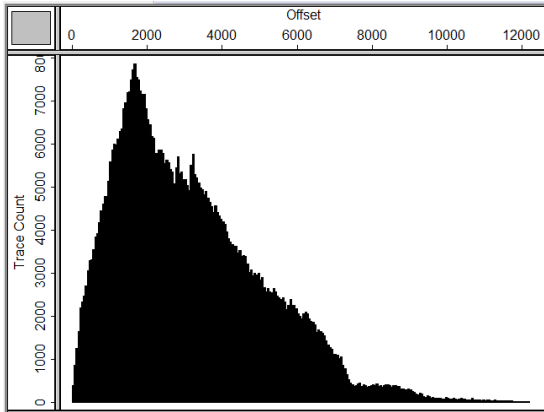
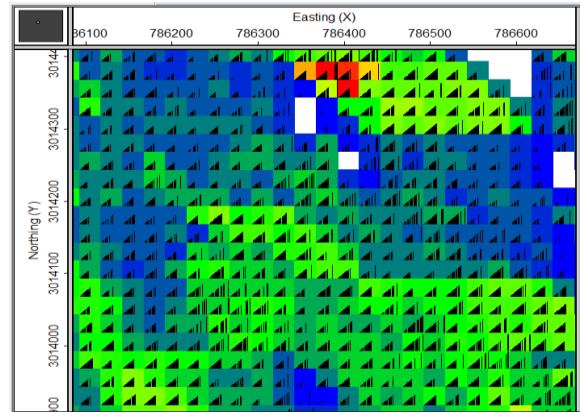


Figure 3.5: Illumination of Seatrial OBN survey on the sea floor. The black dots indicates node locations, red dots indicate source locations. The grey surface indicates ocean-bottom with elevation range from -2400 m to -1300 m.

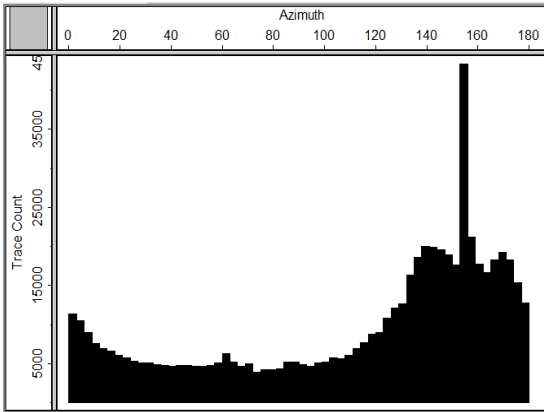
Maximum fold is located on the long inline over the receiver line. Average fold distribution on the sea floor is 96 fold (green area) which can be seen in the Figure 3.5. Azimuth and offset distribution results for Seatrial survey are shown in Figure 3.6.



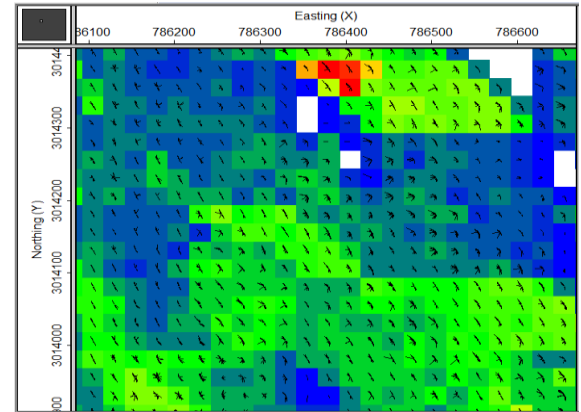
(a)



(b)



(c)



(d)

Figure 3.6: Azimuth and Offset distribution of Seatrial OBN survey. (a) Offset distribution-trace count. (b) offset distribution – stick diagram. (c) Azimuth distribution-trace count. (d) azimuth distribution – spider diagram.

The Seatrial OBN dataset was used to process and image the ocean-bottom data from Atlantis field. Figure 3.7 indicates a raw receiver gathers for radial, transverse, vertical and hydrophone components from Seatrial OBN data set. As a raw data analysis, direct arrivals, first water bottom multiples, PS-converted waves, and P-wave reflections

can be seen from Figure 3.6. All processing and imaging steps will be described in the next chapter.

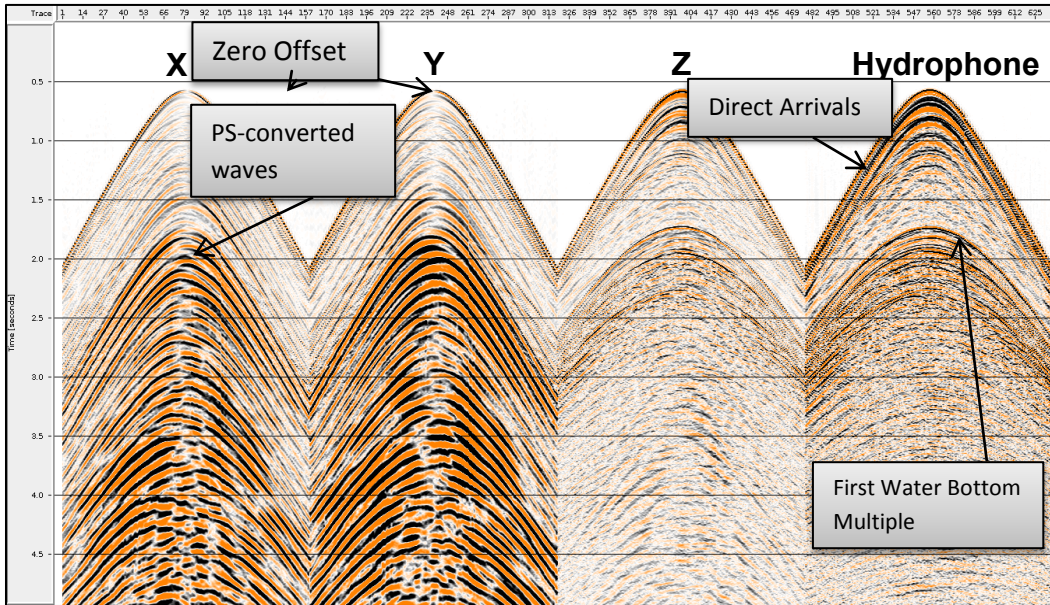


Figure 3.7: Raw receiver gathers from Seatrial OBN dataset. From left to right: X , Y, Z (vertical) and P (pressure) components.

3.3. Atlantis Field Synthetic Data

As mentioned earlier, narrow-azimuth conventional streamer data imaging has some limitations in complex areas such as subsalt in the deepwater Gulf of Mexico. These limitations can be enhanced by using ocean-bottom nodes on the sea floor to acquire wide-azimuth data (Shoshitaishvili, 2006).

To demonstrate that OBN acquisition geometry with sparse receiver locations and dense shot locations can provide competence image quality, I created a synthetic

ocean-bottom seismic dataset using finite difference modeling of acoustic waves in Echos software. The Seatrial Atlantis OBN survey acquisition geometry was used to create synthetic data, dense source interval and sparse receiver interval. The synthetic data has 426 m receiver interval, ~50 m shot interval, and 2 ms sampling interval.

I extract the water bottom depths from real Seatrial OBN dataset, to create a synthetic model with the same depth of the sea floor as in real survey. The model consists of ocean-bottom and three flat reflectors (Figure 3.8).

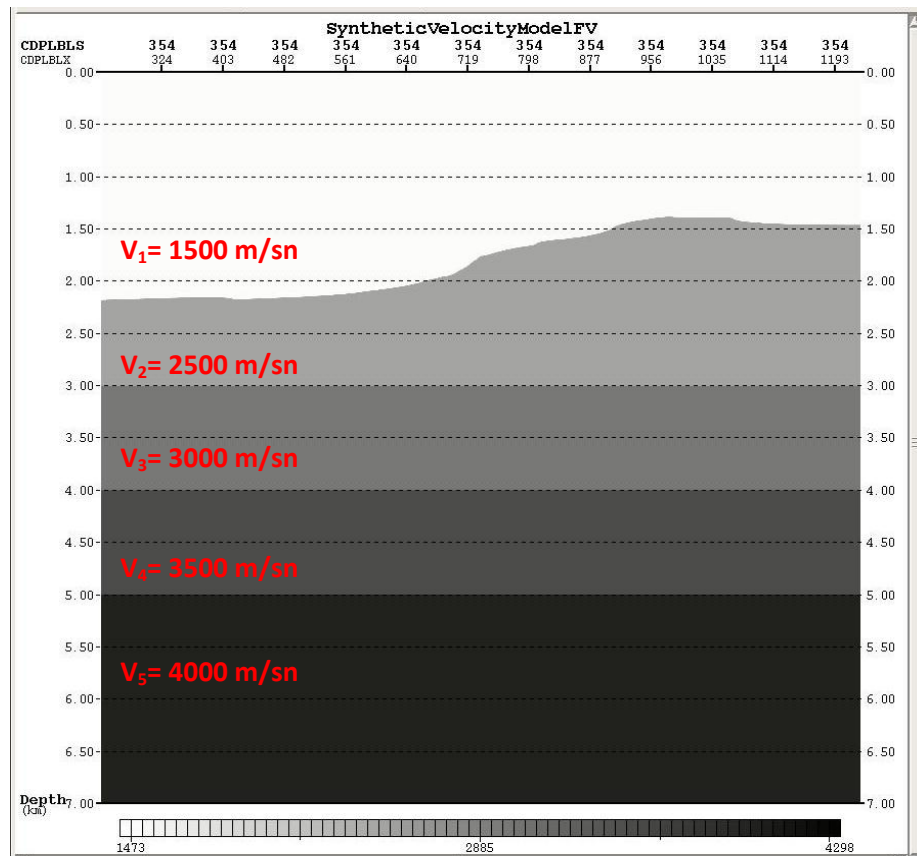


Figure 3.8: 2D section of synthetic velocity model.

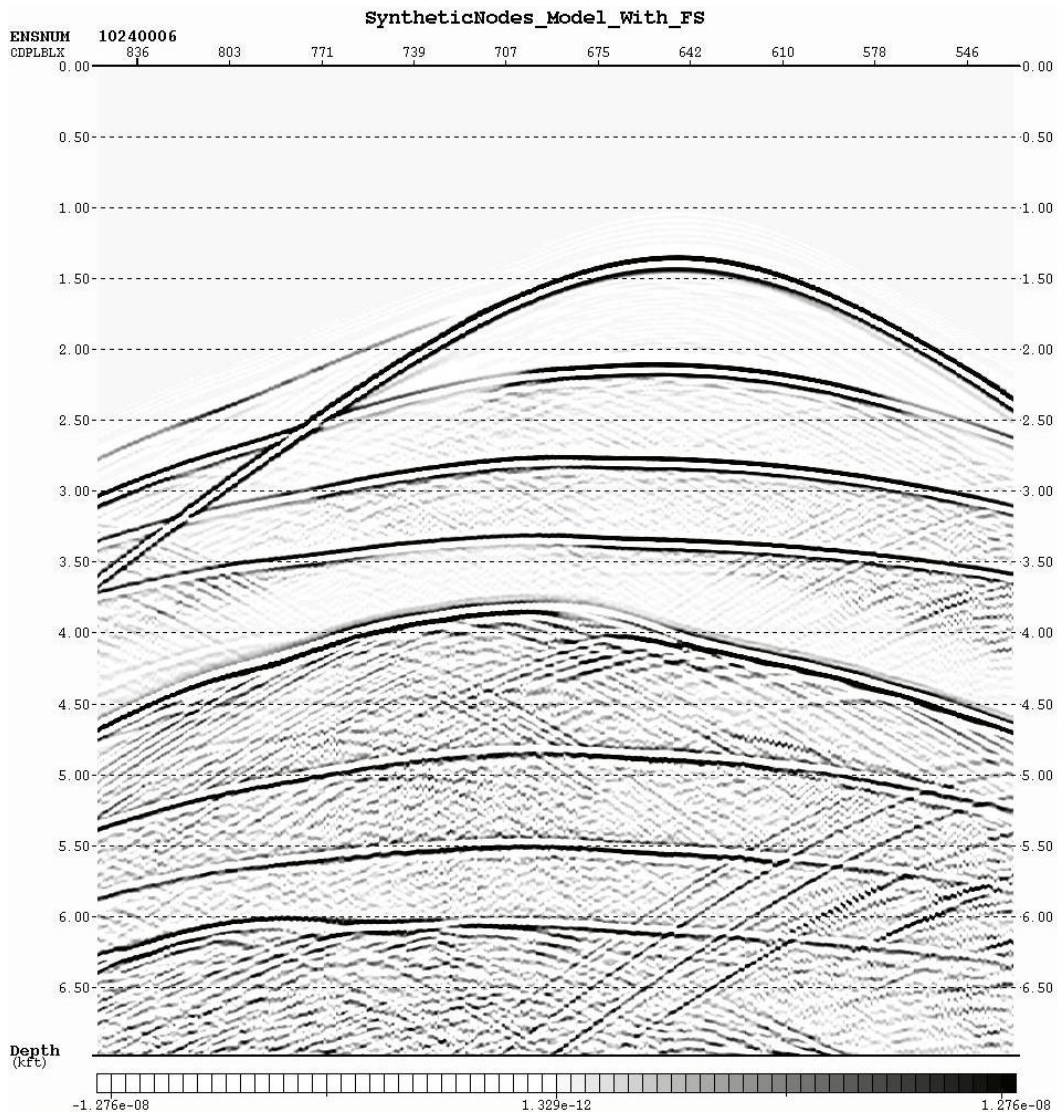


Figure 3.9: Atlantis field synthetic receiver gathers.

Synthetic data which were generated from Atlantis field, Gulf of Mexico are shown in Figure 3.9. Since synthetic data are generated with free surface, direct arrivals, reflections from flat layers, first water-bottom multiples, receiver, and source-side multiples can be seen in Figure 3.9.

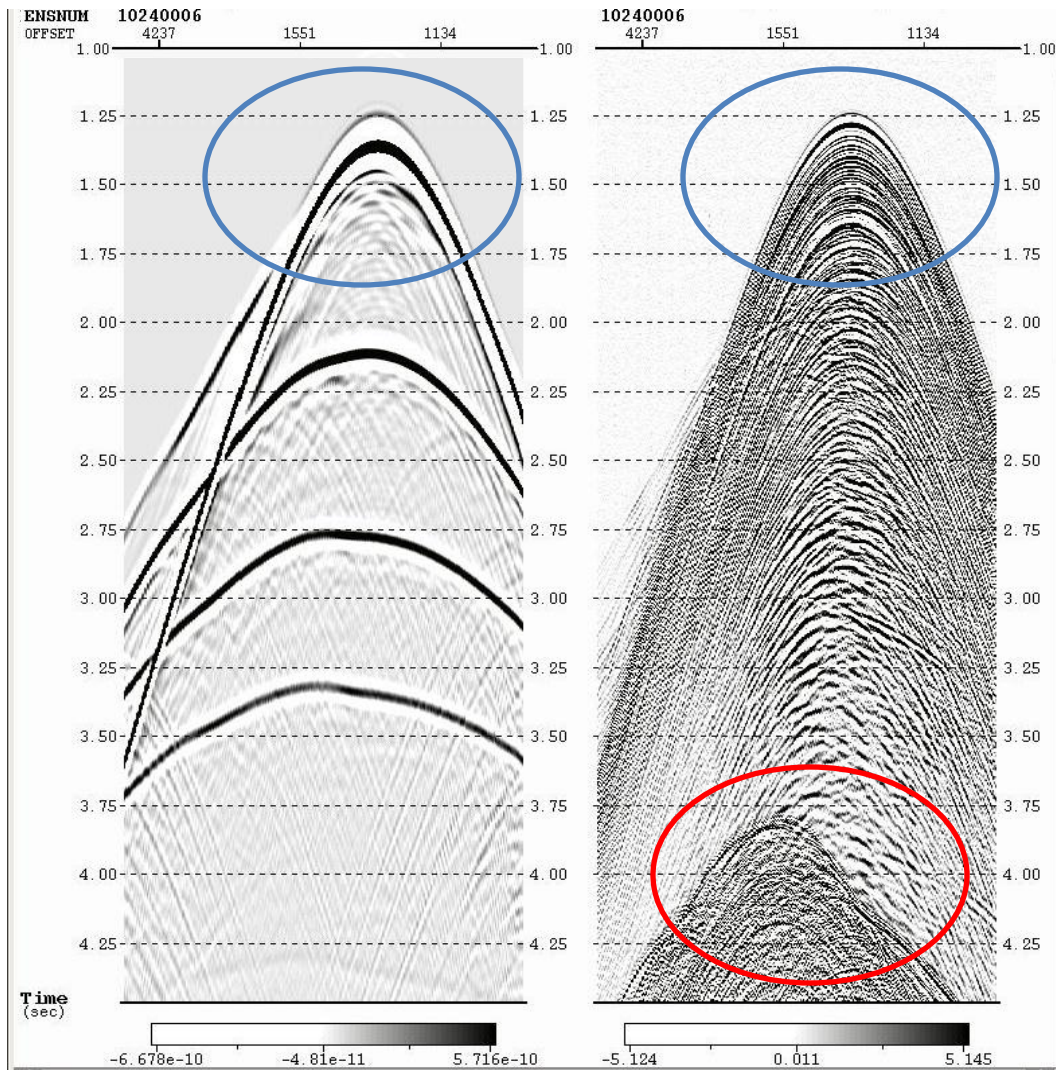


Figure 3.10: Synthetic up-going wavefield data and real Z component data from the Seatrial OBN survey.

Figure 3.10 shows the receiver gathers from both synthetic and Seatrial dataset for node number 1024 and shot line number 6. Since I used the same water bottom depth with Seatrial dataset, first arrivals, highlighted in blue circle, are the same for both dataset. There are no multiples, but only up-going primaries can be seen on the synthetic data because I created the data with no free surface. This is the reason that

first water bottom multiples, highlighted red in the Seatrial real data, cannot be seen in synthetic data. This refers that synthetic data generated with no free surface carries information from only primaries as up-going wavefield.

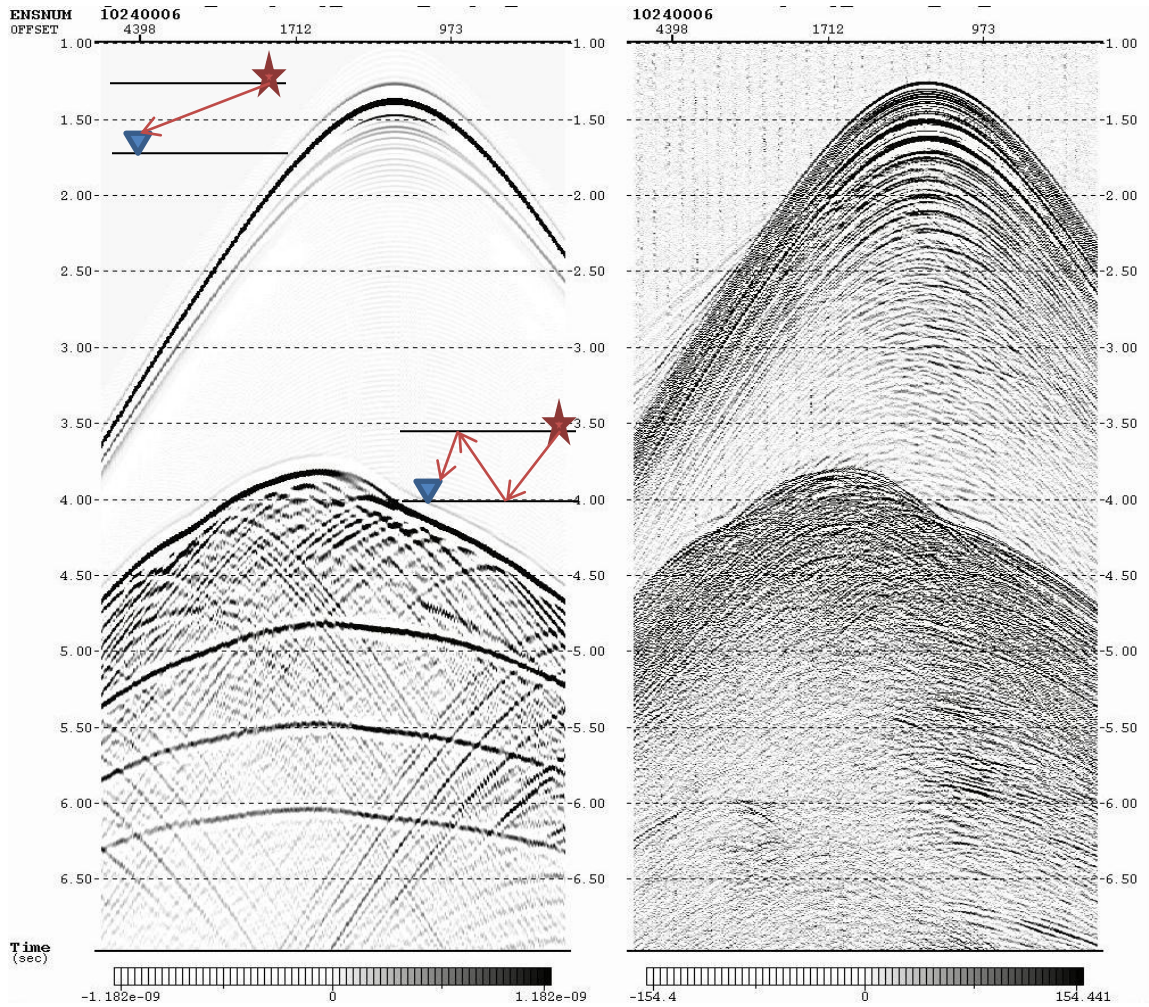


Figure 3.11: Synthetic down-going wavefield data and real down-going wavefield data from Seatrial OBN survey. In down-going synthetic data, direct arrivals and receiver-side ghost can be clearly seen.

To generate down-going synthetic data, I used the down-going wavefield from the Seatrial OBN real data. The wavefield separation of OBN data into up-going and down-going will be explained in the next chapter (chapter 4).

Figure 3.11 represents synthetic down-going wavefield on the left side and real down-going wavefield from Seatrial OBN dataset on the right side. It is clear that down-going wavefield carries information from multiples. Since I used the same water bottom topography with the real data to generate synthetic data, synthetic data has the same water bottom multiple with the real data. Multiples of the flat layers can be seen under first water bottom multiples. However there is no primary information from flat layers in the down-going wavefield data.

These down-going and up-going synthetic datasets will be used for imaging in the next chapter to understand mirror imaging method.

Chapter 4

OCEAN-BOTTOM NODE DATA PROCESSING AND IMAGING

4.1. Motivation

High-quality data from the sea floor can be acquired with ocean-bottom node acquisition techniques. As mentioned earlier, ocean-bottom node acquisition can provide wide-azimuth data set with sparse receiver interval and dense source interval. The ocean-bottom nodes are often deployed on and retrieved from the sea floor by remotely operated vehicles (ROVs). Running ROVs to position nodes on the sea floor is an expensive process. Thus, a sparse receiver interval is generally used to acquire the data on the sea floor because of the higher cost of operations (Alerini, 2009).

A main challenge with the ocean-bottom nodes is now processing and imaging of the data. Acquiring the data on the sea floor from deep water, with a large distance between nodes makes the conventional processing steps difficult to apply for OBN datasets. Another disadvantage of the OBN survey with sparse receiver intervals is that illumination at shallow subsurface is poor (Alerini, 2009).

According to Ronen et al. (2005), velocity model estimation of ocean-bottom node data is difficult since poor illumination makes the continuity of events in common-shot gathers, common-midpoint gathers, and common-image gathers difficult to determine.

To estimate the velocity model from Seabird OBN dataset, I tried different approaches in this study. First, many migration sections were obtained with different constant velocities (from 1400 m/s to 3000 m/s). I then compared these sections with each other to estimate best velocity model. Another approach to estimate the velocity model from updating velocities using common-image gathers.

Water-bottom reverberations are a well-known problem for marine acquisition. According to Dash et al. (2009), many researchers have worked on suppressing the water layer multiples. The assumption that multiples are noise is the main reason to suppress the water layer related multiples. However, the only difference between primaries and multiples is that multiples travel along different paths (Dash, 2009).

In this study, I used the water layer multiples (down-going wavefield) to improve the image quality and illumination at shallow subsurface. Imaging with the down-going wavefield is called the mirror imaging method. Kirchhoff pre-stack time migration, Kirchhoff pre-stack depth migration, and reverse time migration (RTM) adapted for OBN were used to image the datasets.

4.2. Wavefield Separation

Wavefield separation techniques have been developed by many researchers, e.g. Amundsen and Reitan (1995), Osen et al. (1999), and Schalkwijk et al. (1999). According to Dash et al., (2009), White (1965) was the first to recognize that the receiver side water layer multiples can be removed by combining the pressure and velocity phones.

Since pressure is a scalar quantity, which means it is independent of the up-going (U) or down-going direction (D), U and D pressure wavefields have the same polarity on the seafloor pressure recording (Dash, 2009).

Figure 4.1 shows the up-going and down-going recordings by hydrophone and geophone on the sea floor. Both hydrophone and geophone record same polarity below the sea floor; however they record opposite polarity above the sea floor (Barr et al., 1989; Dragoset et al., 1994; Ball, 1996; Barr et al., 1997; Bale, 1998).

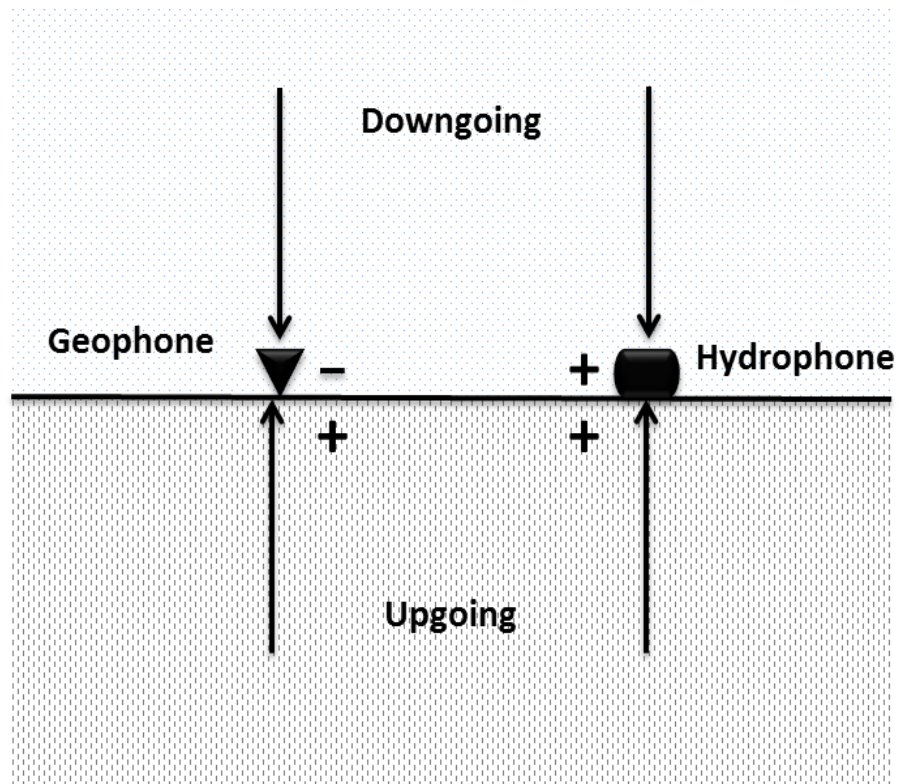


Figure 4.1: Schematic diagram of the hydrophone and geophone at the ocean-bottom as they record up and down-going wavefield.

Therefore, wavefield separation into up-going and down-going wavefield on the ocean-bottom can be obtained by combining of hydrophone and geophone (PZ summation) as:

$$U = \frac{(P + \rho cZ)}{2}$$

and (1)

$$D = \frac{(P - \rho cZ)}{2}$$

where:

U = the up-going wavefield,

D = the down-going wavefield,

P = pressure component,

Z = the vertical velocity component,

ρ = the density of water and

c = the acoustic velocity (Dash, 2009).

The water-column surface related multiples can be classified in two types: source-side and receiver-side multiples. Source-side multiples travel between ocean-bottom and the sea surface, then reflect from subsurface reflectors before recording.

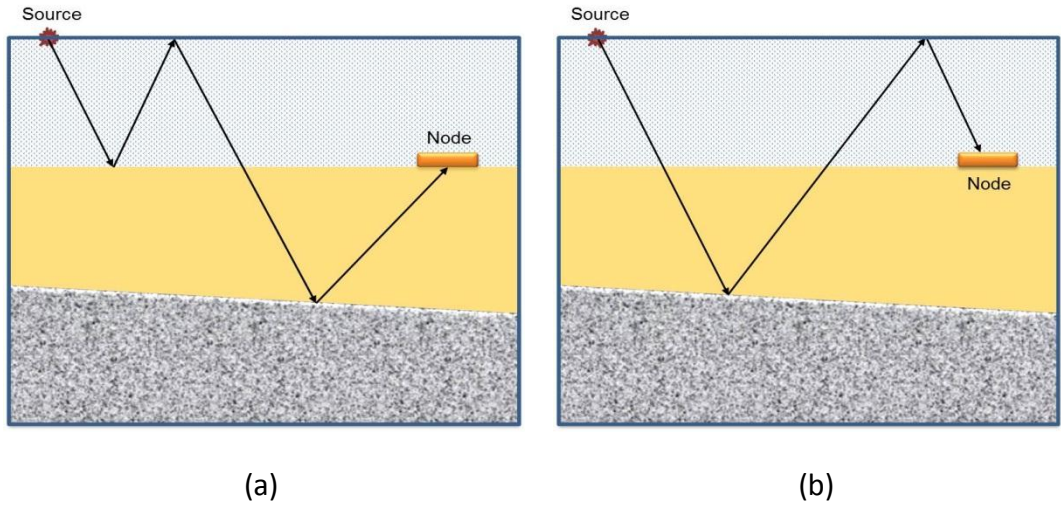


Figure 4.2: (a) Schematic demonstration of source-side and (b) receiver-side multiples on a 2D model (Modified from Xia, 2006).

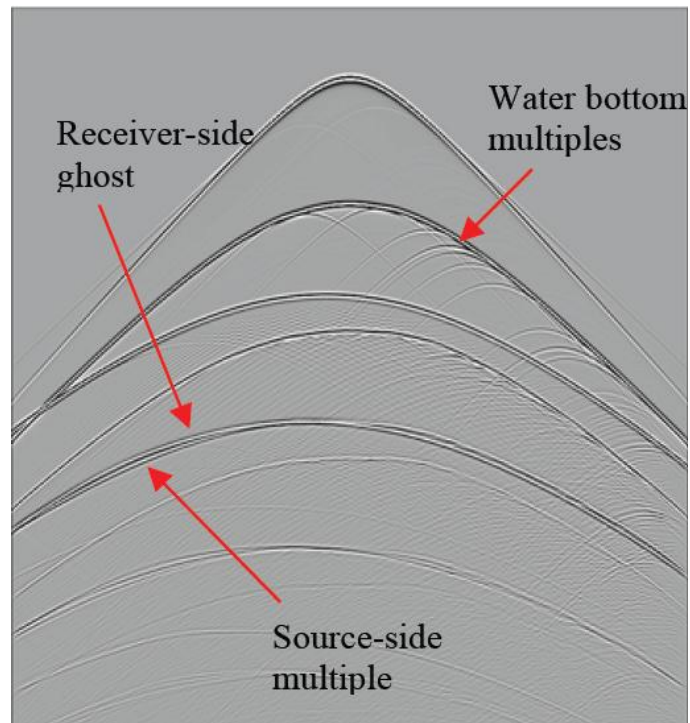


Figure 4.3: Demonstration of source-side and receiver-side multiples on a 2D synthetic example (Xia, 2006).

However, receiver-side multiples reflect from subsurface reflector first, then reflect from sea surface and record (Xia, 2006). Figure 4.2 shows the schematic view of source-side (a) and receiver-side (b) multiple and Figure 4.3 shows the source-side and receiver-side multiples in synthetic data.

According to Xia et al. (2006), the up-going field without receiver-side side ghost can be expressed as:

$$U = P + A * Z \quad (2)$$

where:

P = the pressure component of recorded OBN data,

Z = the vertical velocity component of the data and

A = the matching filter between pressure and vertical components.

U = the up-going wavefield without receiver-side multiples

In this study, instead of using matching filter between components, I designed and applied a wavelet shaping filter to the both pressure and vertical component before wavefield separation. After wavelet shaping, PZ summation (wavefield separation) was applied to the real OBN data set.

4.2.1. Application to Atlantis Seatrial OBN dataset

A. Wavelet Shaping

As mentioned earlier, the Seatrial OBN data was acquired from Atlantis field, Gulf of Mexico in 2009 by SeaBird Exploration for testing purposes. A total of 43 ocean-bottom nodes deployed on the sea floor in 16 locations with water depth ranging from 1400 to 2300 meters.

The raw data were processed in common-receiver gather domain. Figure 4.4 represents the raw vertical (Z) component in common-receiver gathers and Figure 4.4 represents the raw pressure (P) component in common-receiver gathers.

After all initial pre-processing steps were done (noise attenuation, despiking), I designed a wavelet-shaping filter. A shaping filter to transform the estimated wavelet into the specified wavelet is computed by Least Squared method. The filter is then applied to the all traces of both pressure and vertical components.

In this study, I used zero-phase butterworth wavelet as a desired wavelet. The following equation was used to calculate a Butterworth wavelet:

$$A(f)^2 = \frac{\left(\frac{f}{f_a}\right)^{2N}}{\left(1 + \left(\frac{f}{f_a}\right)^{2N}\right)\left(1 + \left(\frac{f}{f_b}\right)^{2M}\right)} \quad (3)$$

where:

f_a = the low cutoff frequency,

f_b = the high cutoff frequency,

$N = SL/6$, [SL is the slope on the low-cut side (dB/Octave)],

$M = SH/6$, [SH is the slope on the high-cut side (dB/Octave)].

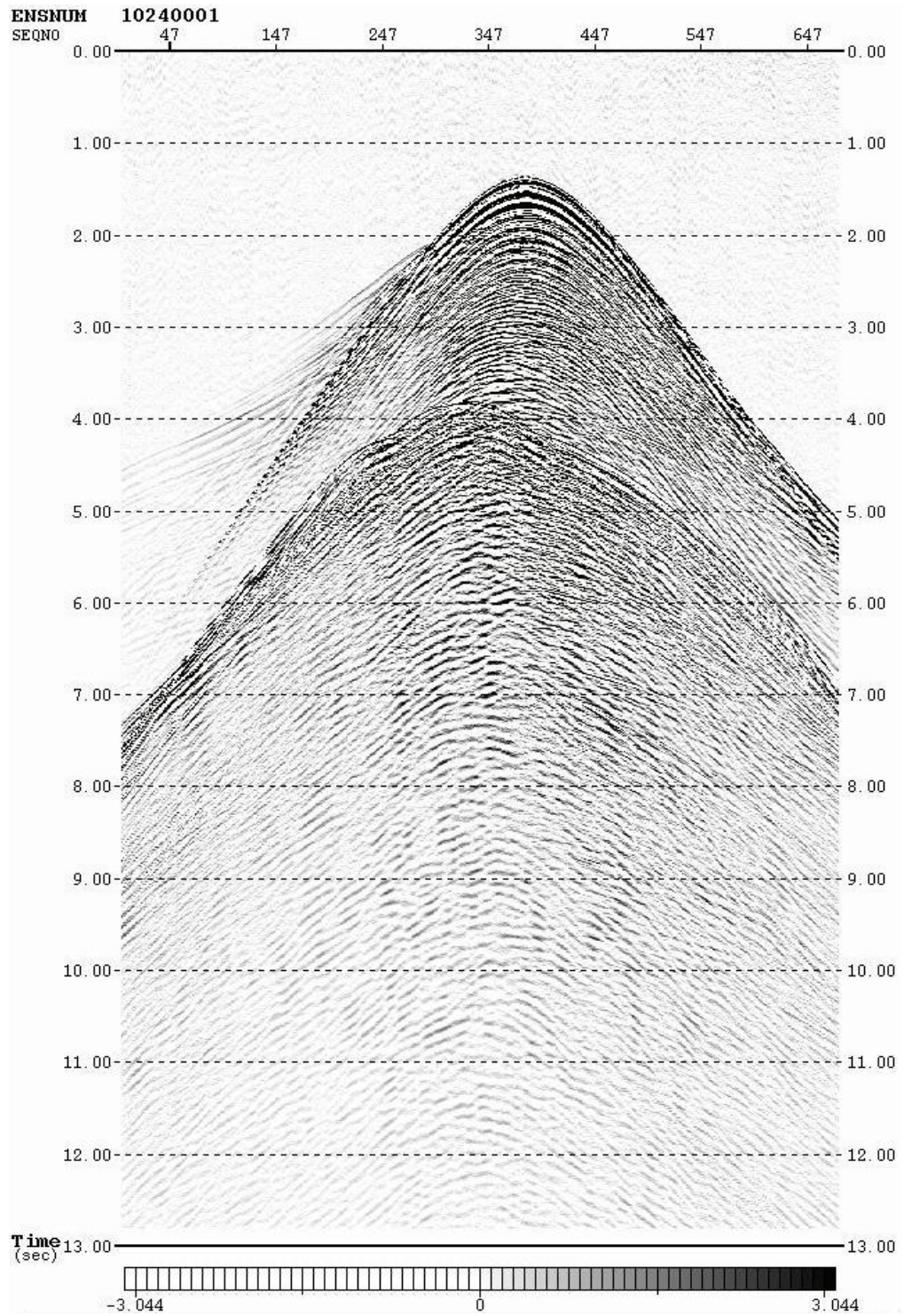


Figure 4.4: The raw vertical component (Z) common-receiver gathers of Seatrial OBN data from selected shot line.

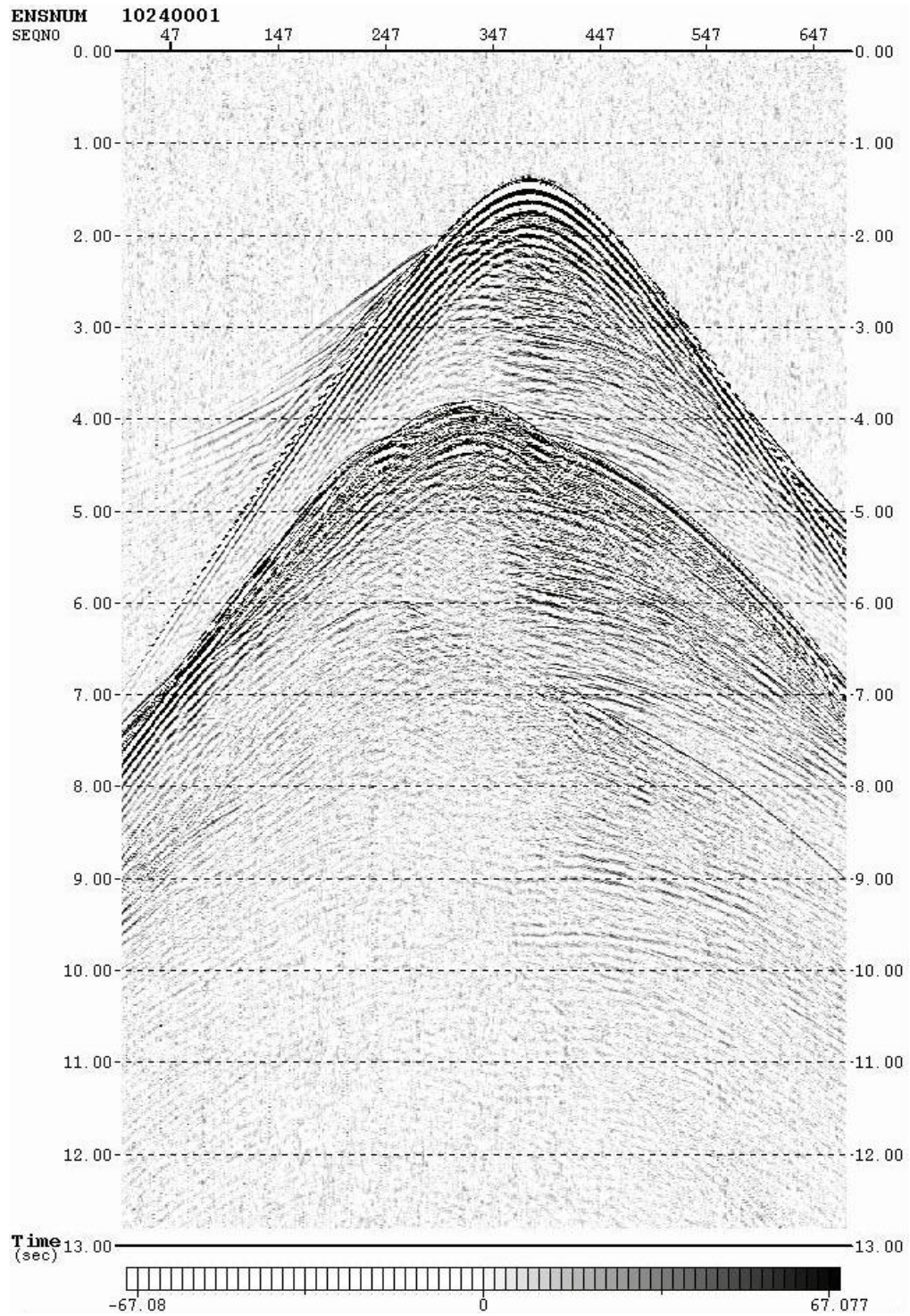


Figure 4.5: The raw pressure component (P) common-receiver gathers of Seatrial OBN data from selected shot line.

Figure 4.6 represents the Butterworth wavelet and Butterworth scaling functions with the time range of -8, 8 ms. The desired and generated Butterworth wavelet which was applied to both pressure and vertical components is shown in Figure 4.7.

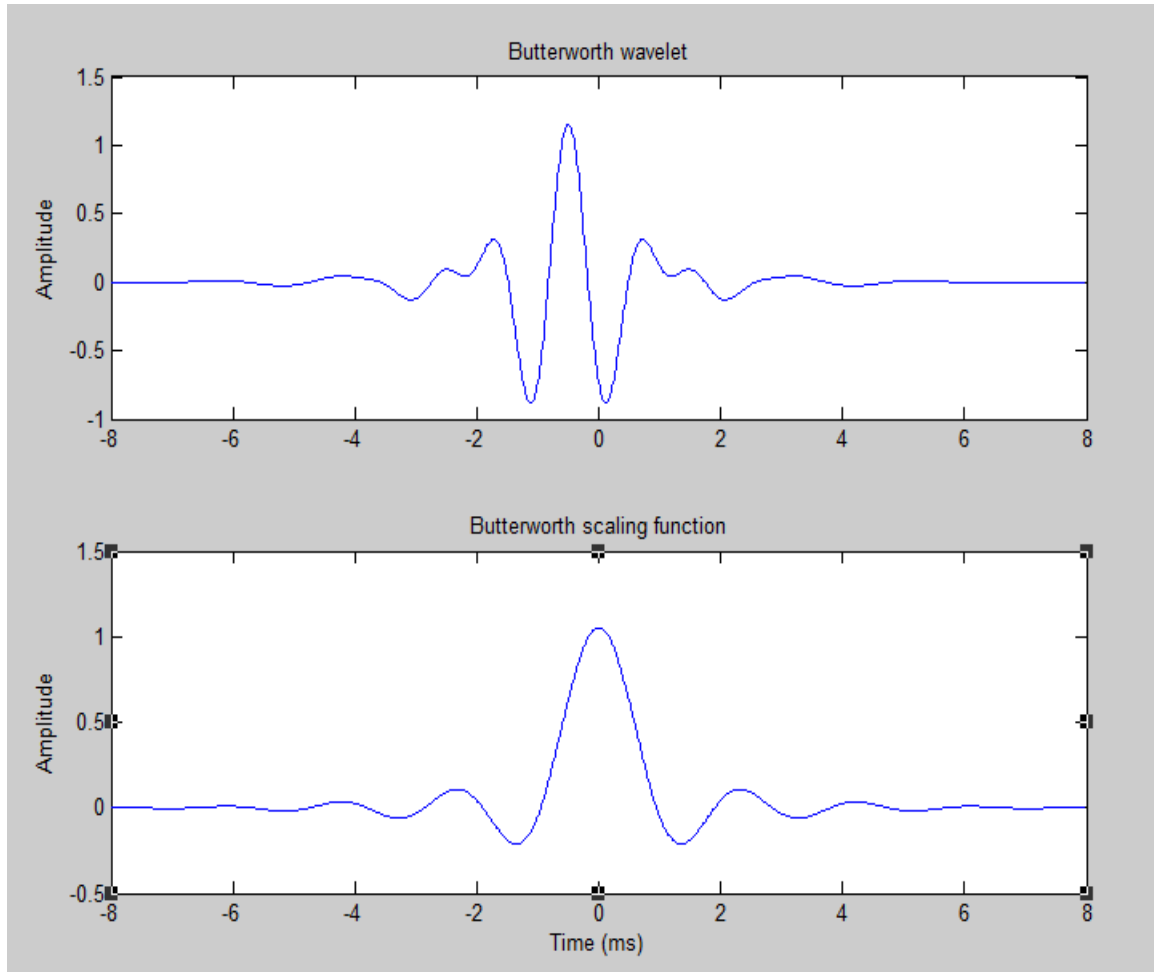


Figure 4.6: Butterworth wavelet and Butterworth scaling function. This figure was created in MATLAB.

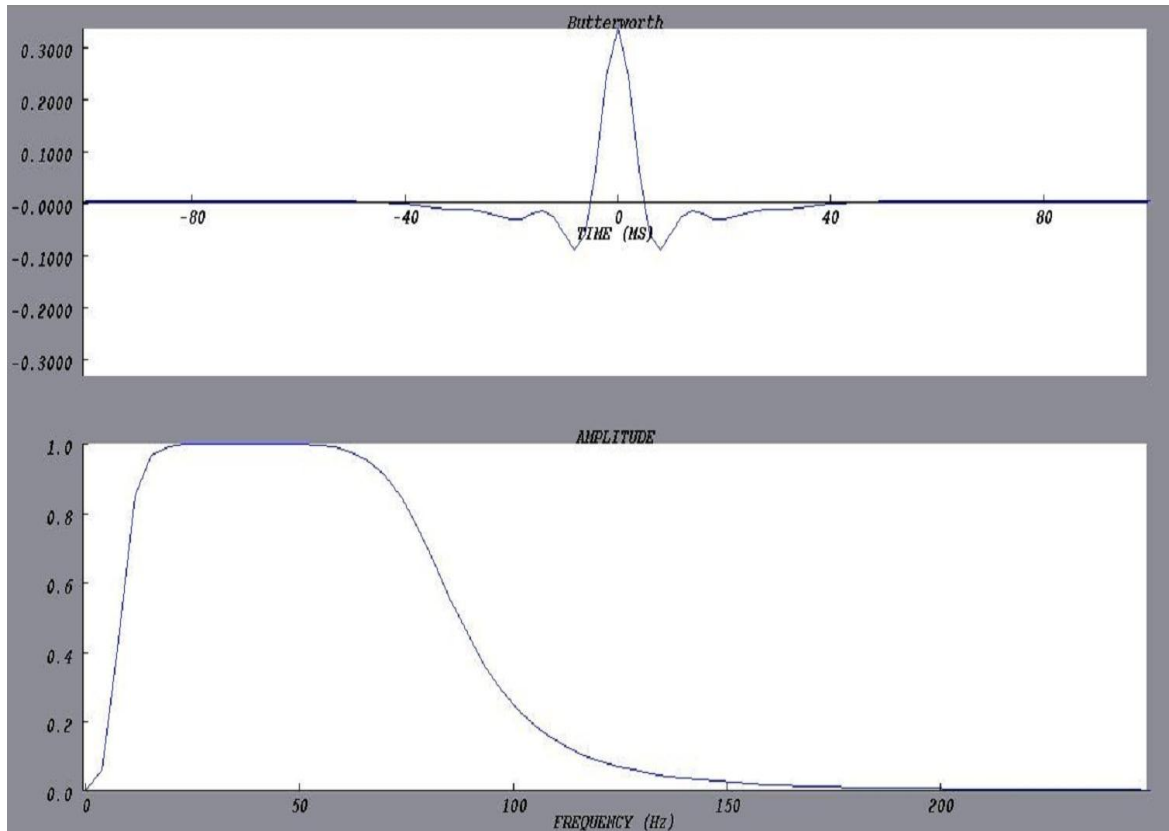


Figure 4.7: Desired and generated Butterworth wavelet. Low-cut frequency is 10 Hz, high-cut frequency is 80 Hz. Slope in the low-cut side is 18, and in the high-cut side is 36.

The purpose of applying wavelet shape filter is that make the P and Z components have wavelet shape as similar as desired wavelet shape. The desired wavelet, which is shown in Figure 4.7, was applied to Seabird OBN dataset before PZ summation. Results after wavelet shaping are represented in Figure 4.8. The Figure shows that after applying wavelet shape filter, both P and Z component have the same wavelet.

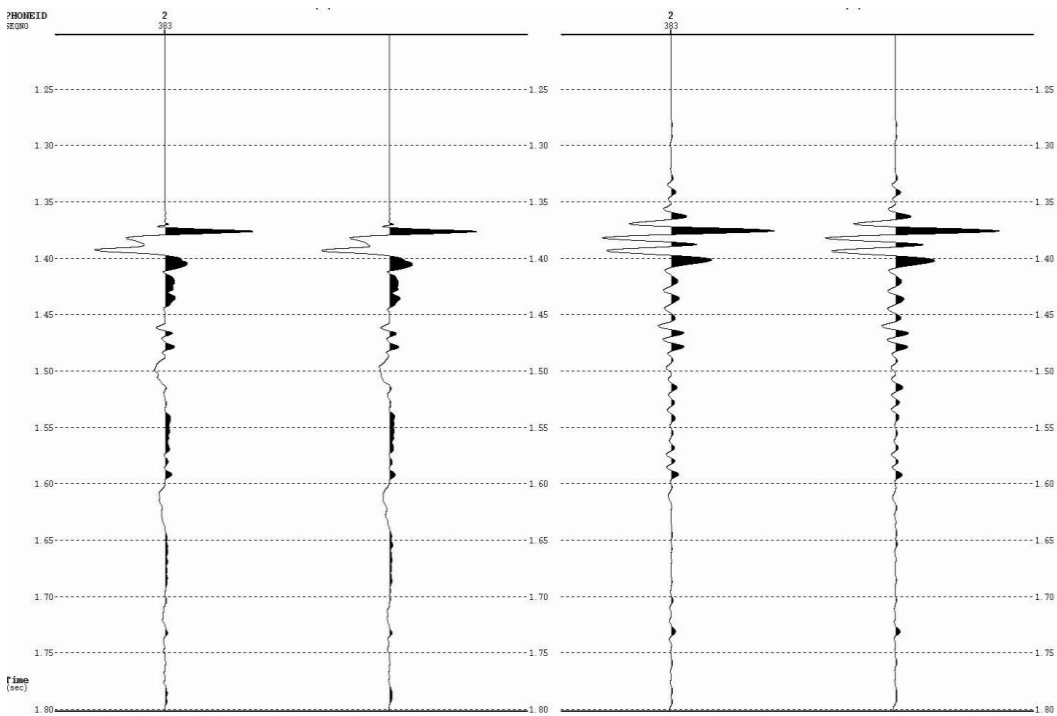
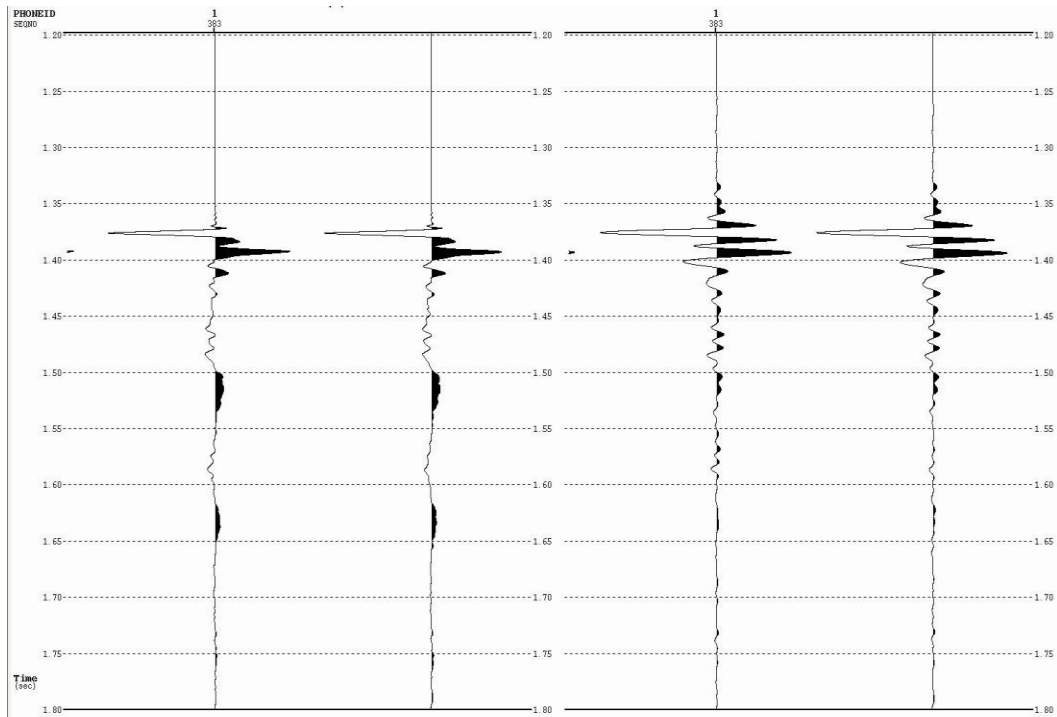


Figure 4.8: Results of wavelet shaping. The figure on the top shows the raw P component and after wavelet shaping, bottom shows raw Z component and after wavelet shaping.

It can be clearly seen from Figure 4.9 that direct arrivals on P and Z components have opposite polarity, annotated in red circles. However, they have similar polarity on primaries, annotated in blue circles. Both P and Z component have same wavelet shape with different amplitudes. Amplitude differences between components were scaled before PZ summation.

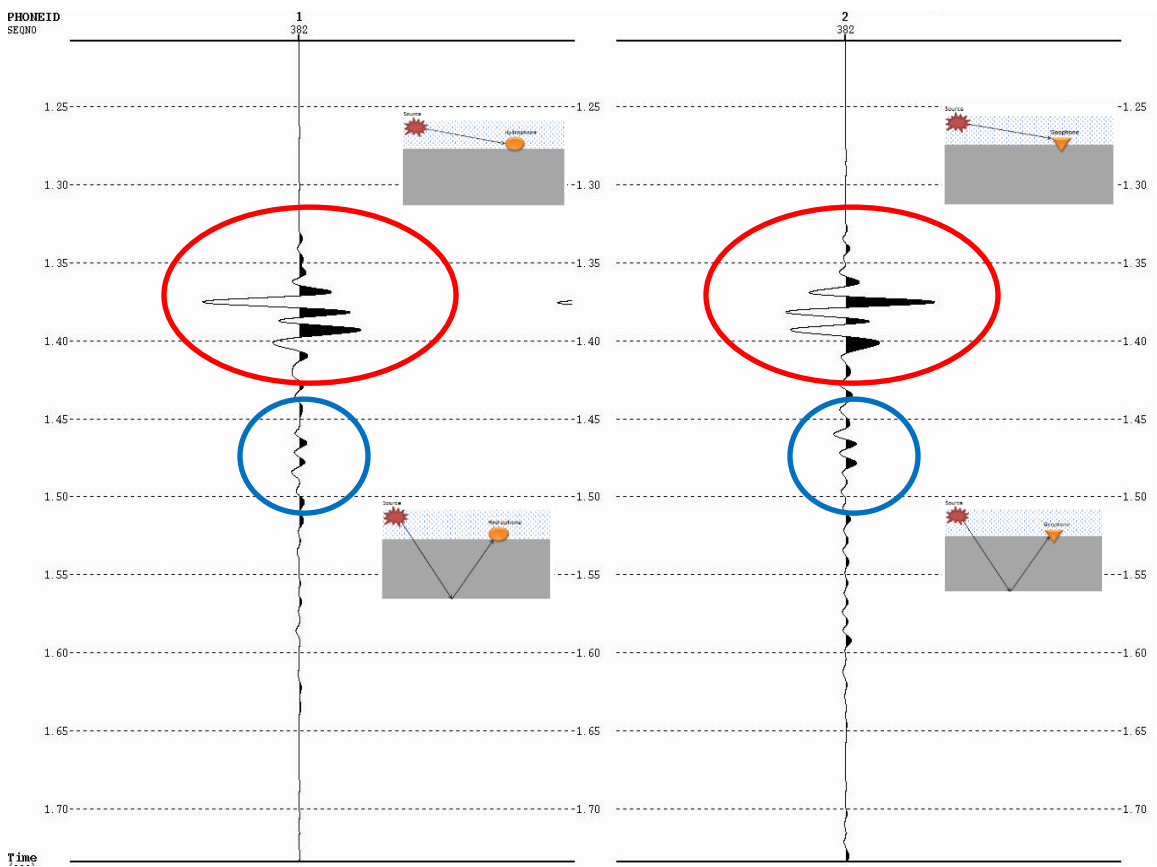


Figure 4.9: P and Z components and after wavelet shaping. Left side shows hydrophone data, right side shows geophone data. Red circles indicate the direct arrivals. Blue circles indicate primaries. Down-going wavefield (direct arrivals) has different polarity on hydrophone and geophone data.

B. Deghosting and PZ summation technique

According to Barr (1997), to obtain a clear image from subsurface, each reflection should appear as a single, short-duration wavelet on each trace. However, energy bouncing in the water layer above the ocean-bottom node sensors complicates the image quality. After a single reflection wavelet arrives and is recorded at the ocean-bottom from below, then continues traveling up to the water's surface and is reflected from the water's surface. When a new reflection arrives to the ocean-bottom, it is recorded again. This keeps reflecting from the water's surface and recording on the ocean-bottom. The undesired second and subsequent recordings of the reflection are the water-column reverberations.

If the reverberation energy is not removed from the data, each single reflection is represented by several wavelets (Barr, 1997). Hoffe et al. (2000) mentioned that dual sensors can be used for multiple suppressions. According to them, the combined hydrophone component (P) and vertical geophone (Z) component allows us to suppress receiver-side multiples.

The receiver-side multiples can be removed by adding pressure wavefield with scaled vertical velocity wavefield (PZ sum data), however source-side multiples still remain in the data (Hoffe et al., 2000). The multiples that remain after PZ summation can be removed by traditional multiple attenuation techniques such as SRME (Surface Related Multiples Elimination).

In this study, the wavefield separation technique (PZ summation) was applied to Seabird Atlantis 4C OBN dataset to obtain up-going and down-going wavefield. The difference of P and Z components provides down-going wavefield (PZ difference data), while summation of these two components provides up-going wavefield (PZ sum data) (Clarke, 2007). The raw P and Z component of the data set is shown in Figure 4.10. The blue circles in the figure shows the first water bottom multiples on the raw P and Z components, and the red circles indicate the multiples.

The results after applying the PZ summation and difference to the real OBN data are shown in Figure 4.11. The right side of the figure shows the up-going data (PZ summation) for a shot line of a receiver gather, and left side shows the down-going data (PZ difference). It can be clearly seen that the second water bottom multiple, annotated by red circles, is suppressed and cannot be seen in up-going wavefield data. However, the down-going wavefield data has the first and second water bottom multiples.

It is noticeable that the receiver-side multiples eliminated by PZ summation technique. However, the source-side first water bottom multiple, annotated by blue circle, still remain in the data.

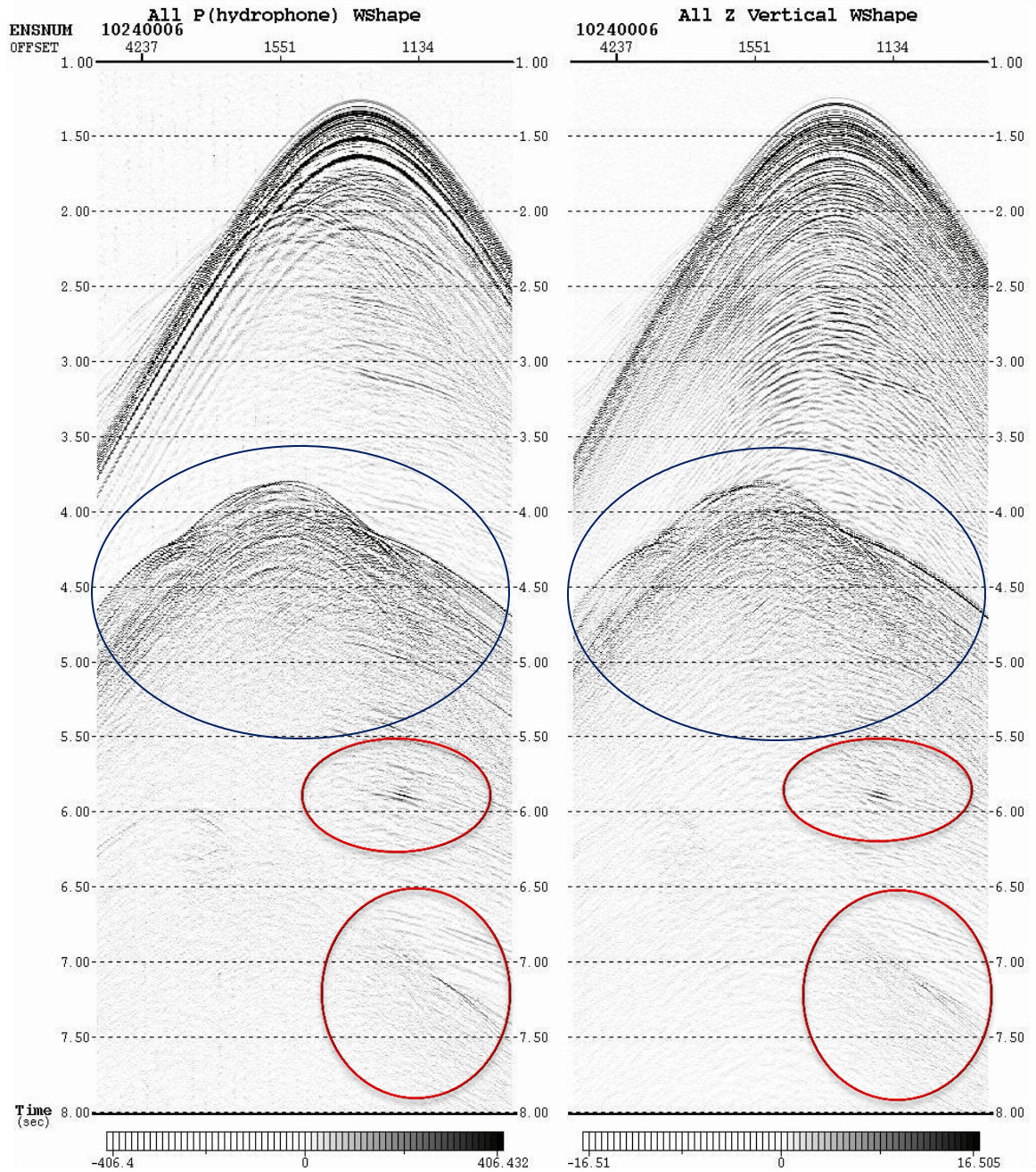


Figure 4.10: Raw pressure (P) and vertical velocity (Z) components before PZ summation. The blue circles indicate the first water bottom multiples. The red circles indicate multiples.

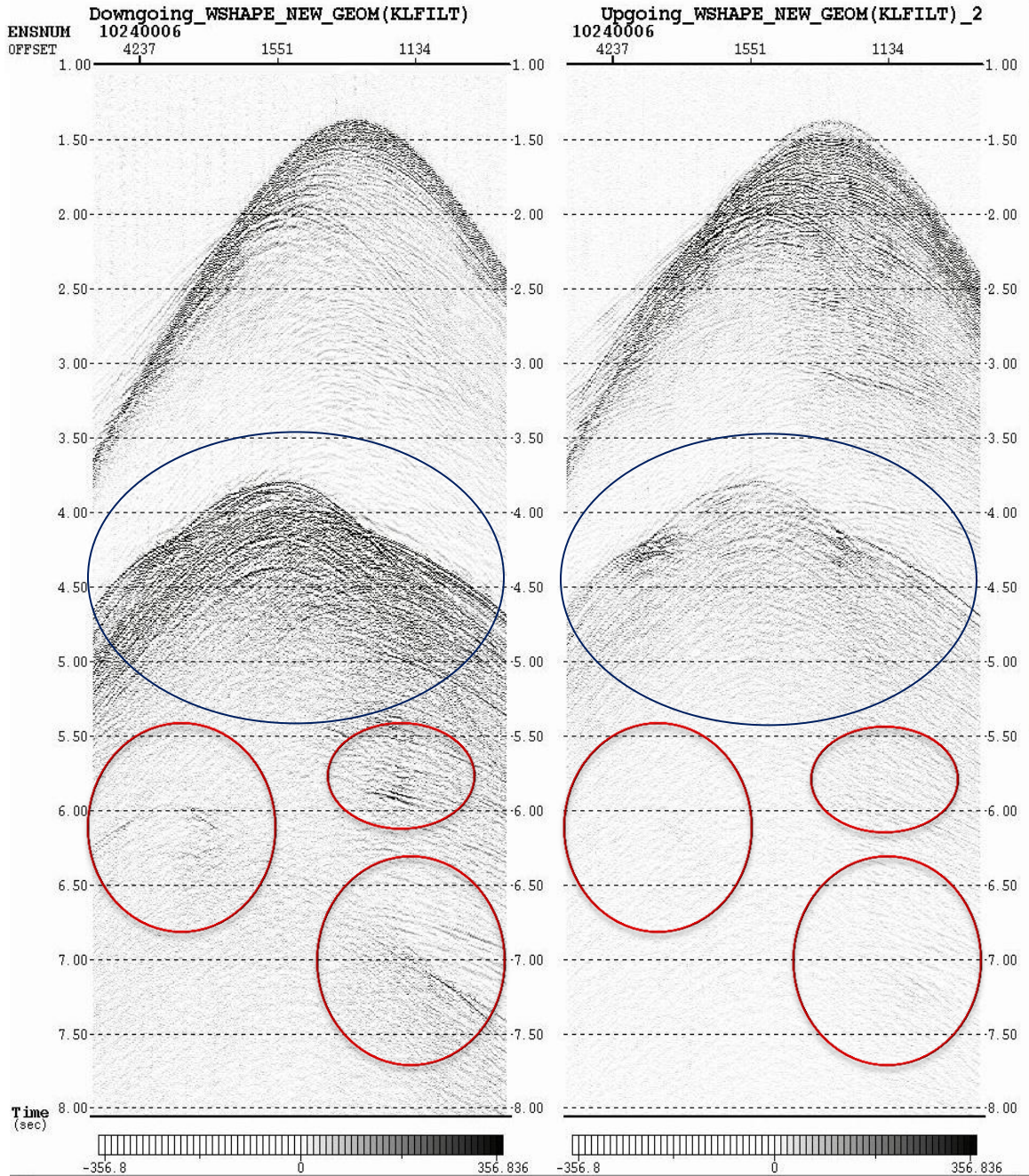


Figure 4.11: Up-going and down-going wavefields after PZ summation. The left side shows down-going data, the right side shows up-going data. The blue circles indicate the first water bottom multiples. The red circles indicate multiples.

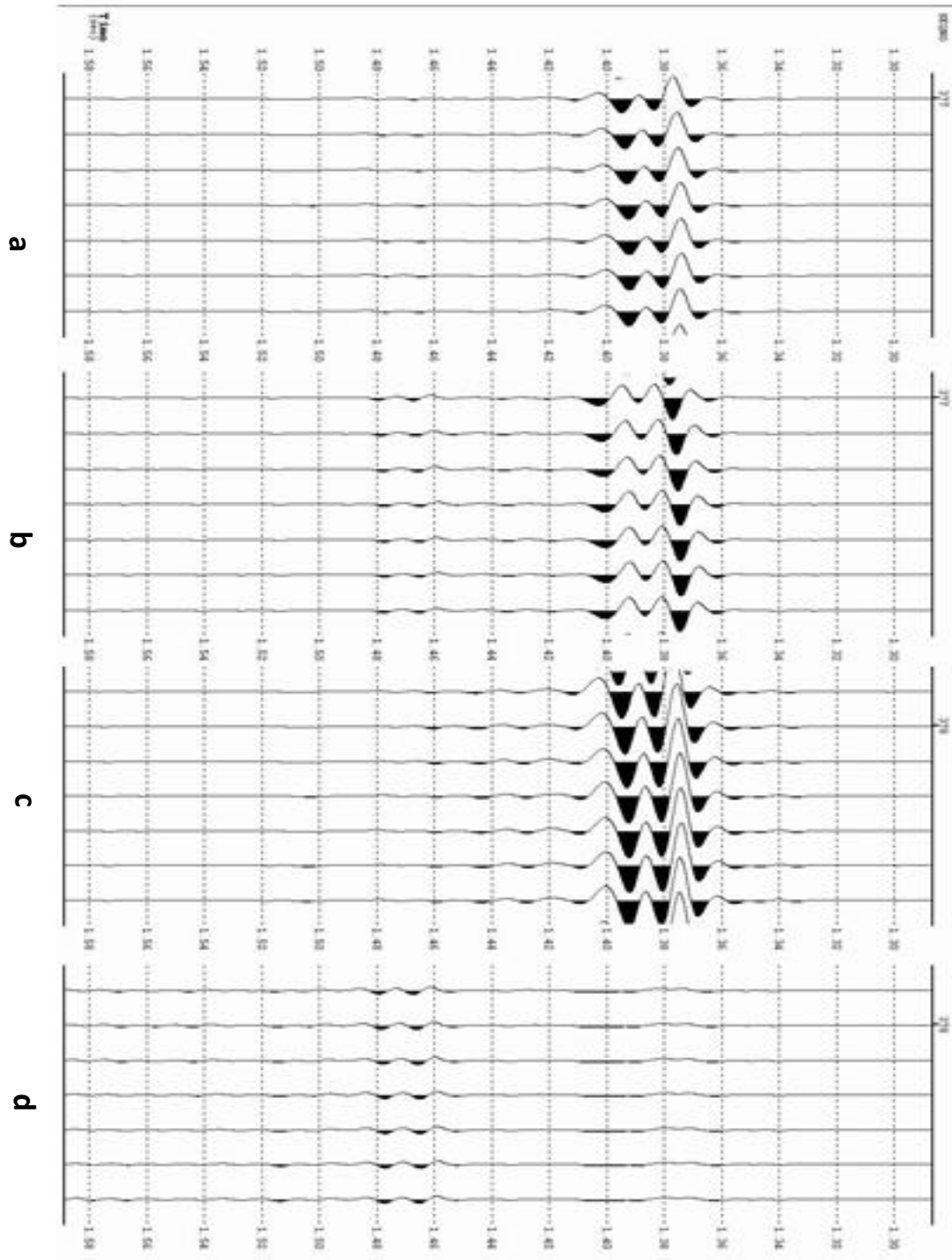


Figure 4.12: a) P component after wavelet shaping. b) scaled Z component after wavelet shaping. c) down-going wavefield after PZ summation. d) Up-going wavefield after PZ summation.

The down-going and up-going data after wavefield separation can be seen in detail in Figure 4.12. Figure 4.12.a shows the wavelet-shaping filter applied pressure data. Since pressure and vertical velocity component data have different amplitudes, the Z (vertical velocity) component was scaled before wavefield separation. The scaled vertical velocity component data is shown in Figure 4.12.b.

After wavelet shaping and scaling the Z component depend on P component, PZ summation was applied to the Seabird's Setrial OBN dataset. Figure 4.12.c shows zoomed in down-going wavefield data and Figure 4.12.d shows zoomed in up-going wavefield data. The direct arrivals are attenuated in up-going data since this section contains predominantly up-going energy.

4.3. Background Velocity Estimation

Estimation of a sufficient background velocity model in areas where the geology is complex is the one of the core challenges in seismic imaging and inversion. The purpose of velocity analysis is to create a model that indicates wave propagation that is similar to the propagation of the real data in medium (Brandsberg-Dahl et al., 1999, Brandsberg-Dahl et al., 2003).

As mentioned earlier, ocean-bottom node data is acquired on the sea floor with large distances between nodes. Acquisition with sparse receiver intervals has some disadvantages such as poor illumination and continuity at shallow subsurface (Alerini, 2009).

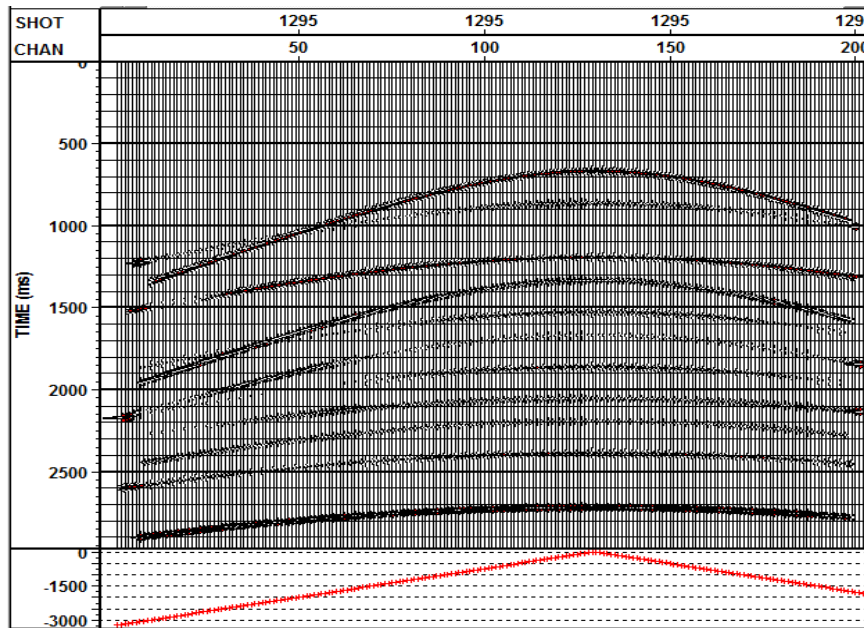
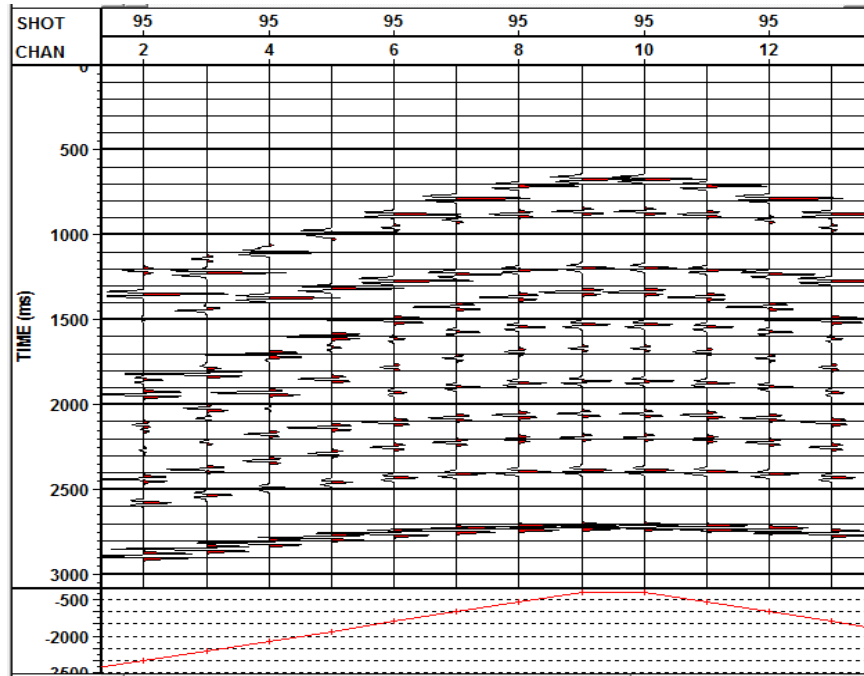


Figure 4.13: Comparison of common-shot gathers for sparsely sampled acquisition (top), the spacing between receivers is 400 m, and common-shot gathers for densely sampled acquisition (bottom), the spacing between receivers is 25 m. Synthetic shot gathers were generated in VISTA by GEDCO.

Figure 4.13 and 4.14 shows that since the illumination is poor at shallow subsurface, events in common-shot gathers (CSGs), common-midpoint gathers (CMGs) and common-image gathers (CIGs) are not continuous and hard to determine. This difficulty causes to have problem for velocity model estimation.

According to Alerini et al. (2009), this difficulty emerges from the small number of receiver locations. If K number of receiver that are covered by dense shot pattern, there are total K^2 traces that can be picked for velocity estimation. Since all picked traces have a reciprocal trace in dataset because of the reciprocity of Green's function, there is only $K^2/2$ traces that contain information from medium. That means if there is small amount of receiver on the sea floor, it is hard to estimate velocity model.

First, conventional PP hyperbolic moveout velocity analysis is performed to estimate background velocity. However, it can be seen from figure 4.15 that, since there are fewer receivers with sparse interval in Seatrial OBN survey, it is hard to pick correct velocities from semblances.

In this work, two different approaches were used to estimate the background velocity model. The first approach is that creating velocity model from migration results. Another approach is picking the correct velocity from common-image gathers (CIGs) and updating the velocity model. Details of these two approaches are explained in imaging from multiples section.

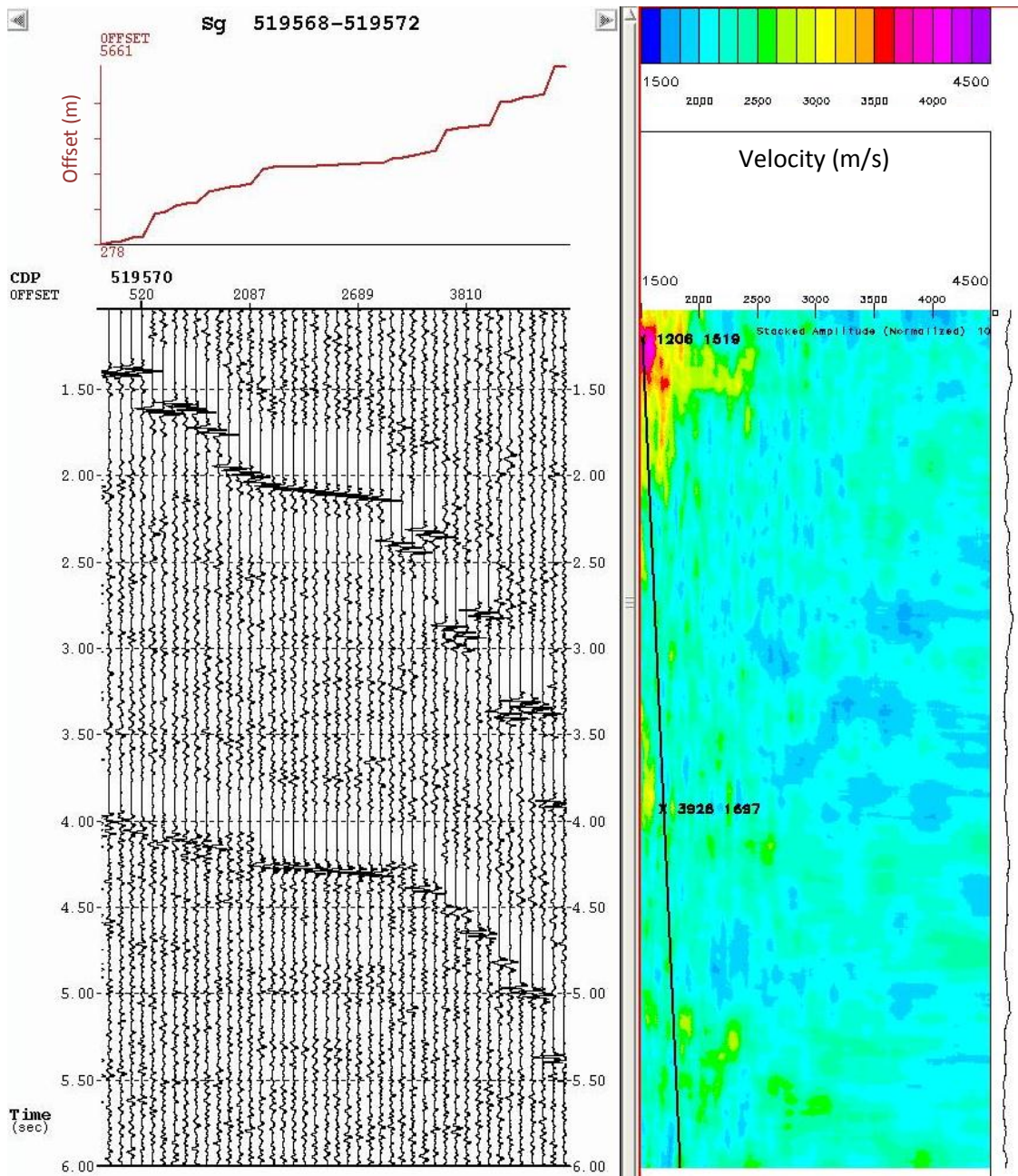


Figure 4.15: Hyperbolic move-out velocity analysis of P component. The right side shows semblance. Purple corresponds to high and blue to low semblance. The left side shows traces in one CDP gather. The red plot on the traces indicates offsets of traces.

4.4. Imaging from Multiples (Mirror Imaging)

As mentioned earlier in the chapter, the economical and practical acquisition geometry for ocean-bottom node survey (OBN) is that using sparse node intervals with dense grid of shots. However, the sparse node geometry provides poor illumination for shallow reflectors which are shallower under the seabed than the node intervals (Grion et al., 2007). Figure 4.16 demonstrated illumination on the sea floor with sparse node intervals.

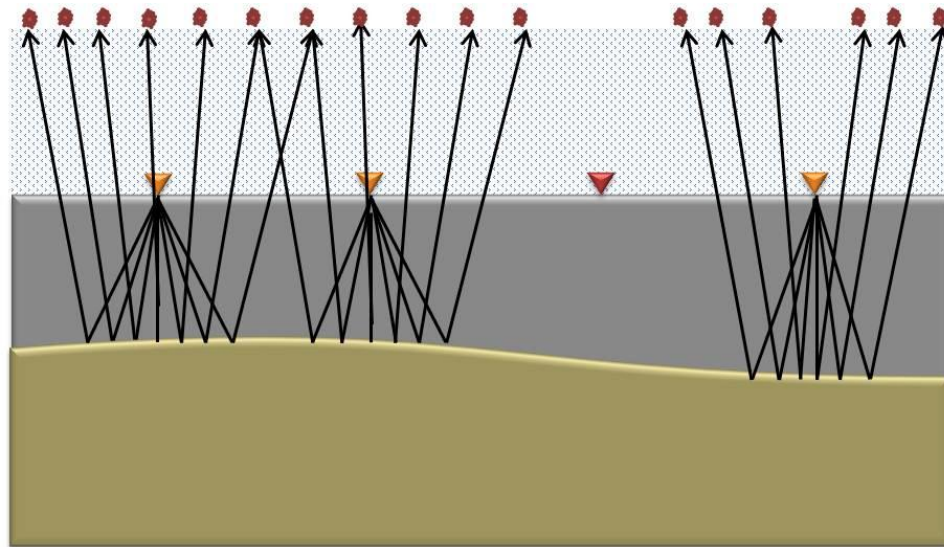


Figure 4.16: Illumination with sparse node geometry. The gaps in shallow reflectors coverage are noticeable. Shots are shown as red dots, live nodes are shown as yellow triangle, and dead node is shown as red triangle. (After Grion et al., 2007)

According to Grion et al. (2007), this problem can be overcome by separating the data from hydrophone and geophone into up-going (U) from down-going (D) waves. The

separation of the wavefields recorded on the sea floor was explained in the previous sections in chapter.

Usually, up-going primary reflections are used to obtain seismic migration section from OBN data (Dash et al., 2009). According to Dash et al. (2009), imaging from the up-going wavefield below the seafloor is more common technique over the up-going wavefield since water later reverberations are both up-going and down-going just above the sea floor. However, migration of the up-going primary wavefield (Figure 4.17) is not good enough for sparse node geometry to image the subsurface structures.

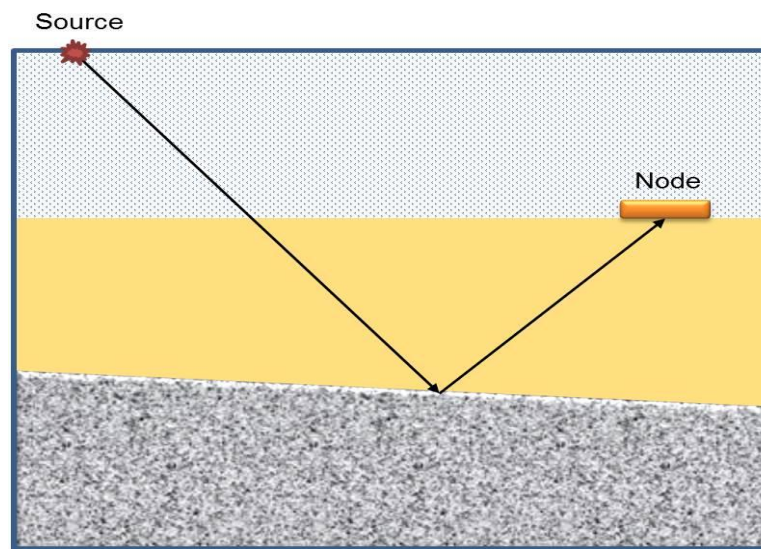


Figure 4.17: Conventional imaging of up-going wave (U) just below the sea floor.

The OBN multiples (down-going wavefield) can be used to have a better structural image of subsurface from wider angles (Godfrey et al., 1998, Ronen et al., 2005, Grion et al., 2007). The multiples reflect from the same reflectors which the

primary waves reflect from. However, multiples take longer wave path and cover wider area than primaries.

Another advantage of multiples over the primaries is that multiples can provide more information than primaries. This is because multiples consist of up-going primaries that reverberate once in the water layer.

Migration of the OBN data by using multiples (down-going receiver ghosts) is called mirror imaging because the sea surface takes the role as a mirror which reflects the image of subsurface structure (Dash et al., 2009). Figure 4.18 demonstrates the ray paths of down-going wave and mirror imaged down-going wave.

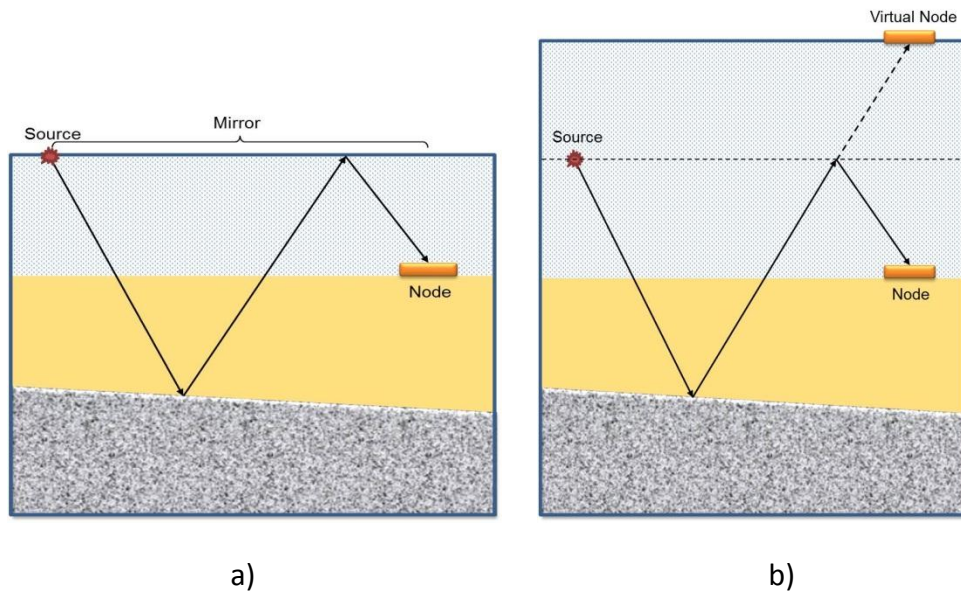


Figure 4.18: Ray paths of down-going (a) wave and mirror imaged down-going (b) wave. Down-going wave can be imaged as primaries recorded on a sea surface twice as high. The sea surface acts like a mirror for primary reflections. The down-going multiple is an up-going primary reflected downward at the sea surface. (After Grion et al., 2007)

According to Liu et al. (2011), imaging of multiples (down-going receiver ghosts) provides better and extended illumination of subsurface reflectors than imaging primaries. This is because primaries cannot reach the shadow zones to illuminate. However, multiples can penetrate into the earth to illuminate the shadow zones. Figure 4.19 shows the illumination of up-going wave and down-going wave. It can be seen from figure that number of rays is the same in both Figure 4.19.a and Figure 4.19.b, however in the Figure 4.19.b (mirror imaging) rays are distributed over wider area.

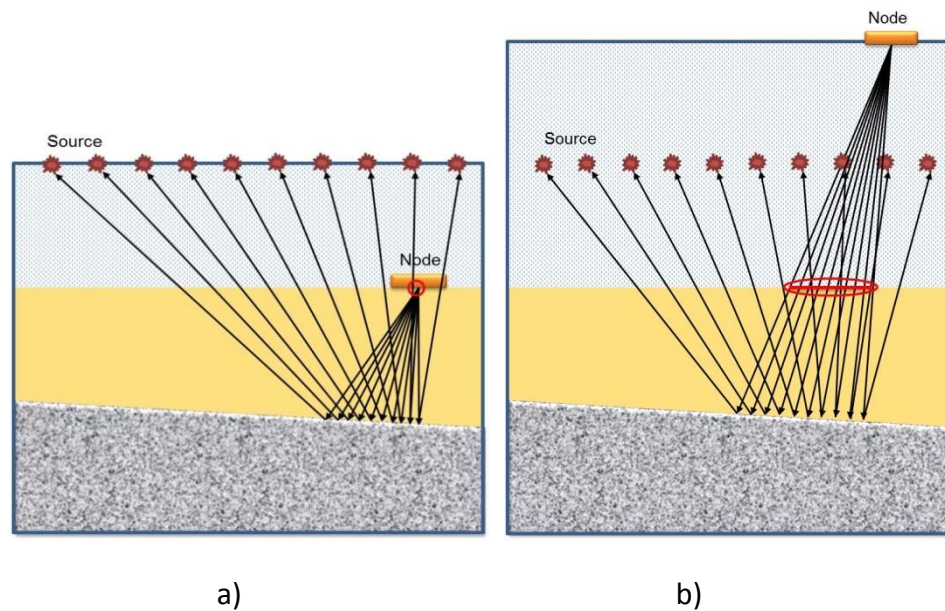


Figure 4.19: Illumination of the up-going (a) wave and down-going (b) wave. It is clear that up-going wave has narrow illumination than down-going wave. Red circles are shows illuminated area.

However it is important to note that illumination also depends on the velocity model. Therefore, it might be possible that conventional imaging could provide better illumination than mirror imaging for a given velocity model (Grion et al., 2007).

4.4.1. Mirror Imaging with Kirchhoff Pre-stack Time Migration

Field data example

I performed the mirror imaging method on Seatrial Atlantis real OBN dataset provided by Seabird Exploration. Since OBN data is acquired with sparse receiver geometry, it's difficult to estimate background velocities from hyperbolic move-out velocity analysis. I used different approaches to estimate velocities from Seatrial OBN dataset.

I first imaged the data using mirror image technique with different constant velocities range of 1400 to 3000 m/sn with increasing velocity of 25 m/sn. Kirchhoff pre-stack time migration (KPSTM) algorithm adapted for ocean-bottom acquisition geometry is used to image the ocean-bottom data from Atlantis field, Gulf of Mexico. Some of the imaging results with different velocities are shown in Figure 4.20.

I then estimate the background velocity model by picking the specific events from these results. Figure 4.20 shows the picking events which are annotated in yellow circles. These yellow circles indicate that this velocity can be considered as correct velocity for this area of image.

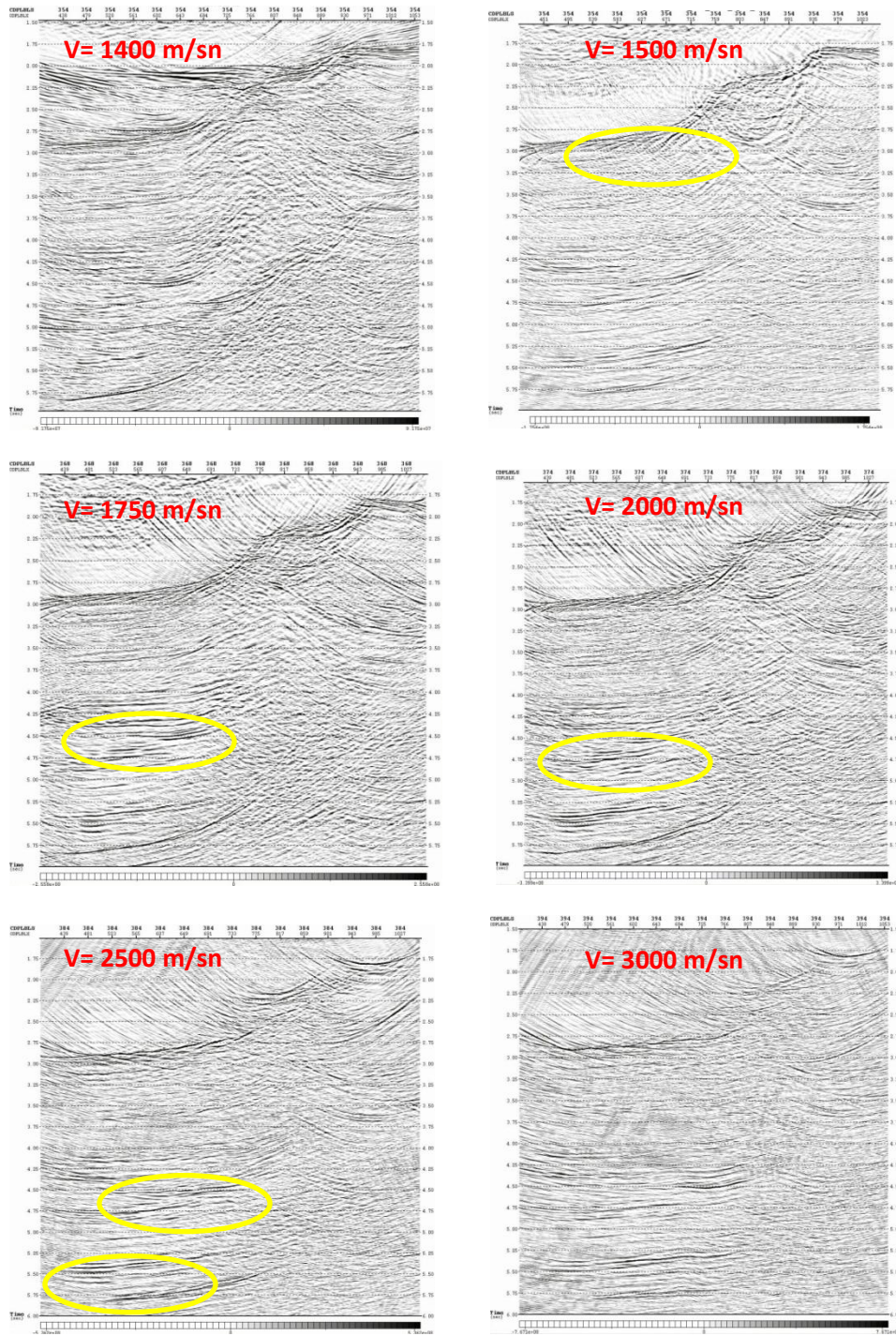


Figure 4.20: KPSTM mirror imaging result with different constant velocities for Seatrial OBN data. The yellow circles indicates the events that are picked to create the velocity model.

Figure 4.21 shows the RMS (root mean square) velocity model which is created with the new picked velocities. This velocity model is used in Kirchhoff pre-stack time migration algorithm to image the Seatrial OBN dataset. Figure 4.22 shows the mirror image (imaging the down-going wavefield) with new velocity model.

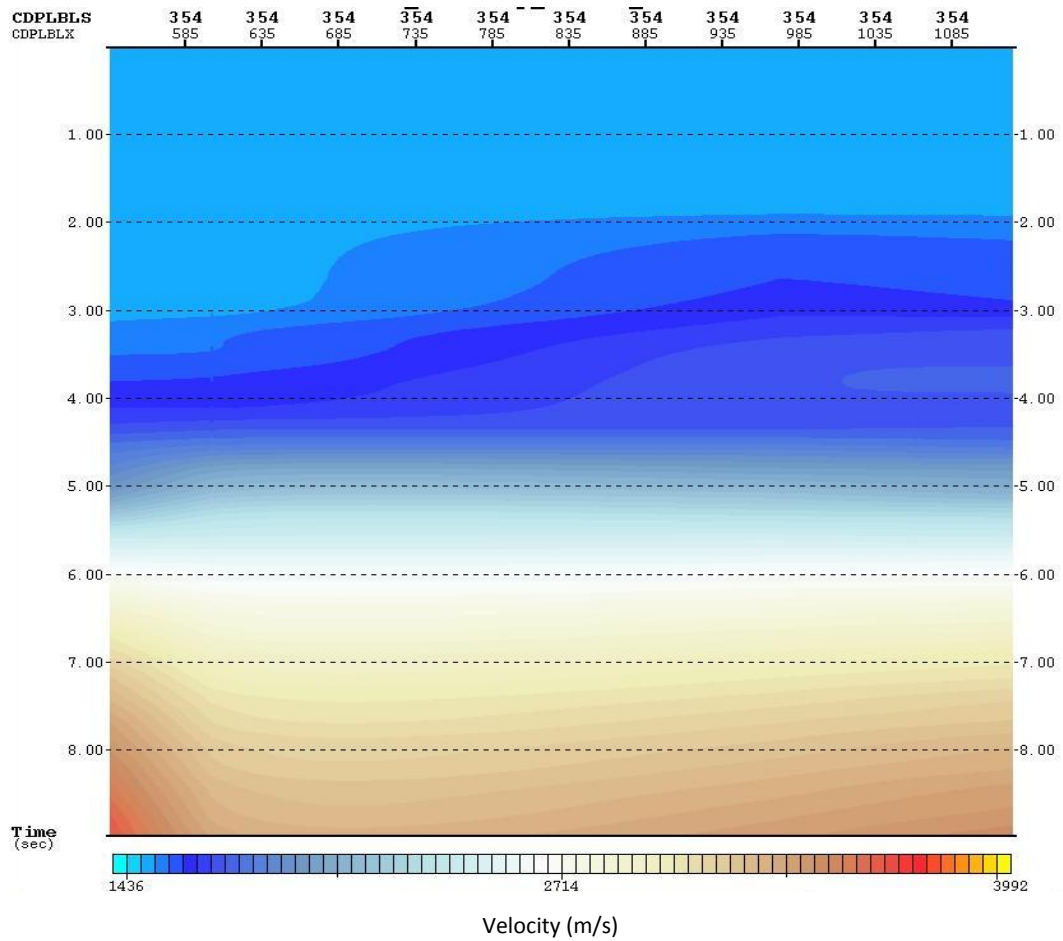


Figure 4.21: RMS velocity model for Seatrial OBN data from picked velocities.

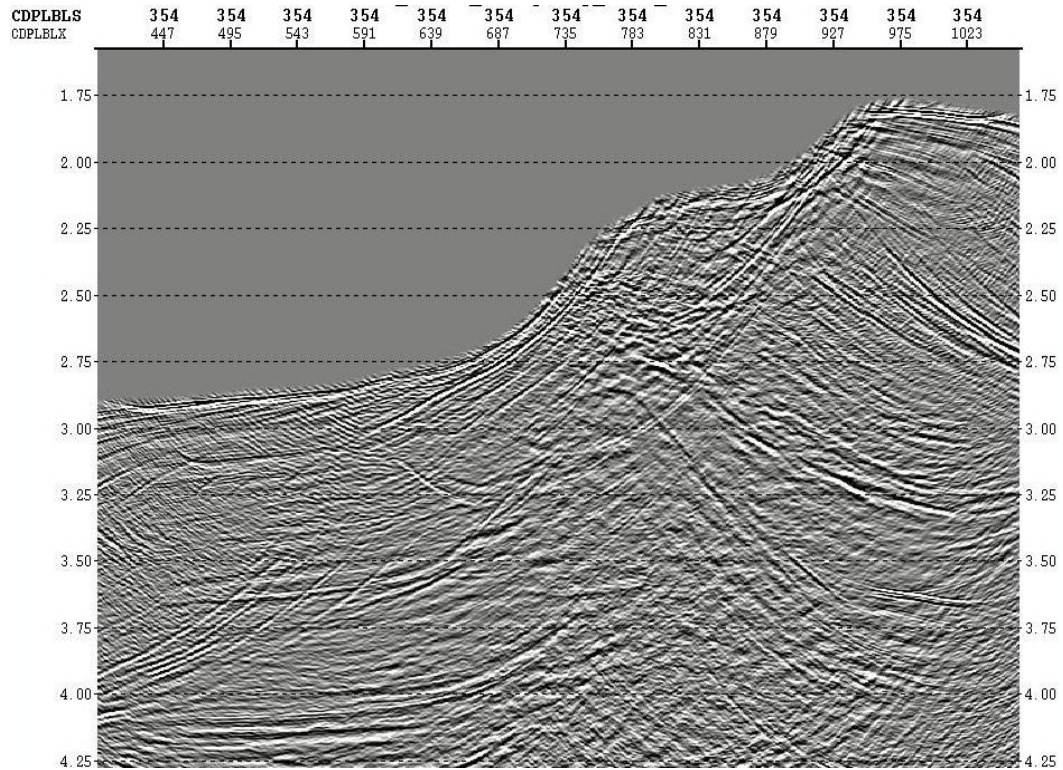


Figure 4.22: Mirror image with RMS velocity model.

I then used the common-image gathers (CIGs) from the migrated down-going wavefield section, shown in Figure 4.22, to update the RMS velocity model. CIG velocity analysis window is shown in Figure 4.23. I picked the events, shown in Figure 4.23 and annotated with pink line, from common-image gathers and updated the RMS velocity model. The new updated RMS velocity model is used to image the down-going wavefield of the Seatrial OBN data. I repeated this process until I obtained better image quality from the down-going wavefield. Final updated RMS velocity model (Figure 4.24) was used to image both up-going and down-going wavefields from Seatrial OBN dataset. The imaging results with updated RMS velocity model can be seen in figure 4.25.

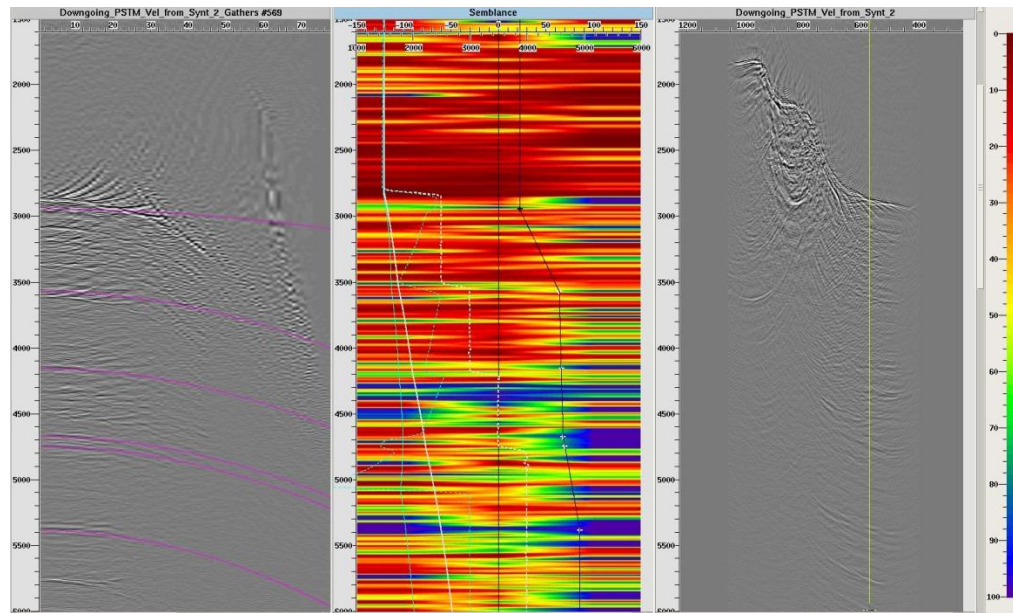


Figure 4.23: Stacking velocity analysis window to update the velocity model from CIGs. The left side shows common image gathers, middle of the figure represents semblance window, and right side represents the stacked section.

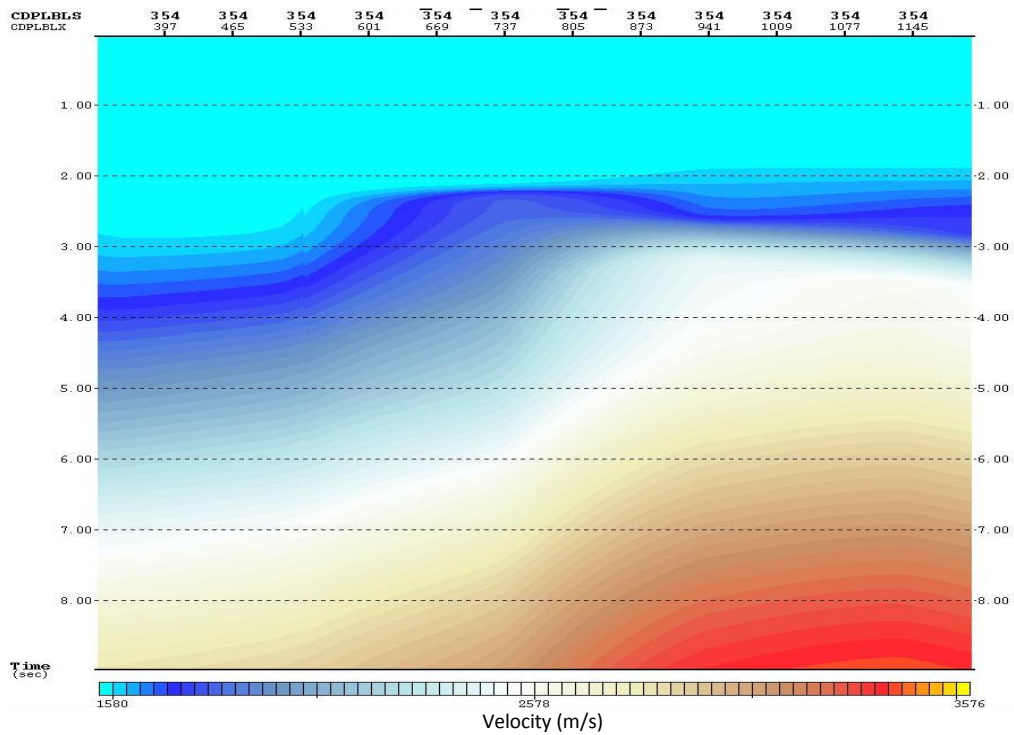


Figure 4.24: Final updated RMS velocity model

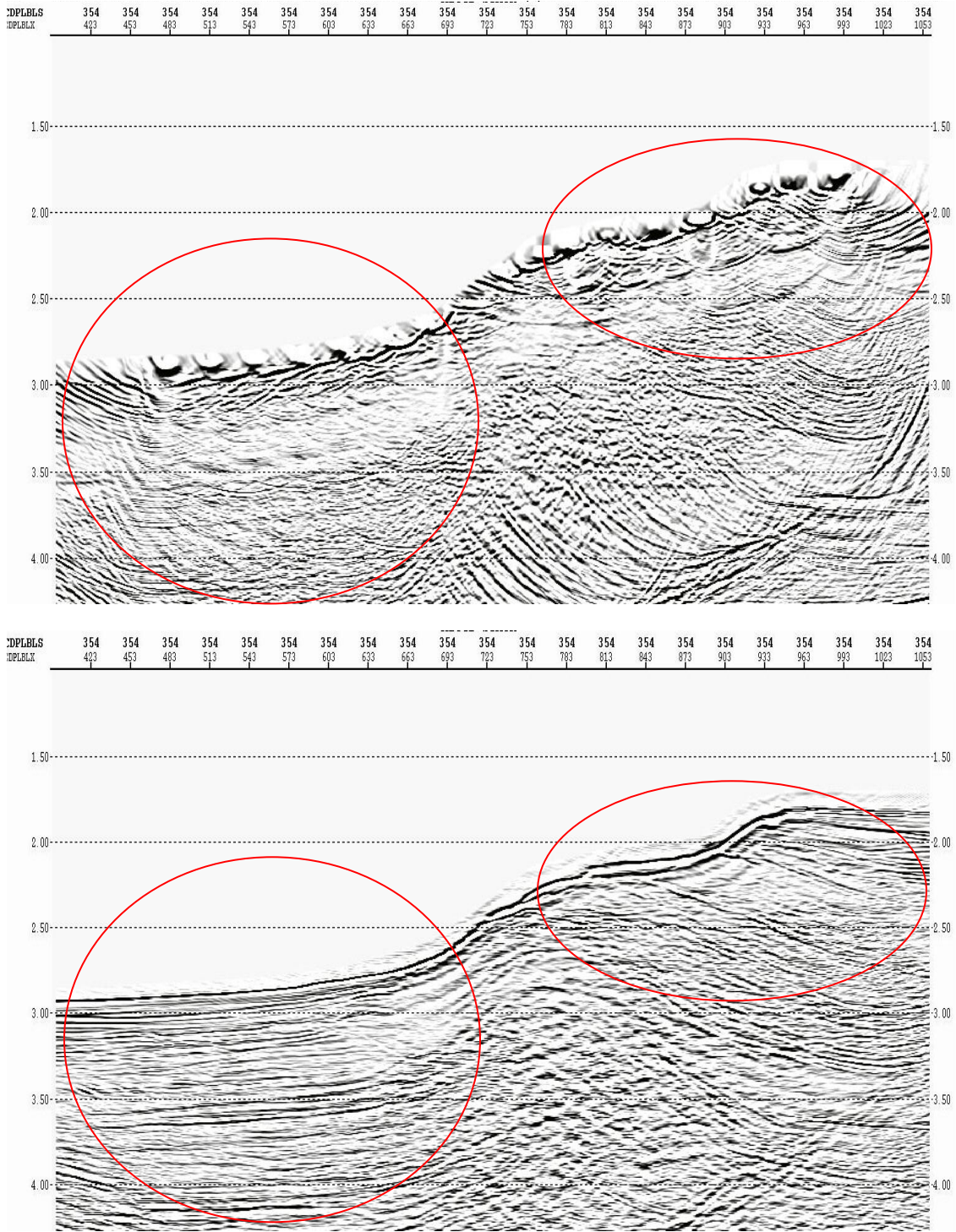


Figure 4.25: In-line time migrated sections of the Seatrial OBN data. Conventional imaging of up-going waves (top) and mirror imaging of down-going waves (bottom).

image of the up-going primary reflections. We then stacked up-going and down-going images to see the result. The result of stacking images is shown in Figure 4.26. It can be seen in the stacked section of up-going and down-going images (Figure 4.26) that shallow targets are better imaged than conventional up-going image.

4.4.2. Mirror Imaging with Kirchhoff Pre-stack Depth Migration

Kirchhoff pre-stack depth migration method is one of the most commonly used migration method by industry. The Kirchhoff integral used for migration (Schneider, 1978; Docherty, 1991; Audebert, et al., 1997; Bleistein and Gray, 2001) is based on Green's theorem (Morse and Feshbach, 1953) and a high-frequency approximation of the wave-equation.

I applied the Kirchhoff pre-stack depth migration (KPSDM) algorithm, adapted for ocean-bottom acquisition, to the up-going primary wavefield and the down-going first order multiple of the Seatrial OBN real dataset. The input interval velocity model for the travel time computation was obtained from final updated RMS velocity model which was used for Kirchhoff pre-stack time migration. The initial interval velocity volume was then updated from five 1D vertical velocity functions which are obtained from previous works. The P-wave velocity volume for Atlantis field from previous works can be seen in Figure 4.27 (Gherasim et al., 2010). Figure 4.28 represents the final interval velocity model that we created. Figure 4.30 shows the results of KPSDM.

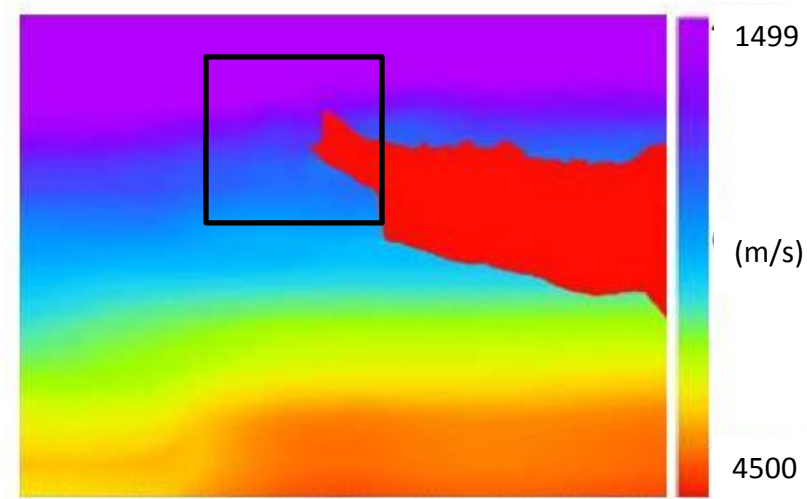


Figure 4.27: P-wave velocity volume in depth for Atlantis field (Gherasim et al., 2010). The black square area indicates our approximate area of coverage.

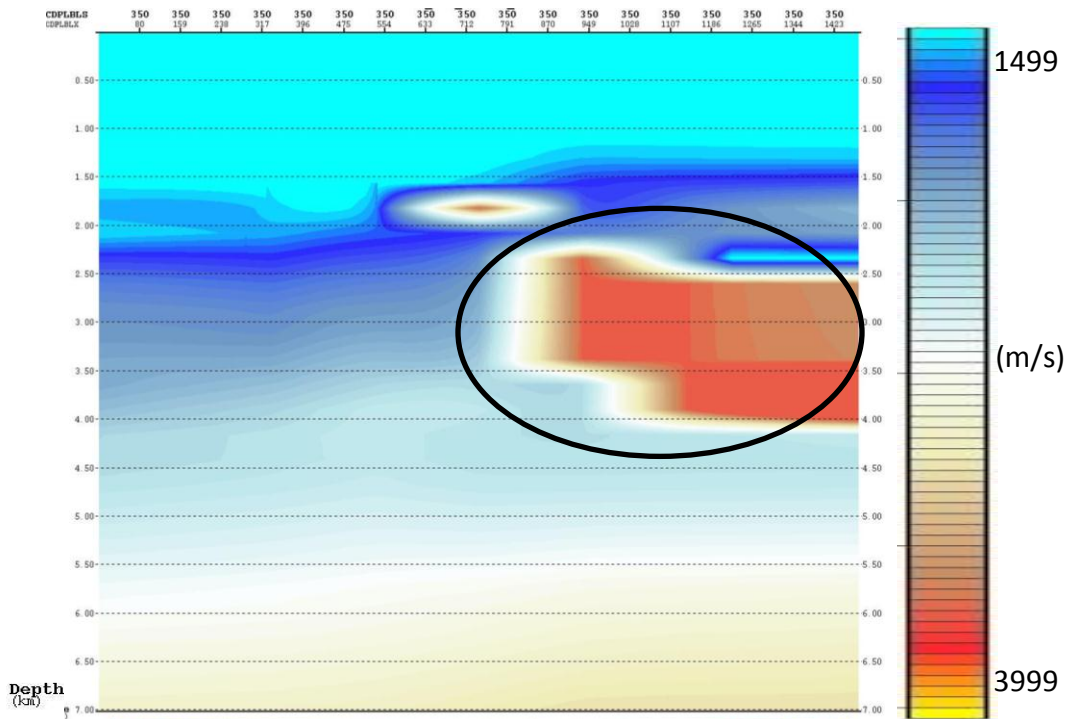


Figure 4.28: The final interval velocity model. The black circle indicates the salt body.

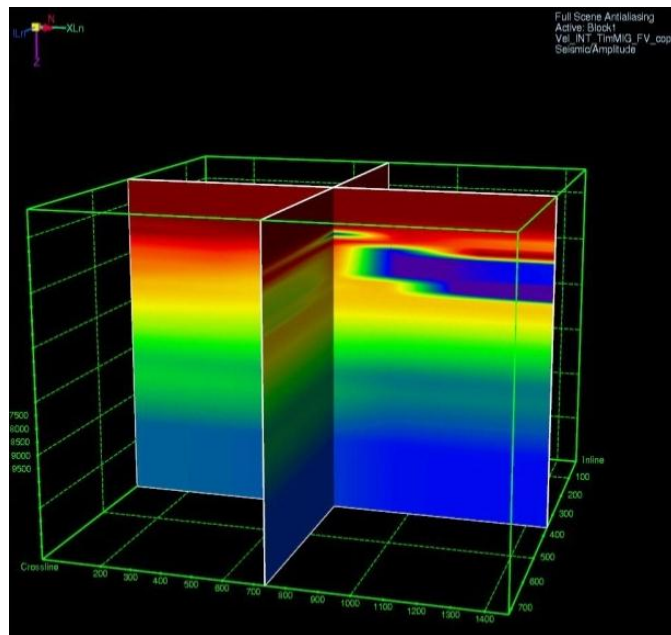
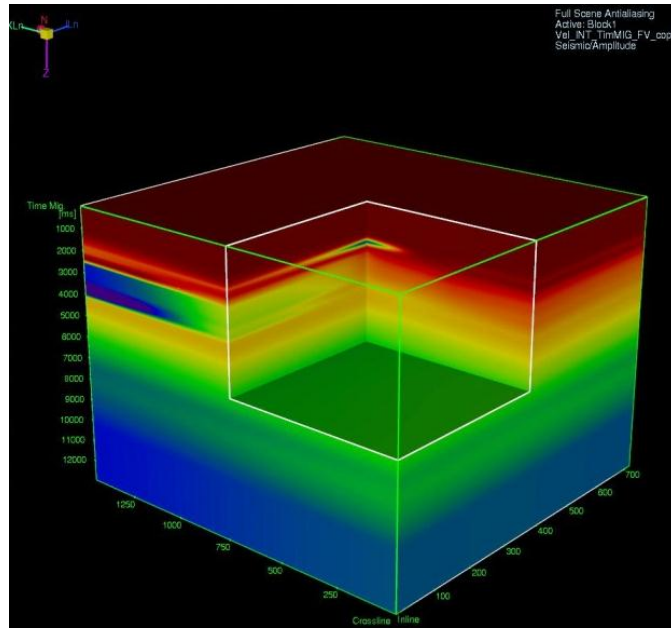


Figure 4.29: The final interval velocity volume in 3D view. Chair display (top) and inline-crossline display (bottom).

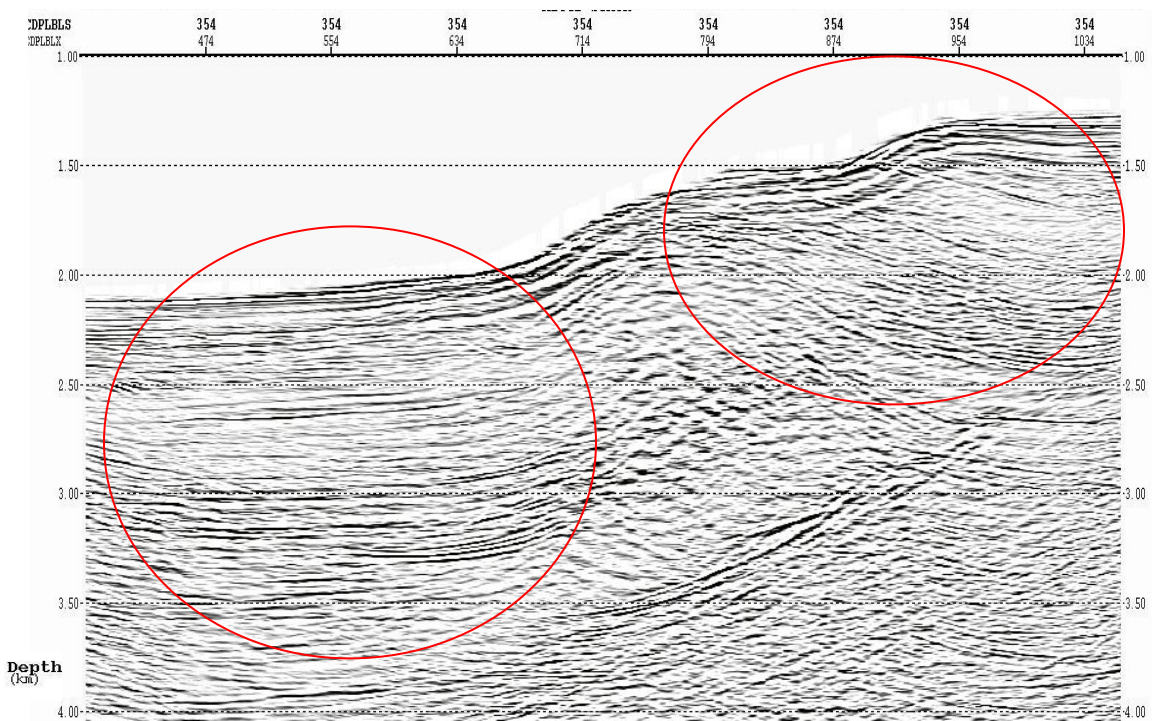
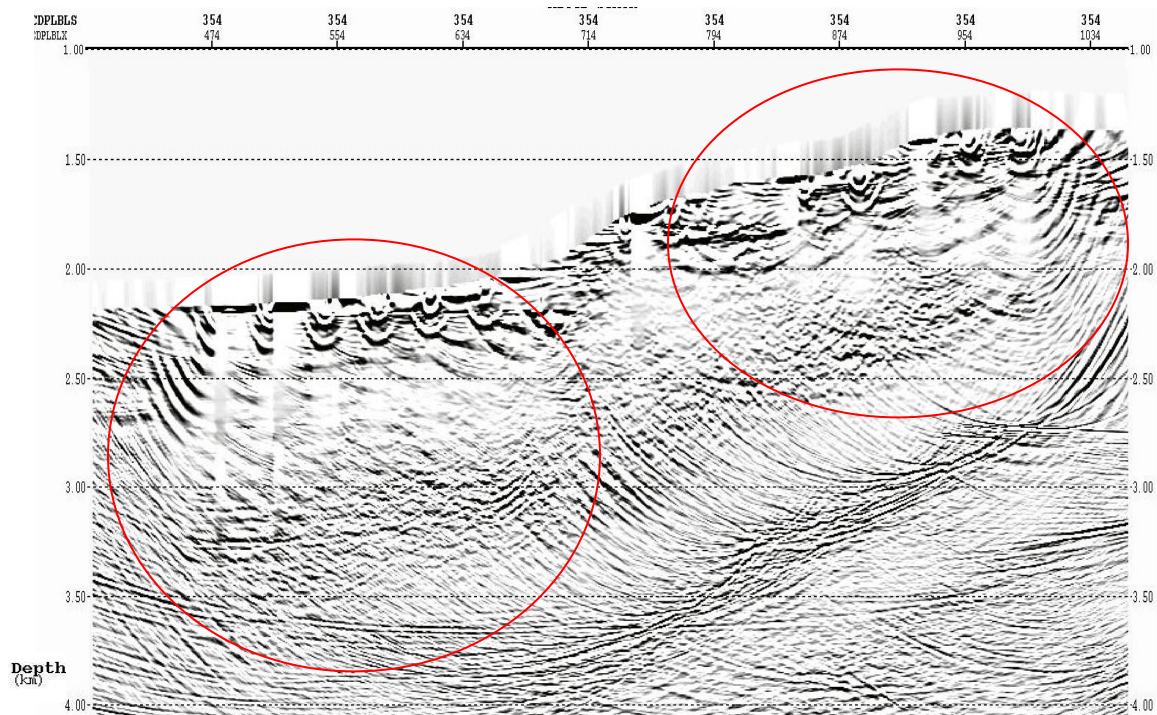


Figure 4.30: Inline depth migrated sections of the Seatrial OBN data. Conventional imaging of up-going waves (top) and mirror imaging of down-going waves (bottom).

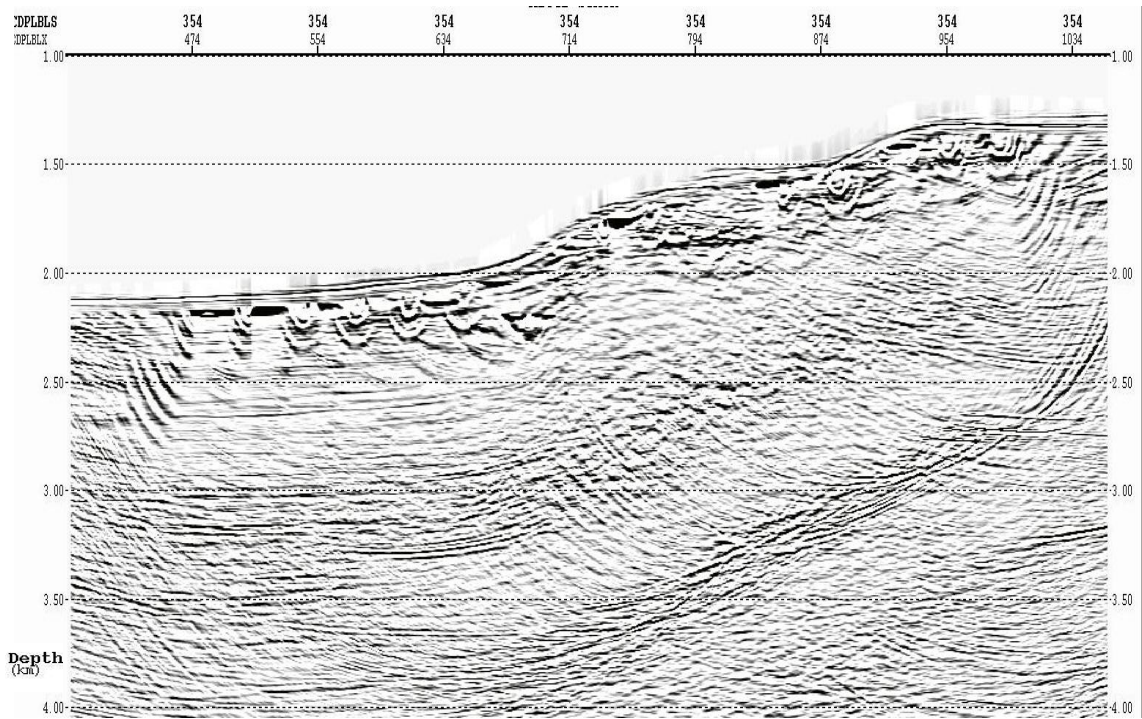


Figure 4.31: Stacked image of PSDM up-going image and down-going image.

Figure 4.30 shows Kirchhoff pre-stack time migration results for up-going wavefield with conventional imaging and down-going wavefield with mirror imaging. Figure 4.31 shows the stacked image section of up-going depth image and down-going depth image. As pre-stack depth migration, it is clear that mirror imaging of down-going waves has better image quality for shallow subsurface than conventional up-going imaging. Combining the up-going image and down-going image also improve image quality of shallow area over the up-going imaging.

4.4.3. Mirror Imaging with Reverse Time Migration (RTM)

Many researchers have successfully used the recent advances in seismic imaging technology to solve salt-related problems (O'Brien et al., 1996; Kessinger et al., 1996; Rosenberg, 2000; Glogovsky et al., 2002; Huang et al., 2009; Liu, F. et al., 2009). However, imaging the subsalt area is still challenge in Gulf of Mexico, since primary reflections are unable to illuminate complicated subsalt areas (Liu et al., 2011).

Reverse time migration (RTM) can be used as a tool for the migration of multiples. Other tools which are used for migration of multiples are Kirchhoff and one-way wave-equation migrations. RTM uses the full wave-equation modeling to image the data (Baysal et al., 1983). That is why reverse time migration is a powerful tool which can effectively handle multi-arrival seismic waves. RTM is the most accurate technique since it uses the entire wavefield for imaging. However, it is also the most sensitive imaging technique to velocity errors (Liu et al., 2011). The imaging condition for RTM of multiples can be found in appendix C.

In this part of this study, I used RTM algorithm which is modified to image multiple reflection to their correct location in the subsurface. RTM migration was applied both synthetic and field dataset.

4.4.3.A. Synthetic Data Example

To understand mirror image technique with reverse time migration (RTM) algorithm, I first perform this imaging technique on a synthetic dataset which was generated from the Seatrail Atlantis OBN survey by using 3D finite-differences method. The synthetic model and dataset was explained in Chapter 2.

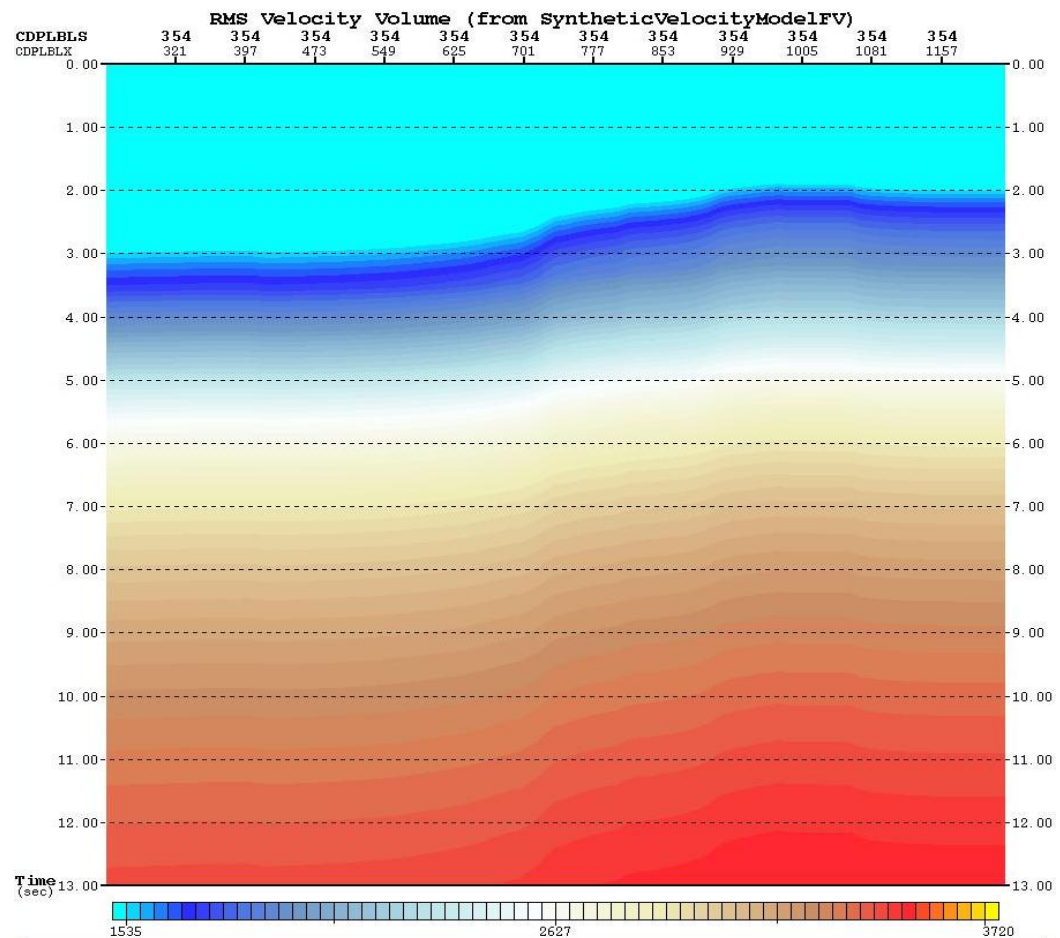


Figure 4.32: Synthetic RMS velocity model for a single inline.

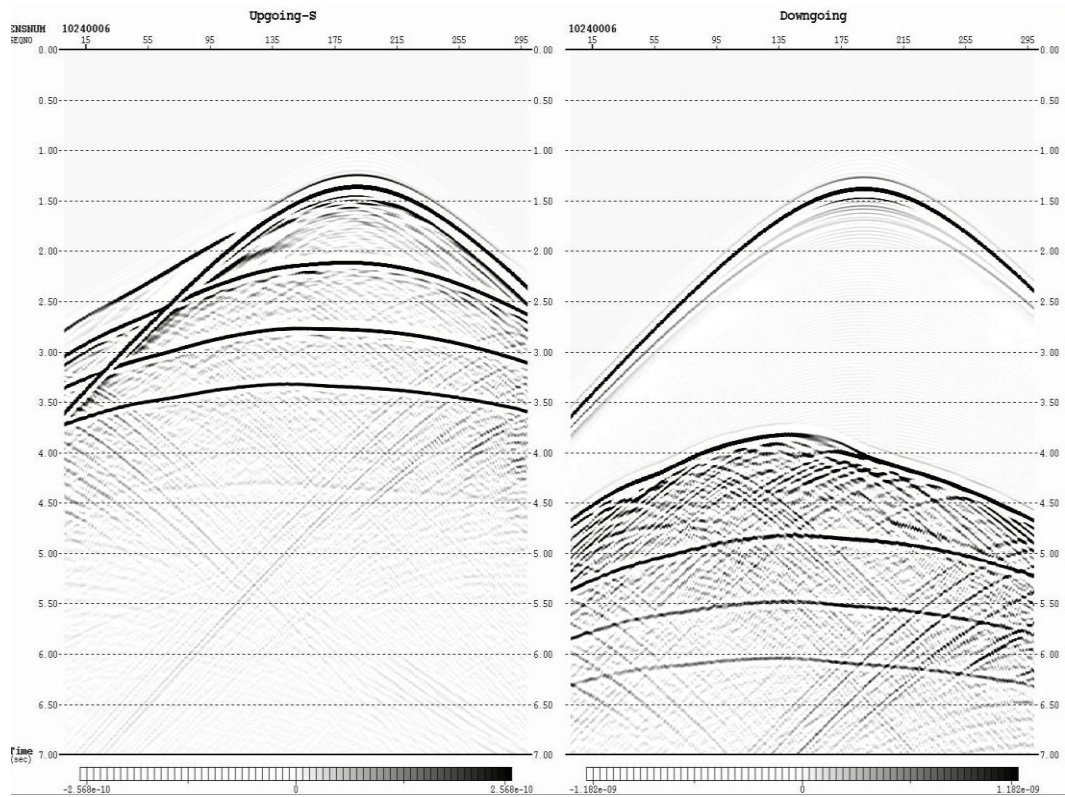


Figure 4.34: Synthetic Up-going and down-going data for the same shot and same node.

The result of conventional reverse time migration of up-going wave and the RTM image which is obtained from down-going wave with the mirror imaging technique can be seen in Figure 4.35. It is clear that seafloor cannot be imaged with the up-going waves but it can be imaged by down-going waves.

It can be concluded from the synthetic example that the image from down-going waves with mirror method provide better image than the image from up-going primaries. The main reason is that the illumination is better and wider in mirror method, especially in shallow areas.

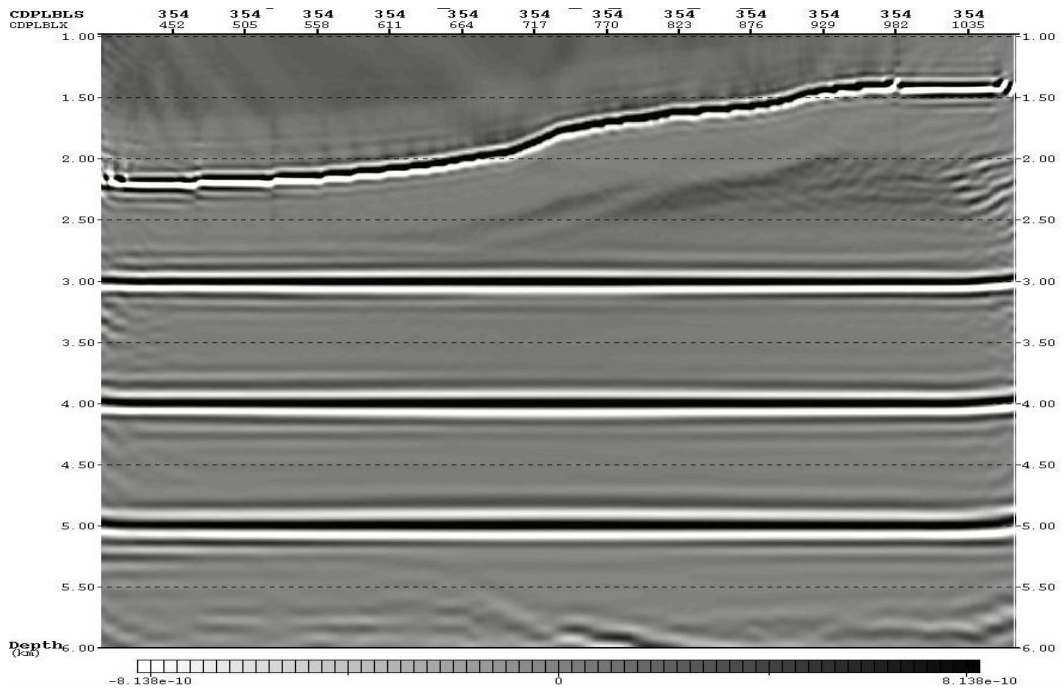
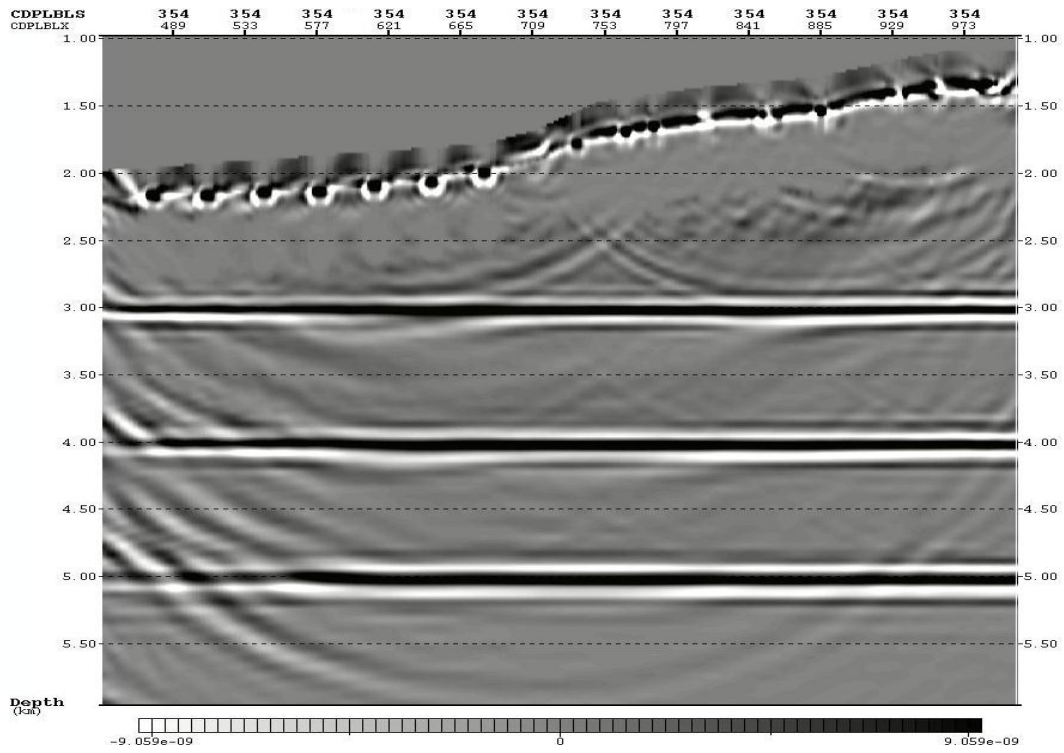


Figure 4.35: Inline RTM sections of the synthetic up-going and down-going data. Conventional RTM of up-going waves (top) and mirror imaging RTM of down-going waves (bottom).

It can be summarized from Figure 4.35 that reverse time migration algorithm can be used to image of down-going ghost. It is also clear that mirror imaging RTM result of down-going wave has better image quality than conventional RTM of up-going primary wave has. The node location on the sea floor can be clearly seen in conventional up-going imaging; however the image of sea floor in the mirror imaging of down-going wave was better illuminated and node locations cannot be identified.

4.4.3.B. Field Data Example

I used the field up-going primary and down-going multiple data to obtain images with RTM method. The Seabird Atlantis OBN dataset are used to separate wavefield into up-going and down-going (Figure 4.11).

The results of up-going and down-going imaging with reverse time migration are shown in Figure 4.36. The figure explains that mirror imaging with RTM successfully applied to field data. Since we don't have exact depth velocity model, image quality is not perfect. This is because RTM is the most sensitive migration technique to velocity. However, improvement of image quality in down-going mirror image (Figure 4.36 bottom) can be clearly seen. The image quality of water bottom and shallow subsurface area which are annotated with red circles in Figure 4.36 is poor in conventional up-going image. These areas, however, are well imaged in down-going mirror image. I then stacked the RTM result of up-going and down-going images. Figure 4.37 shows the

stacked RTM section of up-going and down-going RTM images. If it is compared to conventional up-going RTM result in Figure 4.36 (top), it is clear that shallow area has more information than conventional up-going RTM image.

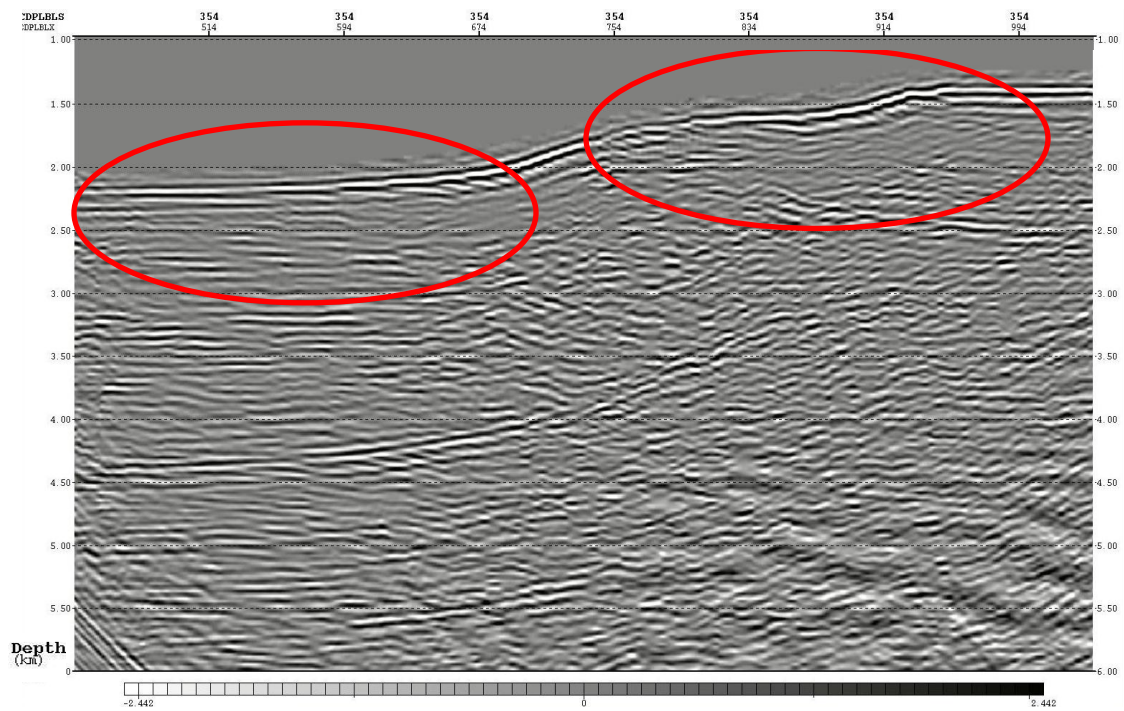
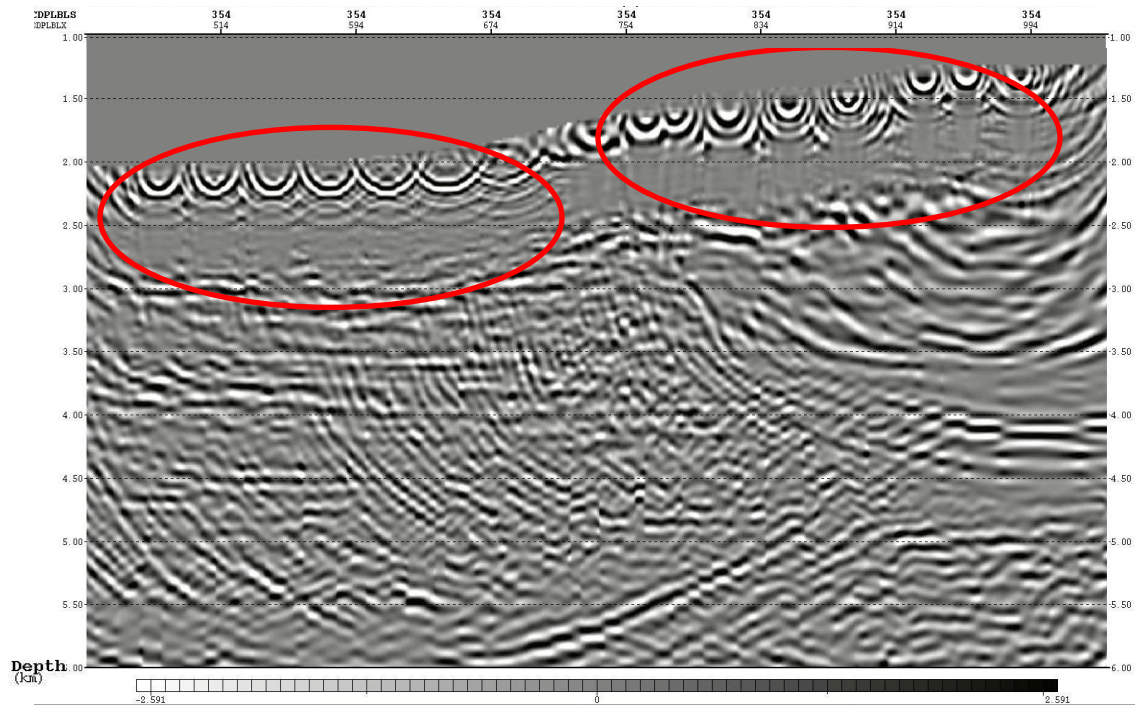


Figure 4.36: Inline RTM sections of the real Seabird OBN up-going and down-going data. Conventional RTM of up-going waves (top) and mirror imaging RTM of down-going waves (bottom).

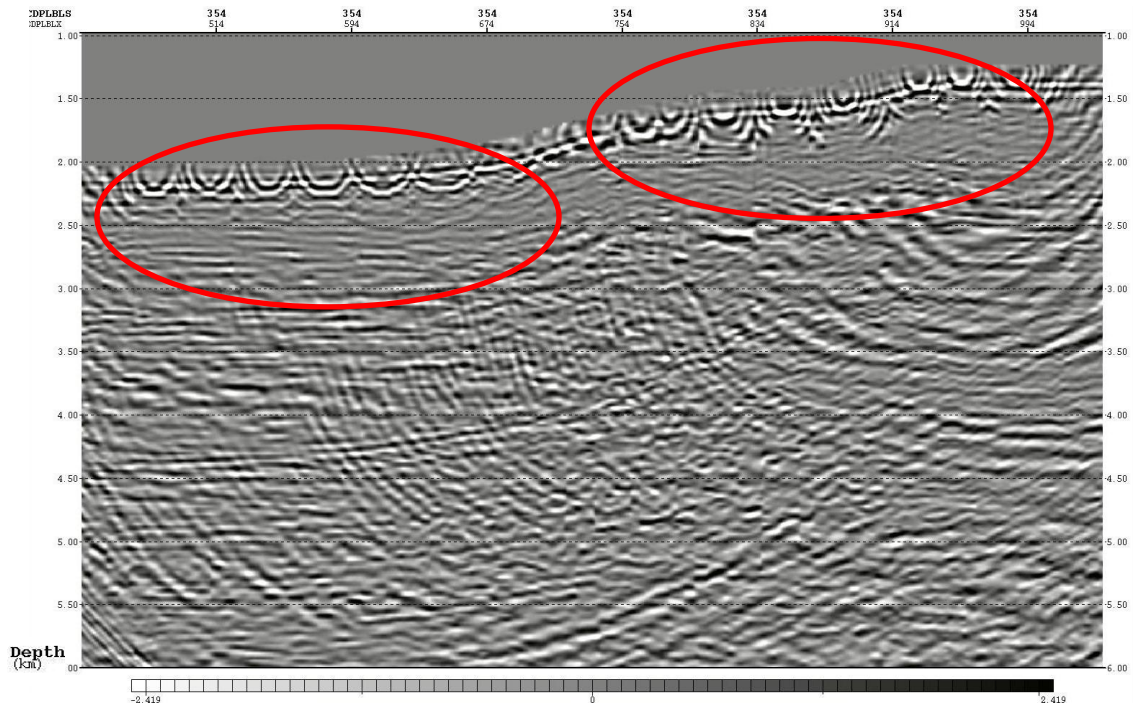


Figure 4.37: Stacked image result of RTM up-going image and RTM down-going image.

Chapter 5

CONCLUSION

Ocean-bottom node (OBN) technology is a new technique to acquire the seismic data from ocean-bottom. There are many advantages of using ocean-bottom nodes on the seafloor to record the data, such as obtaining full azimuth dataset, recording converted waves, and separated wavefield into up-going and down-going wavefields. Another important advantage of ocean-bottom nodes is flexibility. They can be deployed almost anywhere. This advantage provides us an opportunity to combine ocean-bottom nodes with another survey such as VSP survey. We designed many surveys and concluded that combining of ocean-bottom nodes with VSP survey will enhance the azimuth and offset distribution of the VSP survey.

A main challenge with the ocean-bottom nodes is now processing and imaging of the data. Acquiring the data on the sea floor from deep water, with a large distance between nodes makes the conventional processing steps difficult to apply for OBN datasets. The imaging of data from ocean-bottom nodes (OBNs) is negatively affected from poor illumination and sensitivity to velocity anomalies. These are important problems for imaging data from ocean-bottom. Fortunately, we described in this study that there is an effective solution for these problems. According to Grion et al. (2007), this problem can be overcome by separating the data from hydrophone and geophone into up-going (U) from down-going (D) waves.

Usually, up-going primary reflections are used to obtain seismic migration section from ocean-bottom. However, migration of the up-going primary wavefield is not good enough for sparse node geometry to image the subsurface structures. In this study, we showed that we can produce better image quality from the down-going wavefield with mirror imaging technique than the conventional up-going primary wavefield. Obtaining better image from down-going wavefield is because of reduced exposure to shallow inhomogeneous anomalies under the seabed and improved illumination.

References

- Ashton, C.P., Bacon, B., Mann, A., Moldoveanu, N., 1994, 3D Seismic Survey Design, *Oilfield Review*, 6, no. 02, 19–32.
- Alerini, M., S. Le Bégat, G. Lambaré, and R. Baina, 2002, 2D PP- and PS-stereotomography for a multicomponent dataset: 72nd Annual International Meeting, SEG, Expanded Abstracts, 838–841.
- Alerini, M., Traun, B., Ravaut, C., and Duveneck, E, 2009, Prestack depth imaging of ocean-bottom node data, *Geophysics*, Vol. 74, No. 6.
- Amundsen, L., and Reitan, A., 1995, Decomposition of multicomponent seafloor data into up-going and down-going *P*- and *S*-waves: *Geophysics*, 60, 563–572.
- Audebert, F., D. Nichols, T. Redkal, B. Biondi, D. E. Lumley, and H. Urdaneta, 1997, Imaging complex geologic structure with single-arrival Kirchhoff pre-stack depth migration, *Geophysics*, 62, 1533-1543.
- Bale, R., 1998, Plane wave deghosting of hydrophone and geophone data: 68th Annual International Meeting, SEG, Expanded Abstracts, 653-656.
- Ball, V., and Corrigan, D., 1996, Dual-sensor summation of noisy ocean-bottom data: 66th Ann. Internat. Mtg., Soc. Expl. Geophys., Expanded Abstracts, 28-31.
- Barr, F. J., and Sanders, J. I., 1989, Attenuation of water-column reverberations using pressure and velocity detectors in a water-bottom cable: 59th Ann. Internat. Mtg., Soc. Expl. Geophys., Expanded Abstracts, 653-656.
- Barr, F. J., 1997, Dual-sensor OBC technology. *The Leading Edge* pp. 45-51.
- Baysal, E., D. D. Kosloff, and W. C. J. Sherwood, 1983, Reverse time migration: *Geophysics*, 48, 1514–1524.
- Beaudoin, G., and Michell, S., 2006, The Atlantis OBS Project: OBS nodes – Defining the Need, Selection the Technology, and Demonstration the Solution, Offshore Technology Conference, 2006, OTC17977
- Beaudoin, G., 2010, Imaging the invisible-BP's path to OBS node, SEG Expanded Abstracts.

- Bleistein, N., and S. H. Gray, 2001, From the Hagedoorn imaging technique to Kirchhoff migration and inversion, *Geophysical Prospecting*, 49, no. 6, 629-643.
- Brandsberg-Dahl, S, De Hoop, M. V., and Ursin, B., 2003, Focusing in dip and AVA compensation on scattering-angle/azimuth common image gathers, *Geophysics* 68, 232-254
- Brandsberg-Dahl, S., De Hoop, M.V., and Ursin,B., 1999, Velocity analysis in the common scattering-angle/azimuth domain: 69th Ann. Internat. Mtg., SEG, Expanded Abstracts, 1715–1718.
- Brzostowski, M., Altan, S., Zhu, X., Barkved, O., Rosland, B. and Thomsen, L., 1999, 3-D converted-wave processing over the Valhall Field: Annual Meeting Abstracts, Society Of Exploration Geophysicists, 695-698.
- Burch, T., Hornby, B.E., Sugianto H., and Nolte, B., 2010, Subsalt 3D VSP imaging at Deimos Field in the deepwater GOM, *The Leading Edge*
- Caldwell, J., 1999, Marine multicomponent seismology: *The Leading Edge*, 18, 1274–1282.
- Clarke, R., Xia, G., Kabir, N., Sirgue, L., and Michell, S., 2007, Processing of a novel deepwater, wide-azimuth node seismic survey, *The Leading Edge* 26, 504
- Cordson, A., Galbraith, M., Peirce, J., 2000, Planning land 3-D seismic surveys: *Geophysical Developments No. 9, Soc. Expl. Geoph.*, 204pp.
- Dash, R., Spence, G., Hyndman, R., Grion, S., Wang, Y., and Ronen, Shuki., 2009, “Wide-area imaging from OBS multiples”, *Geophysics*,VOL. 74, NO. 6
- Docherty, P., 1991, A brief comparison of some Kirchhoff integral formulas for migration and inversion, *Geophysics*, 56, 1164- 1169.
- Dragoset, W. and Barr, F. J., 1994, Ocean-bottom cable dual-sensor scaling: 64th Ann. Internat. Mtg., Soc. Expl. Geophys., Expanded Abstracts, 857-860.
- Gallant, E.V., Stewart, R.R., Lawton, D.C., Bertram, M.B., and Rodriguez, C., 1996, New technologies in marine seismic surveying: Overview and physical modelling experiments, CREWES Research Report — Volume 8

- Gherasim, M., Etgen, J., Nolte, B., Ahmed, I., Xia, G., Reasnor, M., Howie, J., and Shepherd, D., 2010, Anisotropic velocity model building using OBS node tomography at Atlantis field, Gulf of Mexico, SEG, Expanded Abstracts, 2010.
- Glogovsky, V., E. Landa, and J. Paffenholz, 2002, Integrated approach to subsalt depth imaging: Synthetic case study: *The Leading Edge*, 21, 1217–1223
- Godfrey, R. J., P. Kristiansen, B. Armstrong, M. Cooper, and E. Thorogood, 1998, Imaging the Foinaven ghost: 68th Annual International Meeting, SEG, Expanded Abstracts, 1333–1335.
- Grion, S., Granger, P., Pica, A., and Ronen, S., 2007, OBS Illumination: Primary Problems and Mirror Solutions, International Petroleum Technology Conferences, IPTC 11661.
- Hoffe, BH, Lines, LR, and Cary, PW, 2000, Applications of OBC recording: *The Leading Edge*, 19, 382-391.
- Hornby, B. E., J. A. Sharp, J. Farrelly, S. Hall, and H. Sugianto, 2007, 3D VSP in the deep water Gulf of Mexico fills in sub-salt “shadow zone”: *First Break*, 25, 83–88.
- Howie, J., Mahob, P., Shepherd, D., and Beaudoin, G., 2008, Unlocking the full potential of Atlantis with OBS nodes, SEG, Expanded Abstracts, 363–367.
- Huang, T., Y. Zhang, H. Zhang, and J. Young, 2009, Subsalt imaging using TTI reverse time migration: *The Leading Edge*, 28, 448–452.
- Kessinger, W., and M. Ramaswamy, 1996, Subsalt imaging using mode converted energy and acoustic depth migration: 66th Annual International Meeting, SEG, Expanded Abstracts, 566–569.
- Krey, Th.C. 1987, Attenuation of Random Noise by 2-D and 3-D CDP Stacking and Kirchhoff Migration, *Geophysical Prospecting* 35, 135-147.
- Koster, K., Monk, D., Rokkan, A., Bouraly, R., Brown, S., Brahan, A., Ronen, S., 2011, Imaging drilling hazard in a congested North Sea field using nodel ocean-bottom seismic, *World Oil*, 2011 July.
- Liu, F., G. Zhang, S. A. Morton, and J. P. Leveille, 2009, An optimized wave equation for seismic modeling and reverse time migration: *Geophysics*, 74, no. 6, WCA153–WCA158.

- Liu, Y., D. Jin, X. Chang, and H. Sun, 2009, Multiple subtraction using statistically estimated inverse wavelets: 79th Annual International meeting, SEG, Expanded Abstracts, 3098–3102
- Liu, Y., X. Chang, D. Jin, R. He, and H. Sun, 2011, Reverse time migration of multiples for subsalt imaging: *Geophysics*, 76, no. 5,
- Loncarevic, B.D., 1983, Ocean-bottom Seismometry in *CRC Handbook of Geophysical Exploration at Sea*, R.A. Geyer and J.R. Moore ed., CRC Press, Inc.
- MacLeod, M.K., Hanson, R.A., Bell, C.R., and McHugo, S., 1999, The Alba Field ocean-bottom cable seismic survey: Impact on development, SPE Paper 56977, Offshore Europe Conference, Aberdeen.
- Maxwell, P., Grion, S., Haugland, T., and Ronen, S., 2007, A new ocean-bottom seismic node system: Offshore Technology Conference, OTC 18922.
- Maxwell, P., Grion, S., Ronen, S., Owen, T., and Jakubowicz, H., 2007, The evolution of an OBS node—from North Sea tests to final design: EAGE 69th Conference, Extended Abstract.
- Moldoveanu, and Egan, M., 2006, From narrow-azimuth to wide and rich-azimuth acquisition in the Gulf of Mexico, 24, 69-76, First Break.
- Moldoveanu, B., Kapoor, J., and Egan, M., 2008, Full-azimuth imaging using circular geometry acquisition, *The Leading Edge*, V. 27, No. 7, P. 908-913.
- Morse, P.M. and H. Feshbach, 1953, *Methods in Theoretical Physics*, McGraw Hill, New York, 453-600.
- O’Brien, M. J., and S. H. Gray, 1996, Can we image beneath salt?, *The Leading Edge*, 15, 17–22.
- Orange, D. L., Angell, M. M., Brand, J. R., Thomson, J., Buddin, Tim., Williams, M., Hart, W., Berger W. J., 2003, Geological and shallow salt tectonic setting of the Mad Dog and Atlantis Fields: Relationship between salt, faults, and seafloor geomorphology, Offshore Technology Conference, OTC 15157.
- Osen, A., Amundsen, L., Reitan, A., and Helgesen, H. K., 1996, Removal of water-layer multiples from multicomponent sea-bottom data: 66th Annual Internat. Mtg., Soc. Expl. Geophys., Expanded Abstracts, 1531–1534.

- Ray, A., B. Hornby, and J. Gestel, 2003, Largest 3D VSP in the deep water of the Gulf of Mexico to provide improved imaging in the Thunder Horse South Field: 73rd Annual International Meeting, SEG, Expanded Abstracts, 422–425.
- Ronen, S., L. Comeaux, and X. G. Miao, 2005, Imaging down-going waves from ocean-bottom stations: 73rd Annual International Meeting, SEG, Expanded Abstracts, 963–966.
- Ronholt, G., Aronsen, H. A., Guttormsen, M. S., Johansen, S., and Klefstad, L., 2008, Improved imaging using ocean-bottom seismic in the Snøhvit Field, 70th EAGE Conference & Exhibition, Extended Abstract.
- Rosenberg, M. V., 2000, How much does salt obstruct the subsalt image?, 70th Annual International Meeting, SEG, Expanded Abstracts, 582–585.
- Rosland, B. O., Tree, E.L., Barkved, O.I., Kristiansen, P., 1999, Acquisition of 3D/4C OBS data at Valhall, 61st EAGE Conference & Exhibition, Extended Abstract.
- Schneider, W., 1978, Integral formulation for migration in two and three dimensions, *Geophysics*, 43, 49-76.
- Shoshitaishvili, E., Michell, S., Nolte, B., and Clarke, R., 2006, Imaging subsalt target using OBS data in deepwater Gulf of Mexico: 2D synthetic data example, SEG/New Orleans 2006 Annual Meeting.
- Soubaras, R., 1996, Ocean-bottom hydrophone and geophone processing: 66th Meeting, Society of Exploration Geophysicists, Expanded Abstract, 24-27.
- Stewart, R.R. and Gulati, J.S., 1997, 3-D VSP: Recent history and future promise, CREWES Research Report, Chpt. 9.
- Xia, G., Clarke, R., Etgen, J., Kabir, N., Matson, K., and Michell, S., 2006, OBS multiple attenuation with application to the deepwater GOM Atlantis OBS nodes data: 76th Annual International Meeting, SEG, Expanded Abstracts, 2654–2658.
- White, J. E., 1965, *Seismic waves: Radiation, transmission and attenuation*: McGraw-Hill
- Zachariadis, R.G., Thomason, H.B. and Teague, H.E., 1983, Ocean-bottom seismometers in seismic exploration surveys: Planning and operations: 53rd Annual Meeting SEG Expanded Abstracts, paper S15.6, p.468-470.

Zachariadis, R.G. and Bowden, E.A., 1986, Ocean-bottom cable: a fixed multichannel sea floor reflection system: 56th Annual Meeting SEG Expanded Abstracts, paper S4.4.

Zhang, Q., Stewart, R.R., and Sun, Z., 1995, 3-D VSP: Survey design and processing, CREWES Research Report – Volume 7.

Appendix

Appendix A

Fundamentals of Survey Design

The conventional way for designing 2D and 3D area to cover starts with estimation of the value of subsurface parameters. These parameters are maximum target depth, maximum geological dip, minimum target thickness, and minimum target RMS velocity. Acquisition parameters such as receiver interval, receiver line interval, source and source line interval, and maximum offset can be chosen depend on these values (Cordson, 2000). Survey design decision parameters such as fold, bin size, X_{min} , X_{max} , migration apron can be seen in Table A.1.

A.1. Fold

In 3D surveys, for complex land acquisition and multi-element marine acquisition geometry such as multistreamer and multivessel, reflections at a common-midpoint (CMP) come from different range of azimuths and offsets (Figure A.2). Traces from the different sources and receivers that have the same midpoint reflections are stacked in a bin. Bin is a rectangular horizontal area which is defined during survey planning. The number of the traces that stacked in a bin is called fold. Figure A.2 shows a fold distribution map for a simple 3D survey (Ashton, 1994).

| Parameter | Definitions and Requirements |
|-----------------------------|--|
| Fold | Should be $\frac{1}{2} \times 2\text{-D}$ fold (if the S/N is good) up to 2-D fold (if high frequencies are expected). <i>In-line fold</i> = number of receivers \times RI \div (2 \times SLI). <i>Cross-line fold</i> = NRL \div 2. |
| Bin size | Use 3 to 4 traces across target. Should be $< V_{int} \div (4 \times f_{max} \times \sin \theta)$; for aliasing frequency. Should provide N (= 2 to 4) points per wavelength of dominant frequency. <i>Lateral Resolution available</i> : $\lambda \div N$ or $V_{int} \div (N \times f_{dom})$. |
| X_{min} | Should be less than 1.0 to 1.2 times depth of shallowest horizon to be mapped. |
| X_{max} | Should be approximately the same as target depth. Should not be large enough to cause <i>direct wave interference</i> , refracted wave interference (first breaks), or <i>deep horizon critical reflection offset</i> , particularly in the cross-line direction, or intolerable <i>NMO stretch</i> . Should exceed offset required to see deepest LVL (refractor), offset required to cause NMO $\delta t >$ one wavelength of f_{dom} , offset required to get <i>multiple discrimination</i> > 3 wavelengths, and offset necessary for AVO analysis. Should be large enough to measure X_{max} as a function of dip. |
| Migration apron (full-fold) | Must exceed radius of first Fresnel zone, diffraction width (apex to tail) for an upward scattering angle of 30° , i.e., $Z \tan 30^\circ = 0.58 Z$, and dip lateral movement after migration, which is $Z \tan \theta$. Can overlap with fold taper. |
| Fold taper | Is approximately patch dimension \div 4. |
| Record length | Must be sufficient to capture target horizons, migration apron, and diffraction tails. |

Table A.1 Survey design decision table (after Cordson, 2000)

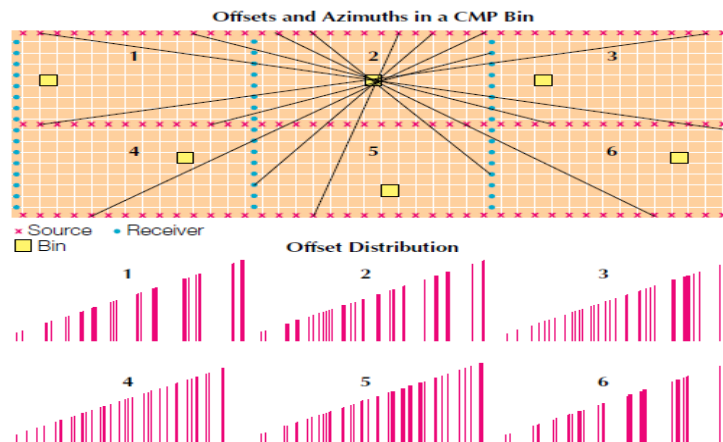


Figure A.1: Offset and azimuth distribution in a CMP bin. Offset distribution is shown at the bottom for 6 specific bin grid. (Ashton, 1994)

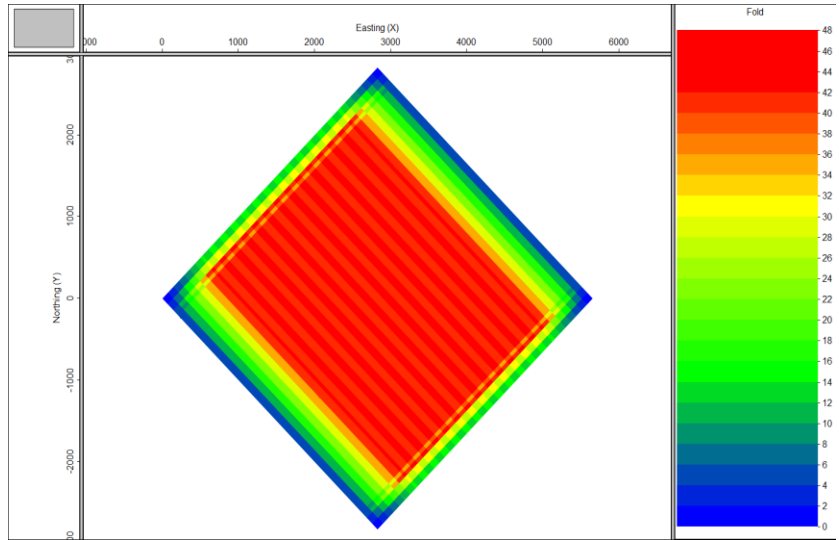


Figure A.2: Fold distribution map for a 3D survey

According to Cordsen (2000), signal-to-noise (S/N) ratio is controlled by fold (Figure A.3). The relation between 3-D and 2-D fold is frequency dependent and varies according to:

$$3D \text{ fold} = 2D \text{ fold} * \text{frequency} * C \quad 1.1$$

where C is an arbitrary constant. For example, if $C = 0.01$ and $2D \text{ fold} = 40$, then $3D \text{ fold}$ is 20 at 50 Hz and 40 at 100 Hz.

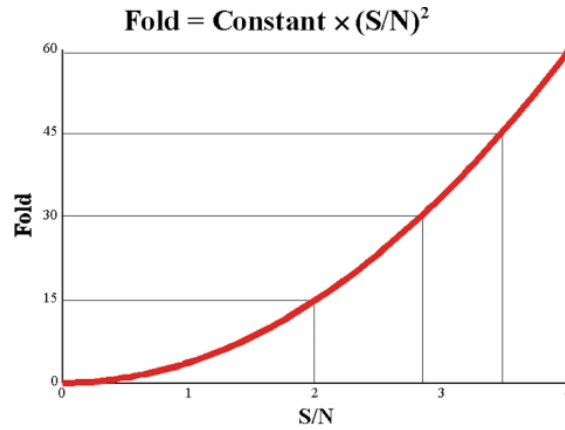


Figure A.3: Fold versus signal-to-noise ratio (S/N), after Cordsen (2000).

Key (1987) showed a calculation of the fold required for a 3D survey based on analysis of 2D data in the same area that has adequate signal-to-random-noise ratio:

$$3D \text{ fold} = 2D \text{ fold} * \frac{3D \text{ Bin spacing}^2 * frequency * \pi * 0.401}{2D \text{ CMP spacing} * velocity} \quad 1.2$$

According to Cordsen (2000), if all offsets are within the acceptable recording range, then the basic fold equation is:

$$fold = SD * NC * B^2 \quad 1.3$$

where SD is the number of source points per unit area, NC is the number of channels, B is the bin dimension (for square bins).

Fold for inline and crossline are given as:

$$Inline \text{ fold} = \frac{\text{number of receiver} \times \text{receiver interval (RI)}}{2 \times \text{source line interval (SLI)}} \quad 1.4$$

$$\text{Crossline fold} = \frac{\text{source line length}}{2 \times \text{receiver line interval (RLI)}} \quad 1.5$$

The total 3-D nominal fold is the product of in-line fold and cross-line fold:

$$\text{total nominal fold} = \text{Inline fold} \times \text{crossline fold} \quad 1.6$$

A.2. Bin Size

According to Cordsen (2000), the S/N is directly proportional to the length of one side of the bin for square bins (Figure A.4). The fold is a quadratic function of the length of one side of the bin (Figure A.5).

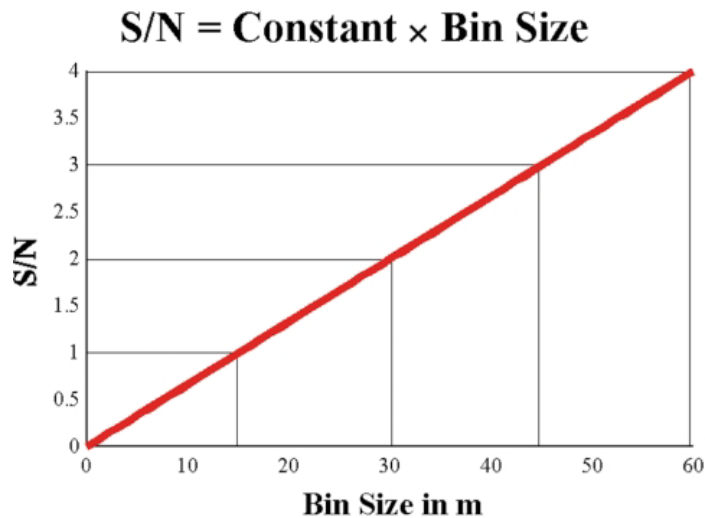


Figure A.4: Signal-to-noise ratio (S/N) versus bin size, after Cordsen (2000).

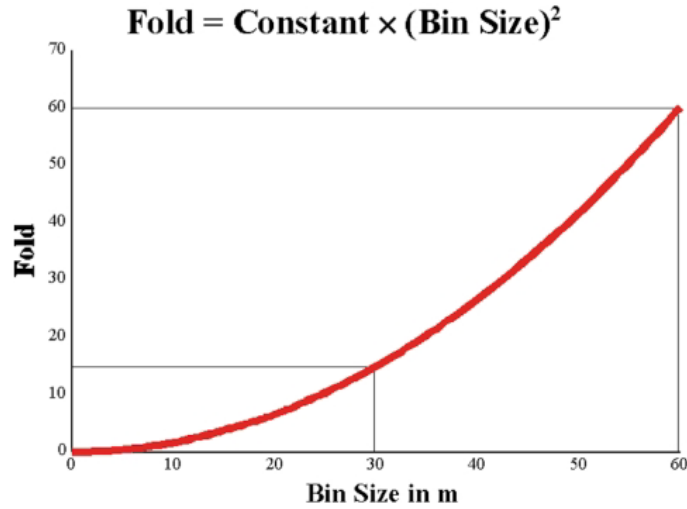


Figure A.5: Fold versus bin size after Cordsen (2000).

Cordsen (2000) mentioned that bin size for target size:

$$Bin\ size = Target\ size \times \frac{1}{3} \quad 1.7$$

For alias frequency:

$$Bin\ size = \frac{V_{int}}{4 \times f_{max} \times \sin\theta} \quad 1.8$$

where V_{int} is interval velocity, f_{max} is maximum frequency and θ is dipping angle.

A.3. Minimum offset (Xmin)

The largest minimum offset is the diagonal of the box of receiver line interval and source (Figure A.6) and it is given by:

$$X_{min} = \sqrt{RLI^2 + SLI^2} \quad 1.9$$

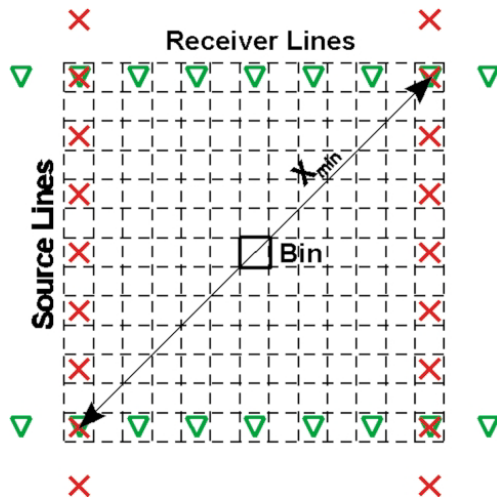


Figure A.6: X_{min} definition with coincident source and receiver stations at corners of box, after Cordsen (2000).

Appendix B

Deghosting and PZ summation

Figure B.1 describes a wavelet travel between ocean-bottom and water's surface. The reflection coefficient is -1 for the reflected pressure wave from the water surface from below, and R for pressure wave from the ocean-bottom from incidence above. The first arrival records on the ocean-bottom with amplitude $+1$, then reflected from ocean-bottom with amplitude R (Hoffe et al., 2000).

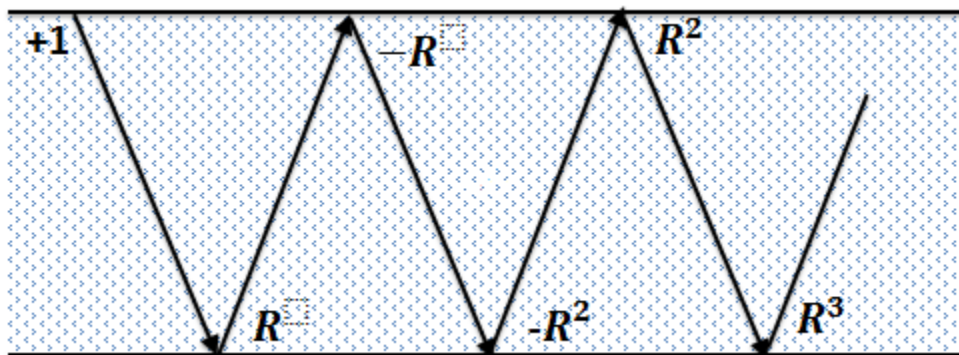


Figure B.1. Reverberations between water surface and ocean-bottom (*Modified from Hoffe et al., 2000*).

According to Hoffe et al. (2000), z transforms for the down-going and up-going waves can be considered at the ocean-bottom. In this case, the down-going wave's z transform at the ocean-bottom can be written as:

$$D(K) = 1 - RK + R^2K^2 + \dots = \frac{1}{(1+RK)} \quad \text{B.1}$$

And z transform of the up-going wave is:

$$U(K) = R - R^2K + R^3K^3 + \dots = \frac{R}{(1+RK)} \quad \text{B.2}$$

Where:

R = reflection coefficient at the ocean-bottom

K = the delay operator for two-way travel through the water layer.

Since the pressure wavefield (P) is the combination of up-going and down-going wavefields, therefore the z transform for the pressure wavefield can be written as:

$$P(K) = U(K) + D(K) \quad \text{or} \quad P(K) = \frac{(1+R)}{(1+RK)} \quad \text{B.3}$$

and the z transform of vertical velocity wavefield (Z), within scalar multiplier ρc (where ρ is density and c is the acoustic velocity), is:

$$Z(K) = U(K) - D(K) \quad \text{or} \quad Z(K) = \frac{(R-1)}{(1+RK)} \quad \text{B.4}$$

From equations B.3 and B.4, it can be seen that summation of the hydrophone (P) component with scaled vertical geophone (Z) component can remove all receiver-side multiples.

$$P(K) + \frac{(1+R)}{(1-R)}Z(K) = 0 \quad \text{B.5}$$

where $\frac{(1+R)}{(1-R)}$ is the ratio of the mean absolute amplitude of hydrophone component to the mean absolute amplitude of vertical geophone component (Barr, 1997).

Figure B.2 represents the up-going wavefield with the reflectivity's z transform δ is:

$$\delta = \sum R_n K^n \quad \text{B.6}$$

It can be considered that the up-going wavefield, δ , is filtered by multiples. In this case, z transform of the up-going wavefield at the ocean-bottom can be written as:

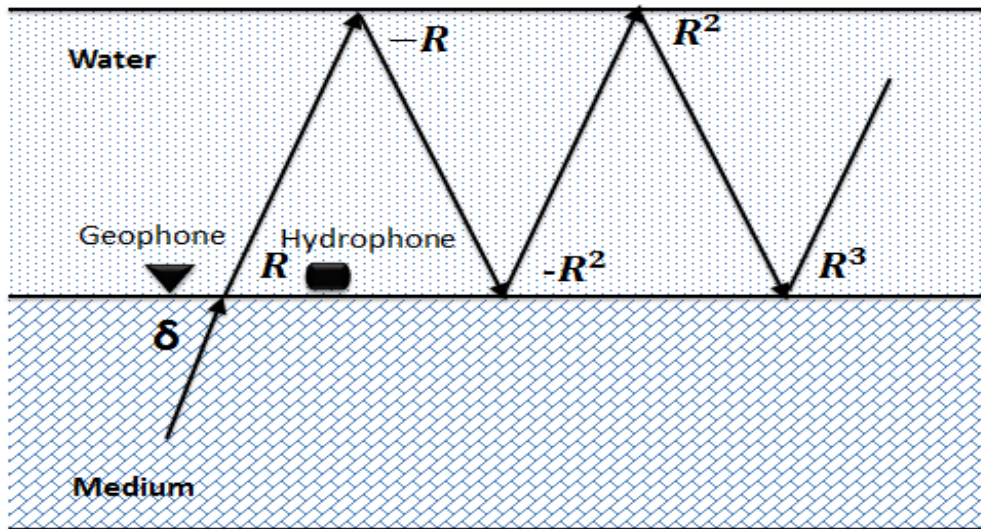


Figure B.2. Up-going wavefield reflectivity, δ , and continuing receiver-side multiples. Modified from Hoffe et al. (2000).

$$U(K) = (1 - RK + R^2K^2 + \dots)\delta = \frac{\delta}{(1+RK)} \quad \text{B.7}$$

and the down-going wavefield at the ocean-bottom is:

$$D(K) = (-K + RK^2 - R^2K + \dots)\delta = \frac{-Z\delta}{(1+RK)} \quad \text{B.8}$$

from equations B.7 and B.8, pressure wavefield (P) and vertical velocity wavefield (Z) can be written as:

$$P(K) = \frac{(1+K)}{(1+RK)}\delta \quad \text{and} \quad Z(K) = \frac{(1-K)}{(1+RK)}\delta \quad \text{B.9}$$

Adding these wavefields in equation B.9 will give us:

$$P(K) + \frac{(1+R)}{(1-R)}Z(K) = \frac{2}{(1-R)}\delta \quad \text{B.10}$$

Appendix C

Imaging condition for RTM of multiples

According to Lui et al. (2011), the imaging condition of RTM consists of crosscorrelating two wavefields. These wavefields are from the source and receivers at each depth level.

Lui (2011) expressed the multiple imaging condition as a zero-lag crosscorrelation between source and receiver wavefields:

$$Image(x, y, z) = \sum_{t=0}^{t_{max}} \{P_f(x, y, z, t) + M_f(x, y, z, t)\} \times M_b(x, y, z, t) \quad C.1$$

where image is the image at location (x, y, z) , and t_{max} is the total recording time. The total data $D(z_0; z_0)$ including primaries $P_f(x, y, z, t)$ and multiples $M_f(x, y, z, t)$ are forward-propagated as the source wavefield, while the receiver multiple wavefield $M_b(x, y, z, t)$ is propagated backward in time.

A surface-related multiple is composed of various of multiples because it is reflected more than once at the water surface:

$$M(x, y, z) = M^1(x, y, z, t) + M^2(x, y, z, t) + M^3(x, y, z, t) + \dots \quad C.2$$

where $M^1(x, y, z, t)$ is the first order multiple, $M^2(x, y, z, t)$ is the second order multiple, and $M^3(x, y, z, t)$ the third order multiple. From here, equation C.1 can be written as:

$$Image(x, y, z) = \sum_{t=0}^{tmax} \begin{bmatrix} P_f(x, y, z, t) + \\ M_f^1(x, y, z, t) + \\ M_f^2(x, y, z, t) + \\ M_f^3(x, y, z, t) + \\ \dots \end{bmatrix} \times \begin{bmatrix} M_b^1(x, y, z, t) \\ M_b^2(x, y, z, t) \\ M_b^3(x, y, z, t) \\ \dots \end{bmatrix} \quad C.3$$

According to Lui (2011), when $P_f(x, y, z, t)$, $M_f^i(x, y, z, t)$ and $M_b^j(x, y, z, t)$ propagate in the medium, they will generate up-going primaries, up-going multiples, down-going primaries, and down-going multiples.

Expanding of equation C.3 can be written as:

$$Image(x, y, z) = \sum_{t=0}^{tmax} \left(P_f(x, y, z, t) \times (M_b^1(x, y, z, t) + M_b^2(x, y, z, t) + M_b^3(x, y, z, t) + \dots) \right) + \left(M_f^1(x, y, z, t) \times (M_b^1(x, y, z, t) + M_b^2(x, y, z, t) + M_b^3(x, y, z, t) + \dots) \right) + \left(M_f^2(x, y, z, t) \times (M_b^1(x, y, z, t) + M_b^2(x, y, z, t) + M_b^3(x, y, z, t) + \dots) \right) + \left(M_f^3(x, y, z, t) \times (M_b^1(x, y, z, t) + M_b^2(x, y, z, t) + M_b^3(x, y, z, t) + \dots) \right) + \dots \quad C.4$$

To express the imaging conditions, equation C.4 can be rewrite as:

$$\begin{aligned}
 & \text{Image}(x, y, z) = \\
 & \sum_{t=0}^{t_{max}} \left[\begin{array}{l} P_f(x, y, z, t) \times M_b^1(x, y, z, t) + \\ M_f^1(x, y, z, t) \times M_b^2(x, y, z, t) + \\ M_f^2(x, y, z, t) \times M_b^3(x, y, z, t) + \\ \dots \end{array} \right] + \sum_{t=0}^{t_{max}} \left[\begin{array}{l} P_f(x, y, z, t) \times M_b^2(x, y, z, t) + \\ M_f^1(x, y, z, t) \times M_b^3(x, y, z, t) + \\ M_f^2(x, y, z, t) \times M_b^4(x, y, z, t) + \\ \dots \end{array} \right] + \\
 & \sum_{t=0}^{t_{max}} \left[\begin{array}{l} M_f^1(x, y, z, t) \times M_b^1(x, y, z, t) + \\ M_f^2(x, y, z, t) \times M_b^1(x, y, z, t) + M_f^2(x, y, z, t) \times M_b^2(x, y, z, t) \\ M_f^3(x, y, z, t) \times M_b^1(x, y, z, t) + M_f^3(x, y, z, t) \times M_b^2(x, y, z, t) \\ + M_f^3(x, y, z, t) \times M_b^3(x, y, z, t) + \dots \end{array} \right] \tag{C.5}
 \end{aligned}$$

According to Lui (2011), the first summation of equation C.5 indicated an image, the second summation generated migration artifacts, and the third summation does not form an image at all and can be ignored.

Appendix D

PHYSICAL MODELING

D.1. Physical modeling in the AGL

Allied Geophysical Laboratories (AGL) has been developing and improving its ultrasonic physical modeling facility for over many years. The purpose of developing this physical modeling system is to carry out the simulated seismic surveys on scaled earth models. These physical earth models are built depending on both the materials used and the complexity of the earth structures to be simulated (Inanli, 2002). Commonly 1:10000 scale factor uses to molded and built the models. These models consist of different materials such as plexiglas, PVC, glass, epoxy resin, rubber, and metals.

Piezoelectric transducers as both sources and receivers are used in the modeling system to acquire the data (Bland, 2006). Transducers locations depend on survey design with variety of source and receiver locations. After placed the transducer in exact locations, ultrasonic signal transmitted into the physical model. Received signal record by a high speed analog-to-digital converter and stored to disk in a format identical to real-world seismic surveys (SEG-Y) (Bland, 2006). In the physical modeling surveys, it is hard to use more than one receiver at the same time like real-world surveys. In this survey, instead of using a spread of multiple receivers, we use a single receiver. Since we

shoot a seismic survey with a single geophone, fold per shot is low and many more shots need to take place to complete the survey than usual (Bland, 2006).

AGL modeling system consists of three systems; marine system, land system and ultrasonic system.

D.2. Model Construction

In this study, which aims to process and image OBN data set from the physical modeling and real ocean-bottom, I used AGL's Vinton Salt Dome model. Vinton dome model is built in the AGL by Dr. Robert Wiley.

The physical model consists of 6 alternate black and blue layers and a salt body. To build the layers, black and blue epoxy resins were used. The physical properties of black and blue resin are given in Table D.1. Figure D.1 shows the stage of model construction.

| | Density (g/cc) | Velocity (m/s) |
|-------------|----------------|----------------|
| Black resin | 1.34 | 2586.9 |
| Blue resin | 2.4 | 3264.3 |
| Salt Body | 2.17 | 4500 |

Table D.1: Physical properties of Black and Blue resin



Figure D.1: Construction stage of Vinton Dome Model. Top left shows bottom layer of model and bottom figure shows finale shape of model (taken by Robert Wiley).

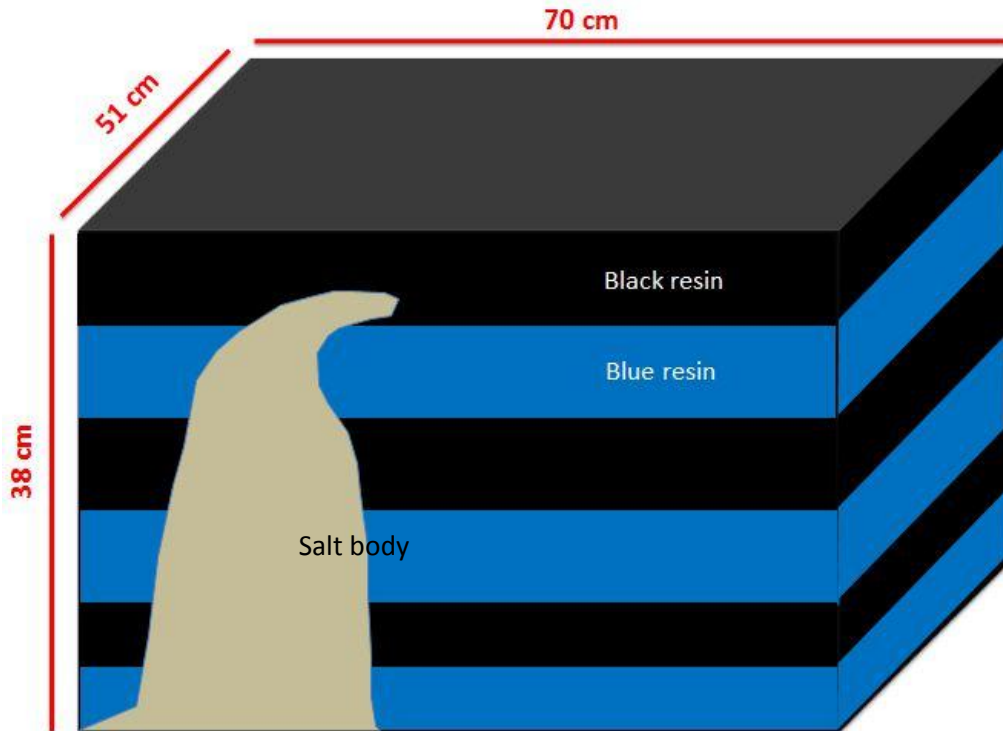


Figure D.2: Dimensions of Vinton Dome model.

Figure D.2 shows the dimensions of the Vinton Dome. Length of the model is 70 cm, height is 38 cm and width is 51 cm.

D.3. Experimental Setup and Recording Instruments

In this survey, I used AGL's existing Vinton salt dome model to acquire ocean-bottom node data in the marine tank. Spherical piezoelectric transducer was used as a source and pin transducer was used as ocean-bottom nodes. The tank filled full of water after model located at the heart of the tank. Pin transducer (receiver) was located on the model surface as nodes are located on the ocean-bottom, and spherical transducer (source) was located 2 cm (200 m in real world) above the model surface (Figure D.3).

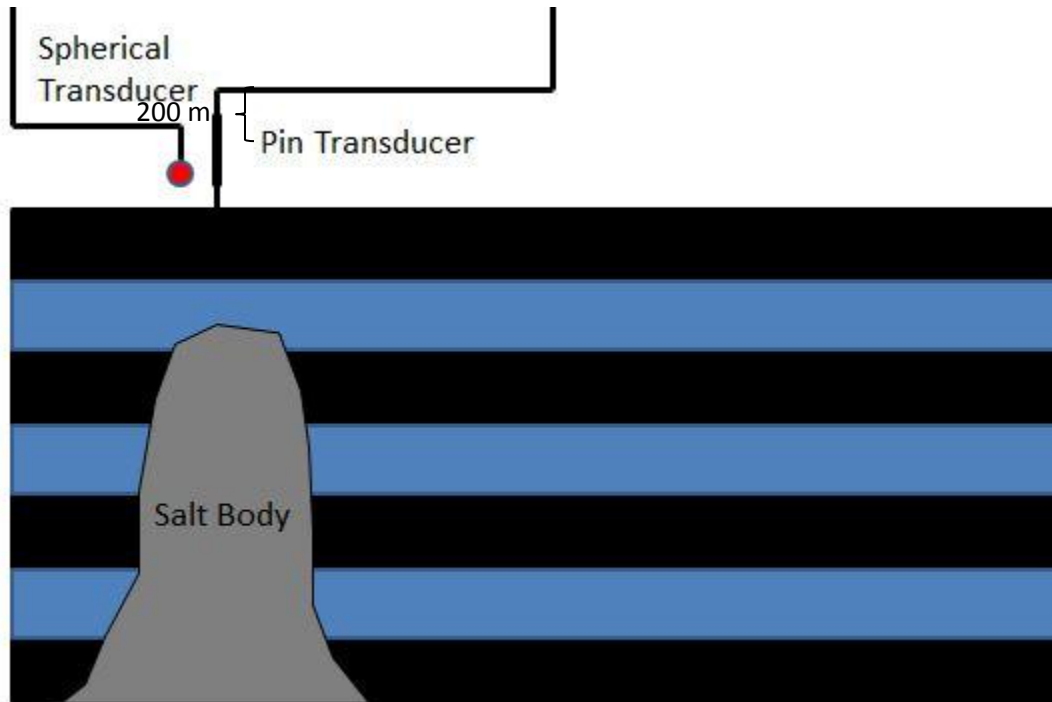


Figure D.3: Schematic illustration of experimental setup on Vinton model. Receiver is located on the surface of the model. Source is located 200 m above the surface.

D.4. Acquisition Geometry

This experiment was 3-D survey which consists of two 2-D lines and one receiver line. The transverse and radial component of the wave train was not recorded. The pin transducer used for both vertical component and pressure component. There were total 6 receiver stations and 224 shot stations (Figure D.4).

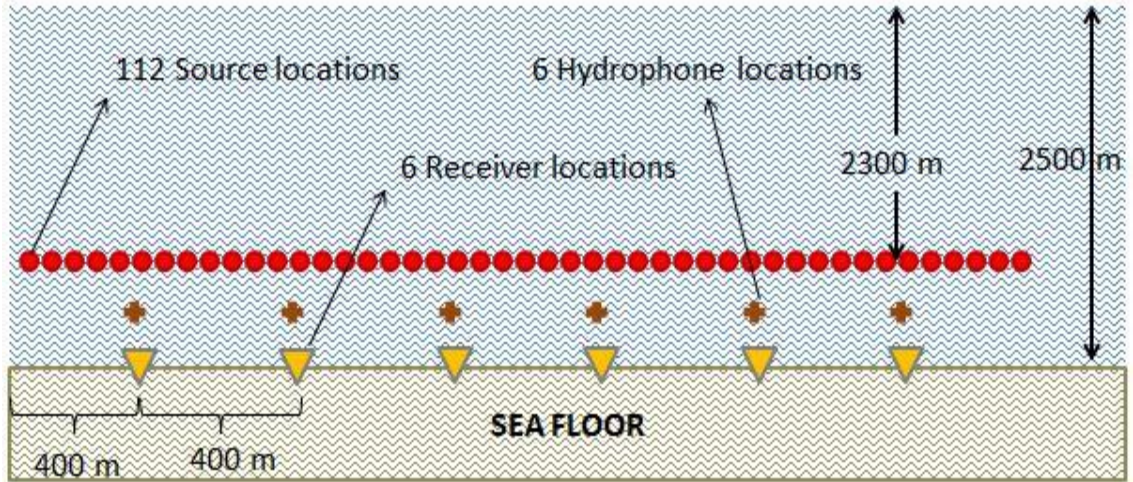


Figure D.4: Schematic diagram of acquisition geometry. Drawing is not to scale. Red circles show shot locations, yellow triangles show receiver locations and brown plus symbols show hydrophone locations.

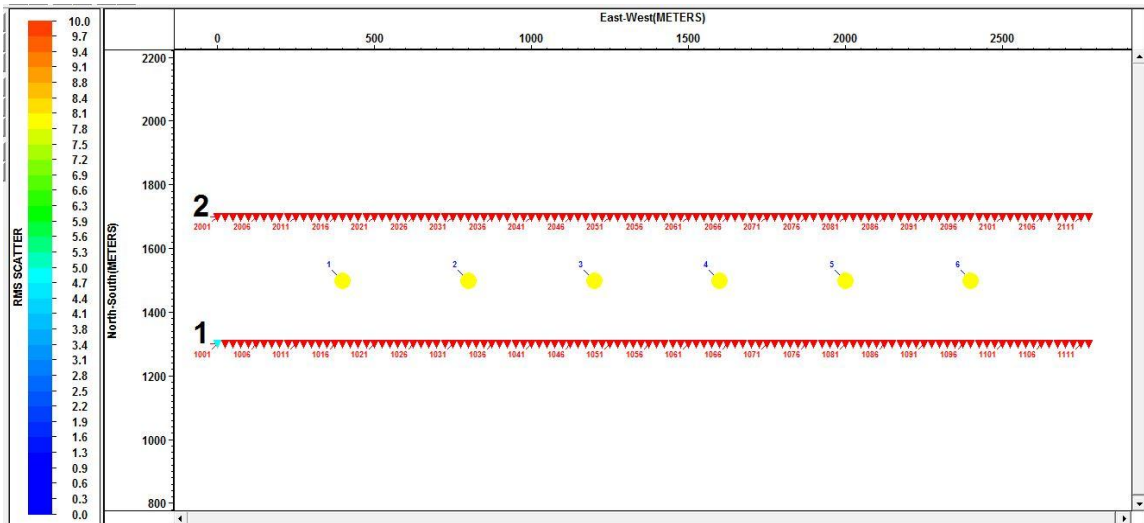


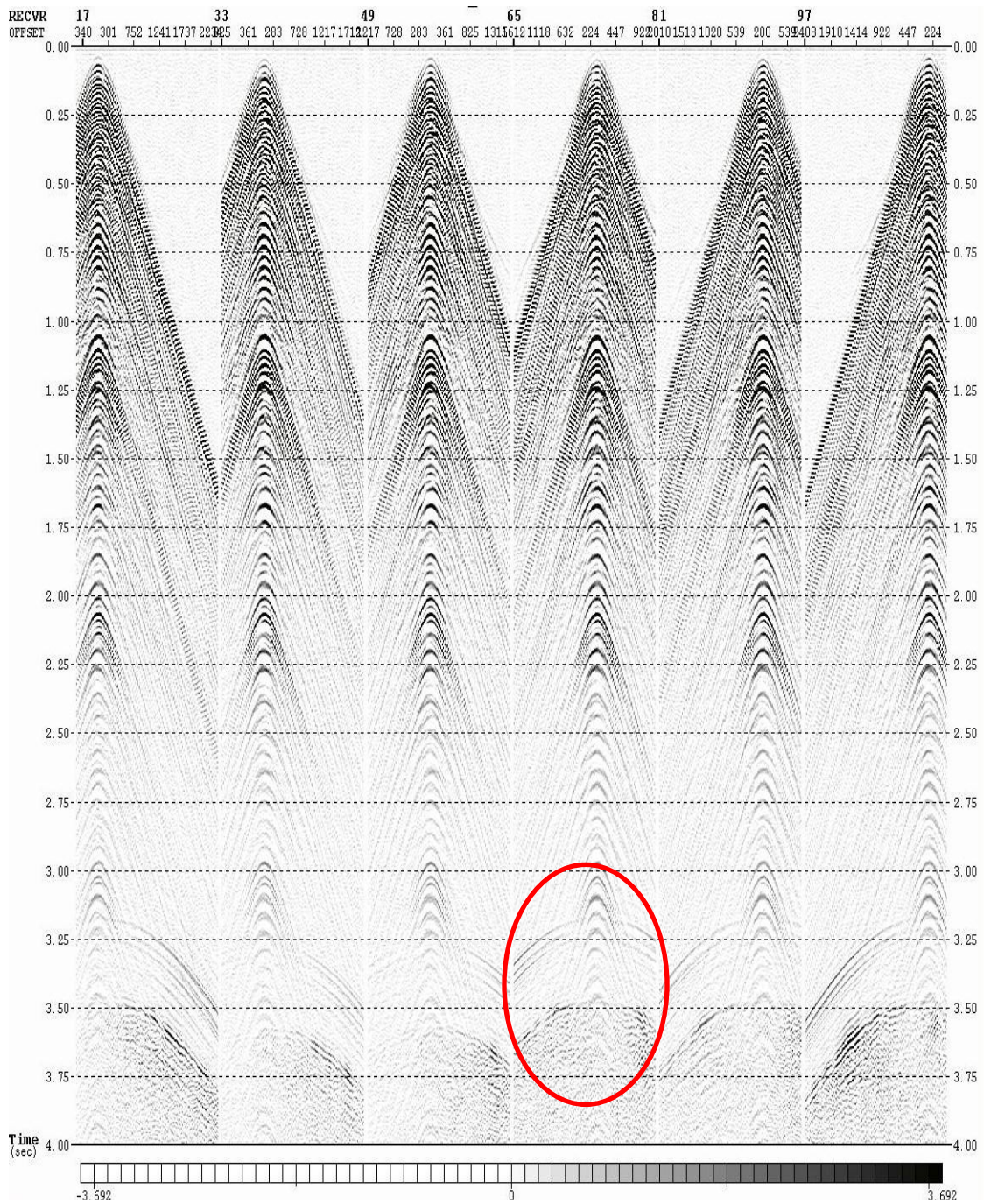
Figure D.5: Location of source lines (red) and position of 6 ocean-bottom nodes in VISTA.

Figure D.5 shows exact receiver and shot location. VISTA processing software was used to display geometry of survey. Red triangles represent shot locations and yellow circles represent receiver locations.

D.5. Data from Physical Modeling

Figure D.5 show common-receiver gathers of subsea physical survey acquired on Vinton model. Pin transducer was located on the surface of the model to record the signal as pressure component. A common-receiver gather from physical modeling data can be seen in Figure D.6.

I then applied Kirchhoff pre-stack time migration method to this physical modeling dataset. The result is shown in Figure D.7.



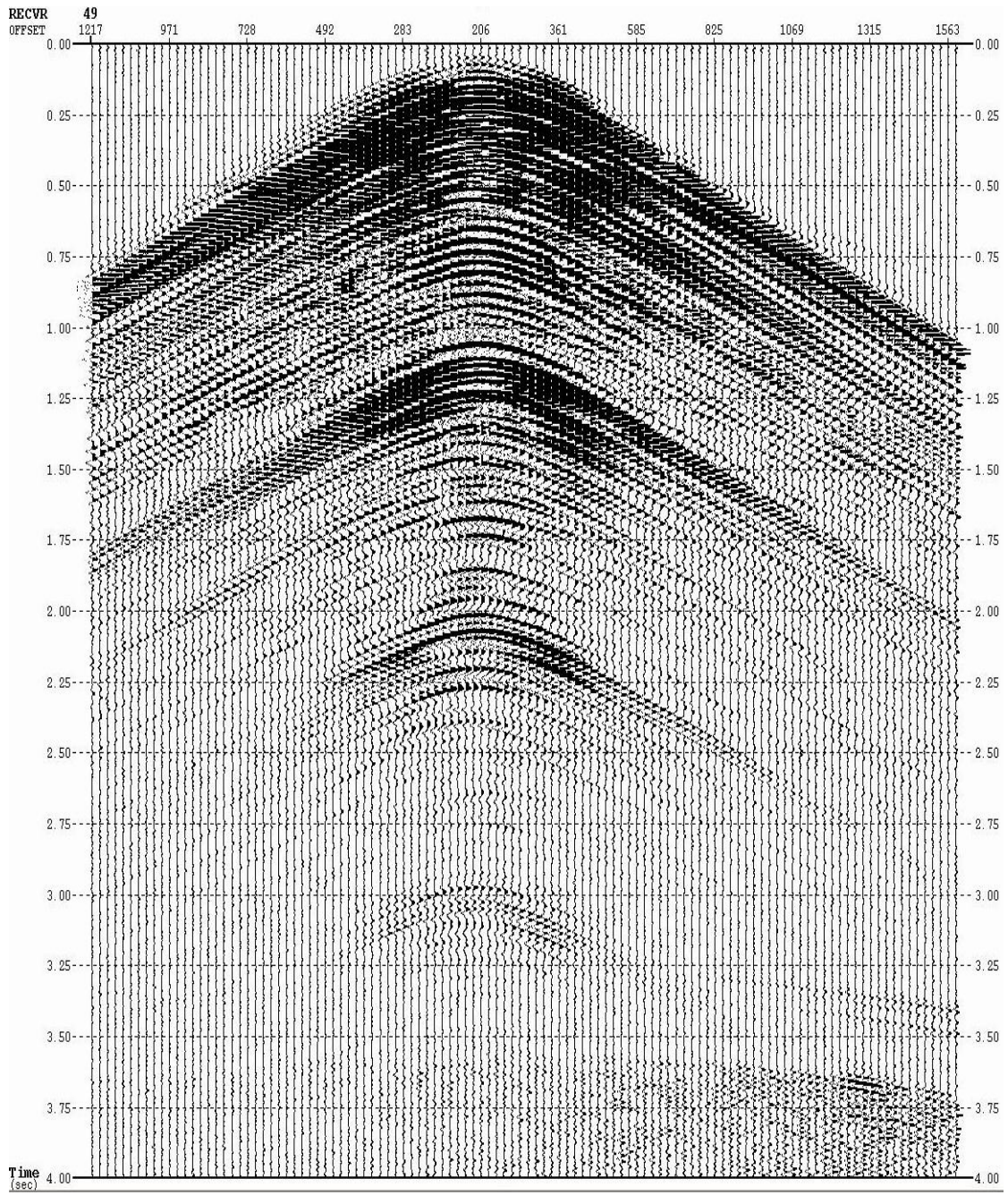


Figure D.7. A common-receiver gather from physical modeling data. The source spacing is 25 m.

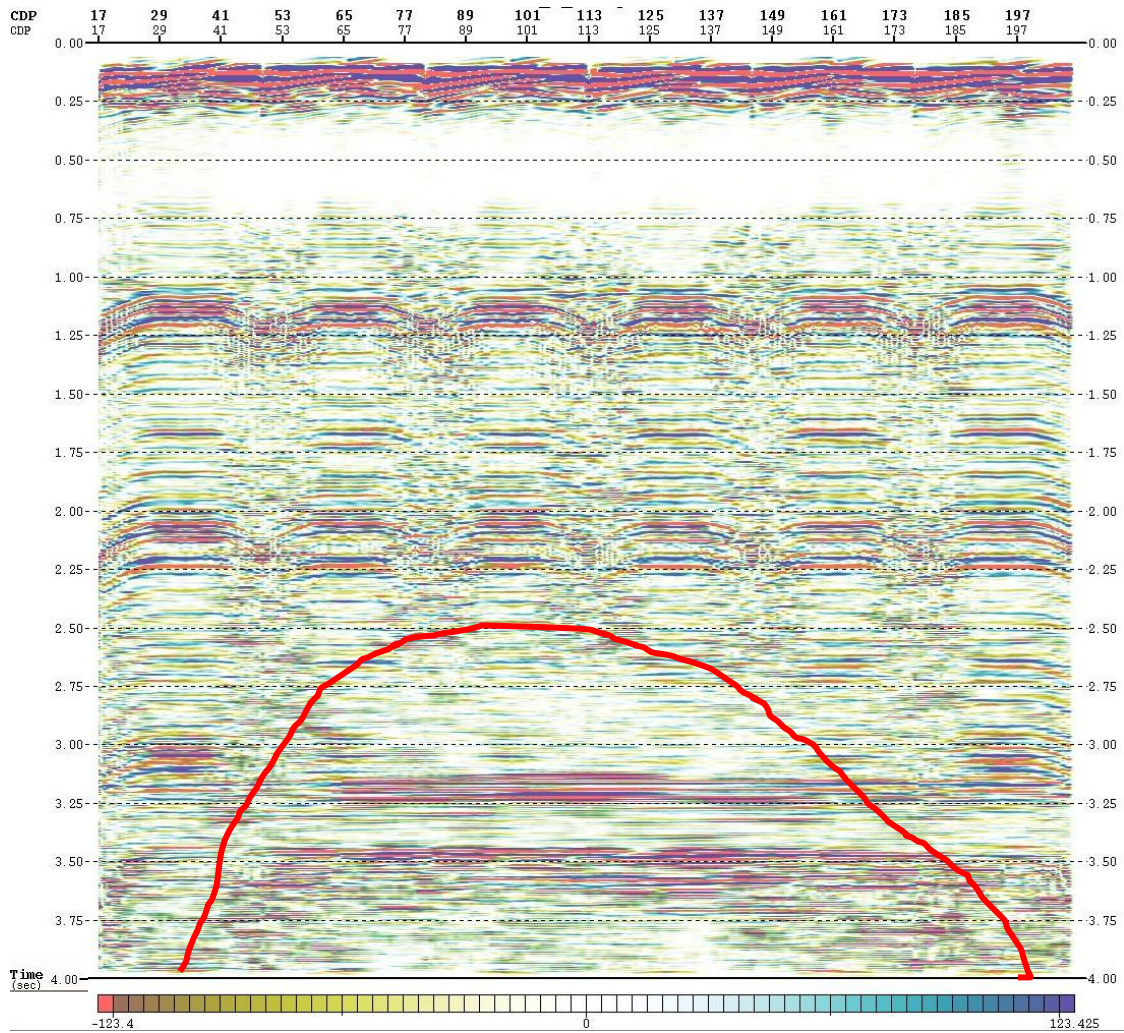


Figure D.7. Kirchhoff pre-stack time migration of physical modeling data.